Soil-Structure Interaction for Deeply Buried Corrugated PVC and Steel Pipes

Chai H. Yoo

Junsuk Kang

Highway Research Center

Auburn University

Auburn University, Alabama

May 2007

IR-07-01

Soil-Structure Interaction for Deeply Buried Corrugated PVC and Steel Pipes

Chai H. Yoo
Junsuk Kang

Highway Research Center
Auburn University
Auburn University, Alabama

May 2007

Acknowledgments

The investigation which led to the results presented herein was supported by Auburn University Highway Research Center and Huff Eminent Scholar Fund. The authors gratefully acknowledge this financial support.

EXECUTIVE SUMMARY

The imperfect trench installation method has been used to reduce earth pressure primarily on buried rigid pipes by inducing reverse soil arching over the pipe. Because corrugated thermoplastic pipes or steel pipes are relatively flexible, their deformation induces a small amount of reverse soil arching. Therefore, there has been limited research regarding the effects of imperfect trench installation on flexible pipes such as those fabricated with corrugated thermoplastic or steel. The objectives of this study were to study the soil-structure interaction for corrugated poly vinyl chloride (PVC) and steel pipes and the efficiency of the imperfect trench method for their installation. The Duncan soil model was used in the development of the soil-structure interaction analysis using finite element methods. The Selig soil parameters were instrumental in the practical implementation of the Duncan soil model. The developed soil-structure interaction model was applied to both embankment and imperfect trench installations. Earth load reductions are quantified by the ratio of the earth pressure for the imperfect trench installation method to earth pressure for the embankment installation method. The geometry of the soft material zone in the imperfect trench installation was optimized to maximize the earth load reduction effects. The optimization process was based on parametric studies with regard to the geometry and location of the soft material zone along with bedding and sidefill treatments. Parametric studies revealed that the optimum geometry of the soft material zone could reduce the maximum wall stress in corrugated PVC and steel pipes by 85%. Predictor equations for earth load, maximum stress, and deflection of corrugated PVC and steel pipes were formulated by

multiple linear regression processes. These equations were developed from a series of finite element analyses of some 600 hypothetical models.

TABLE OF CONTENTS

This page intentionally left blank

LIST OF TABLES

This page intentionally left blank

LIST OF FIGURES

CHAPTER 1

INTRODUCTION

1.1 Statement of the Problem

The use of plastic pipes on federal-aided projects was once prohibited [1]. As of December 15, 2006, the federal highway administration requires "equal consideration" in the project specification of alternate pipe materials including plastic and corrugated aluminum. With this recent development, the use of corrugated PVC pipes in highway drainage structures may dramatically increase.

Theoretical study for designing buried flexible pipe was first performed by Spangler [2]. Watkins [3, 4] reported that the ratio of the vertical soil pressure to the horizontal soil pressure in flexible pipes is only about 2.0 while it can be as high as 3.5 in rigid pipes. This is the major difference between the behaviors of rigid and flexible pipes. The mechanics of induced small positive arching is illustrated in Figure 1.1 where the deformation of the flexible pipe causes a redistribution of the earth load from the crown to the sides of the pipe.

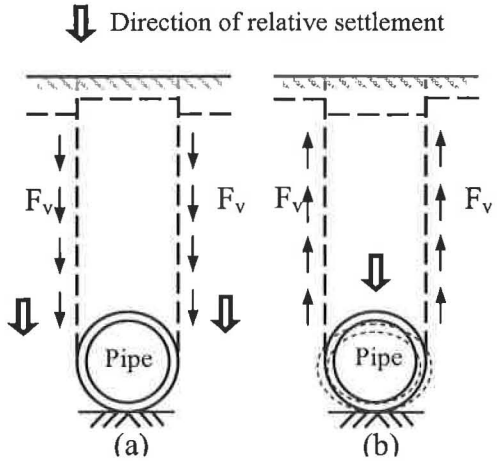

Figure 1.1: Pressure transfer within a soil-pipe system: (a) rigid pipe in embankment installation and (b) flexible pipe in embankment installation (F_v = generated friction forces or shear stresses; interface condition= full-bonded)

The stiffness of a corrugated steel pipe (referred to CSP hereinafter) is somewhere between that of a rigid concrete pipe and a flexible plastic pipe. A CSP may be categorized as semi-flexible [5]. As a consequence, the mechanics of soil arching for CSP are slightly different from that of rigid or flexible pipes. The downward deflection at the top of a CSP, as shown in Figure 1.2(a), is very small and the relative downward deflection of the adjacent backfill soil may be greater than that of the central soil prism above the pipe, thereby inducing a negative arching action. This is similar to the mechanism for a rigid pipe and results in a vertical arching factor substantially greater than one. In the case of truly flexible pipes, the vertical deflection of the central soil prism above the pipe is greater than the deflection of the adjacent backfill soil, as shown in Figure 1.2(b), and induces a positive arching action. This results in a vertical arching factor less than one. The vertical arching factor of CSP's lie between those of rigid and truly flexible pipes.

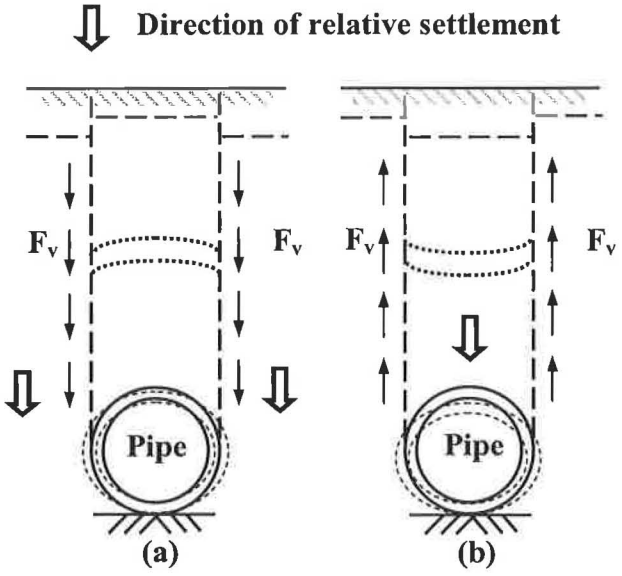

Figure 1.2: Pressure transfer within a soil-pipe system: (a) corrugated steel pipe in embankment installation and (b) corrugated PVC pipe in embankment installation (F_v = generated friction forces or shear stresses; interface condition= full-bonded)

As the CSP is frequently made of very thin gage cold-formed steel sheets, elastic flexural buckling may be an important design parameter. Therefore, it is necessary for designers to be able to assess the buckling strength of CSP. Despite a substantial difference in the buckling strengths of CSP determined by the American Iron and Steel Institute [6] and AASHTO LRFD [7] procedures, there has been little expressed concern [8]. This is perhaps due to the fact that there is another limit imposed by the CSP industry with regard to the maximum slenderness ratio (D/r) permitted. CSP is rarely designed with $D/r > 294$, a threshold value of the slenderness ratio for the yield zone in the AISI formula [6], where D= diameter of pipe and r= radius of gyration per unit length. This study formulated a new equation for the buckling strength of CSP based on the soil-structure interaction using FEA. The buckling strength computed from the new equation is compared with those determined from AISI and AASHTO LRFD procedures. Predictor equations for arching factors, deflections, maximum wall stresses, and buckling strengths are proposed for embankment installations.

Figure 1.3 shows a load transfer within a soil-structure system in imperfect trench installation (referred to ITI hereinafter). McAffee and Valsangkar [9] reported a case study of

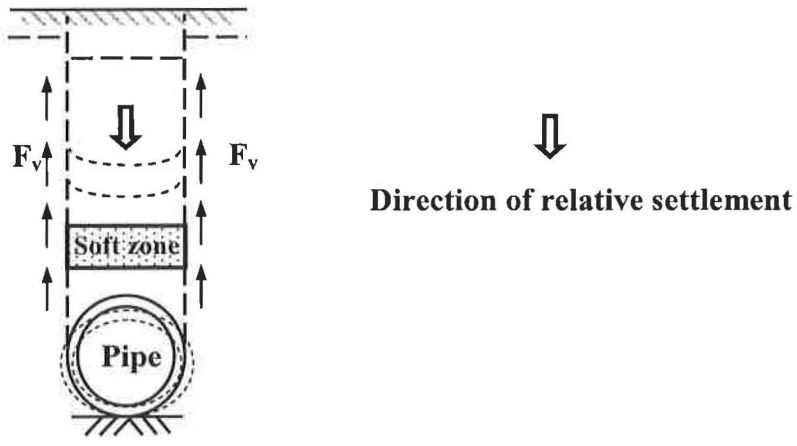

Figure 1.3: Pressure transfer within a soil-pipe system in imperfect trench installation (F_v = generated friction forces or shear stresses)

ITI of rigid pipes in New Brunswick, Canada. They measured earth pressure on a recently constructed concrete pipe and confirmed higher-than-expected lateral earth pressure, almost as high as vertical earth pressure. They concluded that these higher lateral pressures need to be considered in the design of pipes with ITI.

Because corrugated PVC and steel pipes are relatively flexible, a small amount of reverse soil arching is induced. Perhaps partly because of the above reason, there has been limited research regarding the effects of ITI on flexible pipes. As part of this study, an investigation of the efficiency of ITI for corrugated PVC and CSP was conducted. An effective measure is proposed to overcome higher-than-expected lateral earth pressures that developed with ITI. An optimum geometry for the soft zone developed in ALDOT Project No. 930-592 for rigid concrete pipes is re-examined for flexible and semi-flexible pipe. The properties of corrugated PVC and steel pipes were taken from AASHTO LRFD [7]. After synthesizing and quantifying analytical data collected from some 600 hypothetical models, an optimum geometry for the soft zone in ITI is proposed. The proposed optimum geometry of the soft zone reflects the major difference the response of rigid and flexible pipes. Predictor equations for the reduction rates of arching factors, deflections, and maximum wall stresses are proposed as a function of the modulus of elasticity of the lightweight material and the pipe slenderness ratio (ratio of the pipe diameter to thickness). The reduction rate is defined as follows:

$$R(\%) = 100\left(\frac{X - Y}{X}\right) \tag{1.1}$$

where R = reduction rate; X = maximum values (arching factors, deflections, wall stresses) computed for embankment installation; and Y = values expected for ITI.

1.2 Objectives and Scope

The overall objective of this research was to investigate the soil-structure interaction that take place during the construction of deeply buried flexible pipe when placed with embankment installation procedures and the ITI. Major parameters affecting the soil-structure interaction include bedding materials and installation procedures. The bedding materials and installation procedures used significantly affect the conduit performance. The resulting earth pressure on the conduit is greatly affected by the relative settlement of the soil prism directly above the conduit. An improved understanding of these fundamentals is essential to develop technically sound and yet economical design and installation procedures applicable to both designers and contractors.

An objective of this study was to determine an optimum geometry for the soft material zone in ITI by using finite element methods (referred to FEM hereinafter). Finite element analyses (referred to FEA hereinafter), using both ABAQUS [10] and MSC/NASTRAN [11], were carried out to analyze the soil-structure interaction. The most commonly used programs for the analysis of roadway conduits, CANDE-89 [12, 13] and SPIDA (Soil-Pipe Interaction Design and Analysis) [14] were used to assess the validity of the FEA.

Specific objectives of this research are as follows:

1) To conduct a comprehensive literature search pertinent to buried flexible pipes.
2) To advance a comprehensive understanding of soil-structure interaction.
3) To compare the results from this study with those from current design methods.
4) To develop an optimum geometry for the soft zone in ITI for PVC and steel pipes.
5) To develop design guides which include the following items:
    - Predictor equations for the arching factors, deflections, and maximum wall stresses in embankment installation.

- Predictor equations for the reduction rates of the arching factors, deflections, and maximum wall stresses in ITI.

1.3 Summary of Research

Chapter 2 presents current installation practices based on a review of the technical literature and current standard specifications. Chapter 3 describes the finite element modeling procedures. The soil-structure model was described with the Duncan soil model of which implementation is greatly facilitated by Selig soil parameters. Chapter 4 presents methods of accurately determining the soil pressure exerted on corrugated PVC pipes in both embankment installations and ITI. The effect of bedding and sidefill treatment on resulting earth loads on the conduits is also examined. Chapter 5 discusses methods of accurately determining the soil pressure exerted on corrugated steel pipes in both embankment installations and ITI. The effect of bedding and sidefill treatment on earth loads is also examined. Included in this chapter is the determination of the elastic buckling strength of the buried CSP based on an iterative finite element analysis. Finally, Chapter 6 presents a summary, conclusions, and recommendations for future work.

CHAPTER 2

LITERATURE REVIEW

2.1 General

The main role of roadway pipes is to transport water and occasionally used as overhead viaducts. The design and construction of buried structures is one of the most important functions undertaken by public works engineers. The major engineering challenge is understanding how the structure withstands the imposed earth load. The analysis, design, and installation of buried structures thus require an extensive understanding of soil-structure interactions. This chapter presents the current pipe installation practice based on a review of the technical literature and current standard specifications.

It has been traditional practice to define vertical and horizontal earth loads on a pipe in terms of non-dimensional coefficients called the vertical and horizontal arching factors, *VAF* and *HAF*, respectively [15]. Traditionally, *VAF* and *HAF* are calculated using

$$VAF = \frac{W_e}{PL} = \frac{2N_{sp}}{PL} \quad \text{and} \tag{2.1}$$

$$HAF = \frac{W_h}{PL} = \frac{N_c + N_i}{PL} \tag{2.2}$$

where PL = prism load; W_e = total vertical earth load; W_h = total horizontal earth load; N_{sp} = thrust in the pipe wall at the springline; N_c = thrust in the pipe wall at the crown; and N_i = thrust in the pipe wall at the invert.

2.2 Background

2.2.1 Vertical Arching Factors

Burns and Richard [16] first provided theoretical solutions for vertical load on an elastic circular conduit buried in an isotropic, homogeneous infinite elastic medium, with uniformly distributed pressure acting on horizontal planes at an infinite distance. According to Burns and Richard, VAF are as follows:

For full-bond interface

$$VAF = 0.714 - 0.714\left(\frac{S_H - 0.7}{S_H + 1.75}\right) + \left(\frac{1.143 + 0.054 S_B}{2.571 + 0.572 S_H + 0.163 S_B + 0.039 S_B S_H}\right) \tag{2.1}$$

For free-slip interface

$$VAF = 0.81 - 0.714\left(\frac{S_H - 0.7}{S_H + 1.75}\right) + 0.095\left(\frac{27.31 - S_B}{16.81 + S_B}\right) \tag{2.2}$$

where

$$S_H = \frac{M_S R}{E_P A_P} \tag{2.3}$$

$$S_B = \frac{M_S R^3}{E_P I} \tag{2.4}$$

where S_H = hoop stiffness parameter; M_S = one-dimensional constrained soil modulus; R = pipe radius; E_P = modulus of elasticity of pipe material; A_P = area of pipe wall per unit length; S_B = bending stiffness parameter; and I = moment of inertia of cross section of the pipe wall per unit length.

McGrath [17, 18] consolidated Burns and Richard equations eliminating the interface parameter. The McGrath equations adopted by AASHTO LRFD [7] are as follows:

$$VAF = 0.76 - 0.71\left(\frac{S_H - 1.17}{S_H + 2.92}\right) \tag{2.5}$$

$$S_H = \phi_S \frac{M_S R}{E_P A_P} \tag{2.6}$$

where ϕ_S = resistance factor for soil stiffness (= 0.9).

The AASHTO LRFD equations incorporate only the hoop stiffness parameter (S_H) discarding the bending stiffness (S_B) parameters. However, field tests by Sargand and Masada [19] showed that elastic solutions for accurately predicting vertical soil pressure at the crown required both hoop stiffness (S_H) and bending stiffness (S_B) parameters. The constrained soil modulus (M_S) used in the elastic solutions by Burns and Richard and AASHTO LRFD reflects the effect of the change in soil stiffnesses that takes place with increasing depth of fill. A constrained soil modulus (M_S) can be determined by performing one-dimensional tests on representative soil samples at appropriate strain levels. Representative constrained soil moduli (M_S) for this study were adopted from Table 12.12.3.4-1, AASHTO LRFD [7].

2.2.2 Deflections

Deflection and wall stress are primary performance parameters in the design of corrugated PVC pipe. Deflection is quantified with the ratio of the vertical decrease in diameter (Δ_y) to the pipe diameter (D). Spangler [2, 20] developed the following semi-empirical Iowa formula for calculating the deflection of flexible pipes under earth load:

$$\frac{\Delta_y}{D}(\%) = \left(\frac{K_b q D_L}{E_P I_P / R^3 + 0.061 E'}\right) \times 100 \tag{2.7}$$

where Δ_y = vertical decrease in diameter; D = pipe diameter; K_b = bedding factor; q = vertical stress (surface stress) on the pipe; D_L = deflection lag factor (dimensionless); and E' = modulus of soil reaction (passive pressure at haunch area). The Spangler equation needs properties such as the bedding factor (K_b), deflection lag factor (D_L), and modulus of soil reaction (E') which are generally determined by tests and, therefore, is cumbersome to apply.

Burns and Richard [16] provided the following theoretical solutions for deflections in addition to Equations 2.1 through 2.4 for vertical loads:

For full-bond interface

$$\frac{\Delta_y}{D}(\%) = \frac{q}{4M_s}\left[UF\left(1-a_0^*\right)+VF\left(1-a_2^*-2b_2^*\right)\right]\times 100 \tag{2.8a}$$

For free-slip interface

$$\frac{\Delta_y}{D}(\%) = \frac{q}{4M_s}\left[UF\left(1-a_0^*\right)+\frac{2}{3}VF\left(1+a_2^{**}-4b_2^{**}\right)\right]\times 100 \tag{2.8b}$$

where

$$UF = 2B_k M_s R/(E_p A) \tag{2.8c}$$

$$VF = C_k M_s R^3/(3E_p I) \tag{2.8d}$$

$$a_0^* = \frac{UF-1}{UF+(B_k/C_k)} \tag{2.8e}$$

$$a_2^* = \frac{C_k(1-UF)VF - UF(C_k/B_k)+2B_k}{(1+B_k)VF + C_k(VF+1/B_k)+2(1+C_k)} \tag{2.8f}$$

$$a_2^{**} = \frac{2VF-1+(1/B_k)}{2VF-1+(3/B_k)} \tag{2.8g}$$

$$b_2^* = \frac{(B_k + C_k \times UF)VF - 2B_k}{(1+B_k)VF + C_k(VF+1/B_k)UF + 2(1+C_k)} \tag{2.8h}$$

$$b_2^{**} = \frac{2VF - 1}{2VF - 1 + (3/B_k)} \tag{2.8i}$$

where UF = extensional flexibility ratio; VF = bending flexibility ratio; B_k = nondimensional parameter $= (1 + K_s)/2$; C_k = nondimensional parameter $= (1 - K_s)/2$; K_s = lateral stress ratio $= n/(1 - n)$; and ν = Poisson's ratio of soil.

McGrath [17] proposed the following equation to compute deflections of CSP:

$$\frac{\Delta_y}{D}(\%) = \left(\frac{q}{E_p A_p / R + 0.57 M_s} + \frac{K_B q D_L}{E_p I / R^3 + 0.061 M_s} \right) \times 100 \tag{2.9}$$

The first term in Equation 2.9 quantifies the effects of hoop compression while the second is Spangler's Iowa formula quantifying the effects of bending deformation.

2.2.3 Buckling

AISI [6] presents the following series of equations for computing the critical buckling stresses for CSP with backfill compacted to 85% standard AASHTO T-99 density.

$$f_{cr} = f_y = 227{,}370\,\text{kPa}\ (33{,}000\,\text{psi}) \qquad \text{when } \frac{D}{r} < 294 \tag{2.10}$$

$$f_{cr} = 275{,}600 - 0.558\left(\frac{D}{r}\right)^2 \qquad \text{when } 294 < \frac{D}{r} < 500 \tag{2.11}$$

$$f_{cr} = \frac{3.4 \times 10^{10}}{\left(\frac{D}{r}\right)^2} \qquad \text{when } 500 > \frac{D}{r} \tag{2.12}$$

where f_{cr} = critical buckling stress and f_y = minimum yield point of steel.

Details of experiments that are the basis for the above equations are summarized in a paper by Watkins and Moser [21]. AASHTO LRFD [7] stipulates the following critical stress formulas to be applied in association with SW90 backfill compaction requirements:

$$f_{cr} = 6.89\left[f_u - \frac{f_u^2}{48E_p}(kD/r)^2 \right] \qquad \text{if } D < 0.0254\frac{r}{k}\sqrt{\frac{24E_p}{f_u}} \tag{2.13}$$

$$f_{cr} = 6.89\left[\frac{12E_p}{(kD/r)^2} \right] \qquad \text{if } D > 0.0254\frac{r}{k}\sqrt{\frac{24E_p}{f_u}} \tag{2.14}$$

where f_u = specified minimum metal strength, 310 MPa (45,000 psi) and k = soil stiffness factor, 0.22.

2.2.4 Imperfect Trench Installations

The ITI results in earth loads on pipes installed in embankments which are similar to those on pipes installed in a trench. A soft (compressible) layer is placed between the top of the pipe and the natural ground surface as shown in Figure 1.3. In traditional ITI, backfill is placed and thoroughly compacted on both sides and for some distance above a projecting embankment conduit. Then a trench is constructed in this compacted fill by removing a prism of soil having the same width as the conduit and refilling with soft lightweight (compressible) materials as shown in Figure 1.3. The mechanics of ITI are shown in Figure 2.1.

The imperfect trench method of pipe installation was originally developed by Marston [25]. Spangler [23] significantly improved the method. Marston [26] and Spangler [23] quantified the load on conduits installed by imperfect trench conditions by solving differential equations based on the equilibrium conditions of a simplified free body of prisms, and proposed the following equation for predicting loads:

$$W = C_n \gamma B_c^2 \tag{2.15}$$

where C_n = load coefficients and B_c = the out-to-out horizontal span of the conduit.

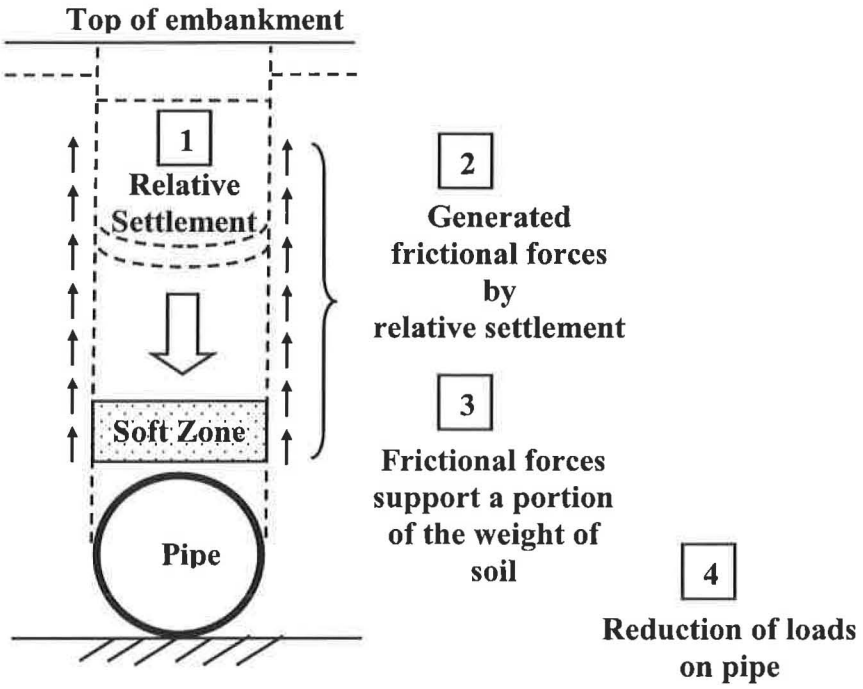

Figure 2.1: Mechanism of imperfect trench installation

Although graphic illustrations are provided for the computation of coefficients, there exist many practical difficulties as the coefficient proposed contains parameters that cannot be determined readily. These parameters include the settlement ratio, computed by Equation 2.16, and the height of the plane of equal settlement, determined by a graphical method as shown in Figures A1.1-6.

$$r_{sd} = \frac{s_g - (s_d + s_f + d_c)}{s_d} \tag{2.16}$$

where r_{sd} = settlement ratio for imperfect trench conduits; s_g = settlement of surface of compacted soil; s_d = compression of fill in ditch within height; s_f = settlement of flow line of

conduit; d_c = deflection of conduit, i.e., shortening of its vertical dimension; and $(s_d + s_f + d_c)$= settlement of critical plane. Although the settlement ratio, r_{sd}, is a rational quantity used in the development of the load formula, it is very difficult to predetermine the actual value that will develop in a specific case. Spangler and Handy [27] recommended values of the settlement ratio based on observations of the performance of actual culverts under embankments, as shown in Table A1.2 of Appendix 1. Imperfect trench designs based on the Marston-Spangler theory have generally been successful. However, experimental studies have shown the predicted earth pressure to be highly conservative [28, 29, 30]. This is perhaps attributable, in part, to the conservative parameters used in the development of the design charts [31].

Vaslestad et al. [30] proposed design equations for determining earth loads exerted on the conduits in induced trench installations. Earth loads on the conduit are determined by applying an arching factor to the overburden pressure. This arching factor is based on the friction number, S_v, used by Janbu to determine friction on piles [32]. Vaslestad's equation for estimating earth pressures on an induced trench culvert is given as follows:

$$\sigma_v = N_A \gamma H \tag{2.17}$$

$$N_A = \frac{1 - e^{-2S_V \frac{H}{B}}}{2S_V \frac{H}{B}} \tag{2.18}$$

$$S_V = |\gamma| \tan \rho K_A \tag{2.19}$$

where N_A = arching factor; S_V = Janbu's friction number; B = width of conduit; r = toughness ratio $\left(=\frac{\tan\delta}{\tan\rho}\le 1\right)$; $\tan\rho$ = mobilized soil friction; f = degree of soil mobilization; $\tan\phi$ = soil friction; and $K_A=\frac{1}{\left[\sqrt{1+\tan^2\rho}+\tan\rho\sqrt{1-\left|1-\left|r\right|\right|}\right]^2}$.

Vaslestad reported that the design method shows good agreement between the earth pressure measured at the top of the buried conduits in a full scale induced trench installation and the results from FEA program CANDE [32]. However, Vaslestad did not include the effect of shear force on the sidefill, foundation characteristics, and sidefill treatment.

ITI procedures have not been improved much since the work of Marston [24, 25] and Spangler [23, 33]. Tyler [31] investigated the effects of a number of variables on earth pressures including the pipe shape, backfill material, as well as the location, width, and stiffness of the soft zone. Tyler [31] indicated that the soft zone need not be highly compressible or thick to generate significant reductions of earth pressure, which turned out to be wrong according to this study. Vaslestad et al. [30] and Tyler [31], however, did not present specific guidelines for optimizing soft zone geometry. Katona [12] mentioned that the backpacking material, such as a low density polystyrene foam, can be used to reduce the earth pressure around the pipe (in a qualitative sense), yet he did not present the specifics such as geometries and properties of backpacking. Recently, Yoo et al. [34] presented guidelines for optimizing the geometry of the soft zone.

This page intentionally left blank

CHAPTER 3

SOIL-STRUCTURE MODELING

3.1 Introduction

A FEA of a soil-structure system is different from a FEA of a simple, linearly elastic, continuum mechanics problem in several ways. The soil has a nonlinear stress-strain relationship. Therefore, a large step of load increments can lead to significant errors in evaluating stress and strain within a soil mass. In the approximate nonlinear incremental analysis procedures adopted in this study, nonlinear soil properties were simulated by way of the hyperbolic stress-strain relationship. It was also necessary to allow movement between the soil and the walls of the pipe, which necessitated an interface element. As shown by Kim and Yoo [35] and McVay [36, 37], the effect of interface behavior was generally insignificant for soil-structure interaction of rigid structures. McVay [36, 37] showed that results were reasonable without numerical modeling of the compaction process.

Four widely used computer programs were run, comparatively. ABAQUS [10] and MSC/NASTRAN [11] are commercially available general purpose finite element programs. SPIDA [14, 38] and CANDE-89 [12] are two commonly used computer programs for soil-structure interaction analysis.

Although **Article 12.10.2.1**, AASHTO LRFD [39] requires that bedding placed under a conduit be compacted to minimize settlement and control the conduit grade, it was found from FEA that both the loads on the pipe and the bending moments at the invert were reduced when uncompacted (loose) middle bedding was placed as described in Figure 3.1. McGrath and Selig

[40] also observed this trend. However, the outer bedding, described in Figure 3.1, should be compacted to provide support to the haunch area and to provide an alternate vertical load path around the bottom of the conduit. It was confirmed in this study that the haunch area shown in Figure 3.1 contributes significantly to the support of the earth load. Similar phenomena have been observed by other researchers [15, 37, 40]. Both field tests and computer models show that the bending moments are greater in the case of an uncompacted (or untreated) haunch. In this study, therefore, the installation features described in Figure 3.1 were included in the numerical modeling. Bedding materials should meet the requirements of Article 27.5.2, AASHTO LRFD [39]. It should be noted, however, that the practice of the mandatory classification of the treated bedding material into three distinct types is problematic. An examination of a series of numerical analysis results [34] reveals that there is practically no significant difference among type 1, 2 and 3 installations as described in AASHTO LRFD [39].

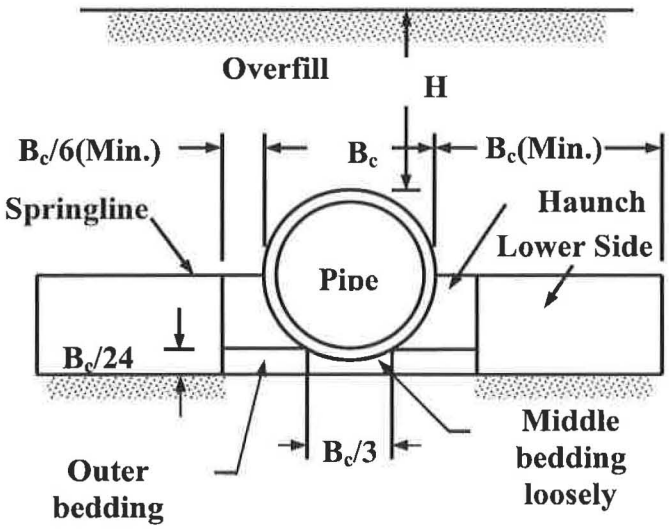

Figure 3.1: AASHTO standard embankment installations [7]

3.2 Soil Models and Parameters

Soil stiffness properties are required to analyze soil-structure interaction. Several soil models were investigated to select the soil stiffness property that best depicted the nonlinear soil characteristics.

3.2.1 Duncan Soil Model and Parameters

Kondner [41] has shown that the nonlinear stress-strain curves for both clay and sand may be approximated by a hyperbola with a high degree of accuracy. This hyperbola can be represented by an equation of the form:

$$(\sigma_1 - \sigma_3) = \frac{\varepsilon}{a + b\varepsilon} \tag{3.1}$$

where σ_1, σ_3 = the maximum and minimum principal stresses, respectively; ε = the axial strain; and a, b = constants whose values may be determined experimentally. Both of these constants a and b have readily discernible physical meanings. As shown in Figures 3.2 and 3.3, a is the reciprocal of the initial tangent modulus, E_i and b is the reciprocal of the asymptotic value of the stress difference which the stress-strain curve approaches at infinite strain $(\sigma_1 - \sigma_3)_{ult}$. The values of the coefficients a and b may be determined readily if the stress-strain data are plotted on transformed axes, as shown in Figure 3.3. When Equation 3.1 is rewritten in the following form:

$$\frac{\varepsilon}{(\sigma_1 - \sigma_3)} = a + b\varepsilon \tag{3.2}$$

Here, a and b are the intercept and the slope of the resulting straight line, respectively. By plotting stress-strain data in the form shown in Figure 3.3, it is straightforward to determine the values of the parameters a and b corresponding to the best fit between a hyperbola and the test

data. It is commonly found that the asymptotic value of $(\sigma_1 - \sigma_3)$ is larger than the compressive strength of the soil by a small amount, because the hyperbola remains below the asymptotic at all finite values of strain. The asymptotic value may be related to the compressive strength a factor, R_f:

$$(\sigma_1 - \sigma_3)_f = R_f(\sigma_1 - \sigma_3)_{ult} \tag{3.3}$$

where $(\sigma_1 - \sigma_3)_f$ = the compressive strength, or stress difference at failure; $(\sigma_1 - \sigma_3)_{ult}$ = the asymptotic value of stress difference; and R_f = the failure ratio, which always has a value less than unity. For a number of different soils, the value of R_f has been found to be between 0.75 and 1.00, and is essentially independent of confining pressure. By expressing the parameters a and b in terms of the initial tangent modulus value and the compressive strength, Equation 3.1 may be rewritten as

$$(\sigma_1 - \sigma_3) = \frac{\varepsilon}{\left[\frac{1}{E_i} + \frac{\varepsilon R_f}{(\sigma_1 - \sigma_3)_f}\right]} \tag{3.4}$$

This hyperbolic representation of stress-strain curves has been found to be fairly useful in representing the nonlinearity of soil stress-strain behavior [42]. Except for the case of unconsolidated-undrained tests on saturated soils, both the tangent modulus value and the compressive strength of soils have been found to vary with the confining pressure employed in the tests. Experimental studies by Janbu [43] have shown that the relationship between tangent modulus and confining pressure may be expressed as

$$E_i = K \cdot P_a \left(\frac{\sigma_3}{P_a}\right)^n \tag{3.5}$$

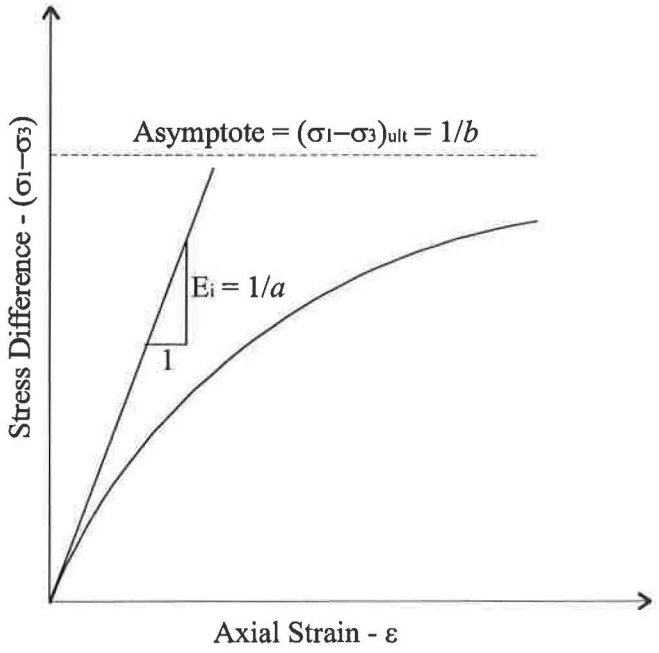

Figure 3.2: Hyperbolic stress-strain curve

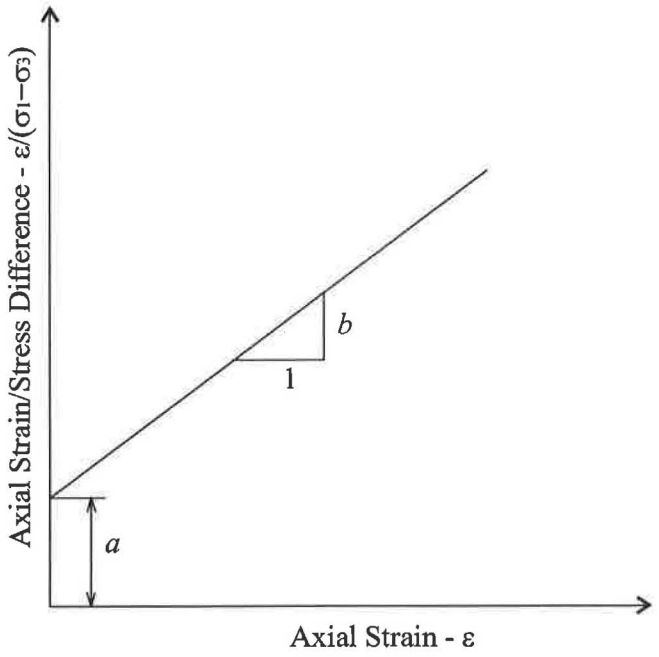

Figure 3.3: Transformed hyperbolic stress-strain curve

where E_i = the initial tangent modulus; σ_3 = the minimum principal stress; P_a = atmospheric pressure expressed in the same pressure units as E_i and σ_3; K = a modulus number; and n = the exponent determining the rate of variation of E_i with σ_3.

If it is assumed that failure will occur with no change in the value of σ_3, the relationship between compressive strength and confining pressure may be expressed conveniently in terms of the Mohr-Coulomb failure criterion as

$$(\sigma_1 - \sigma_3)_f = \frac{2c\cos\phi + 2\sigma_3 \sin\phi}{1 - \sin\phi} \tag{3.6}$$

where c, ϕ = the Mohr-Coulomb strength parameters. Equations 3.5 and 3.6 provide a means of relating stress to strain and confining pressure using the five parameters K, n, c, ϕ, and R_f. Nonlinear, stress-dependent stress-strain behavior may be approximated in FEA by assigning different modulus values to each of the soil elements. The modulus value assigned to each element is selected on the basis of the stresses or strains in each element. Because the modulus values depend on the stresses, and the stresses in turn depend on the modulus values, it is necessary to make repeated analyses to ensure that the modulus values and stress conditions correspond for each element in the system.

The stress-strain relationship expressed by Equation 3.4 may be employed in incremental stress analyses because it is possible to determine the value of the tangent modulus corresponding to any point on the stress-strain curve. If the value of the minimum principal stress is constant, the tangent modulus, E_t, may be expressed as

$$E_t = \frac{\partial(\sigma_1 - \sigma_3)}{\partial\varepsilon} \tag{3.7}$$

Substituting the strain, ε, derived from Equation 3.4, the initial tangent modulus, E_i, in Equation 3.4, and the compressive strength, $(\sigma_1 - \sigma_3)_f$, in Equation 3.6 into the result of the differentiation of Equation 3.7, the following expression is obtained for the tangent modulus [44, 45]:

$$E_t = \left[1 - \frac{R_f(1-\sin\phi)(\sigma_1 - \sigma_3)}{2c\cos\phi + 2\sigma_3 \sin\phi}\right]^2 KP_a\left(\frac{\sigma_3}{P_a}\right)^n \tag{3.8}$$

For the hyperbolic stress-strain relationships, the same value for the unloading-reloading modulus, E_{ur}, is used for both unloading and reloading. The value of E_{ur} is related to the confining pressure by an equation of the same form as Equation 3.5

$$E_{ur} = K_{ur}P_a\left(\frac{\sigma_3}{P_a}\right)^n \tag{3.9}$$

where K_{ur} is the unloading-reloading modulus number. The value of K_{ur} is always larger than the value of K (for primary loading). K_{ur} may be 20% greater than K for stiff soils such as dense sands. For soft soils such as loose sands, K_{ur} may be three times as large as K. The value of the exponent n is nearly unchanged for primary loading and unloading, and in the hyperbolic relationships it is assumed to be the same.

The value of the Poisson's ratio may be determined by analyzing the volume changes that occur during a triaxial test. For this purpose, it is convenient to calculate the radial strains during the test using the equation.

$$\varepsilon_r = \frac{1}{2}(\varepsilon_v - \varepsilon_a) \tag{3.10}$$

where ε_v and ε_a are the volumetric and axial strains. Taking compressive strains as positive, the value of ε_a is positive and the value of ε_r is negative. The value of ε_v may be either positive or negative. If the variation of ε_a versus ε_r is plotted, as shown in Figure 3.4, the resulting curve can be represented with reasonable accuracy by a hyperbolic equation of the form:

$$\varepsilon_a = \frac{-\varepsilon_r}{\nu_i - d\varepsilon_r} \tag{3.11}$$

Equation 3.11 may be transformed into Equation 3.12.

$$-\frac{\varepsilon_r}{\varepsilon_a} = \nu_i - d\varepsilon_r \tag{3.12}$$

As can be seen from Figures 3.4 and 3.5, the relationship of these parameters can be linearized. In Equation 3.12, ν_i is the initial Poisson's ratio at zero strain and d is a parameter representing the change in the value of Poisson's ratio with radial strain. For saturated soils under undrained conditions, there is no volume change and ν_i is equal to one half for any value of confining pressure. This variation of ν_i with respect to σ_3 may be expressed by the equation:

$$\nu_i = G - F\log_{10}\left(\frac{\sigma_3}{P_a}\right) \tag{3.13}$$

where G is the value of ν_i at a confining pressure of one atmosphere, and F is the reduction in ν_i for a ten-fold increase in σ_3. After differentiating Equation 3.11 with respect to ε_r, substituting Equation 3.13, and eliminating the strain using Equations 3.2 to 3.5, the value of Poisson's ratio may be expressed in terms of the stresses as follows:

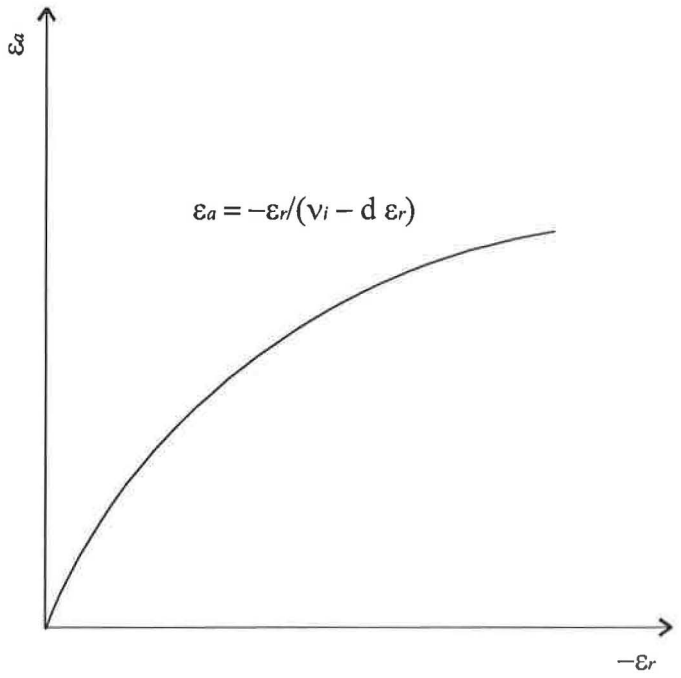

Figure 3.4: Hyperbolic axial strain-radial strain curve

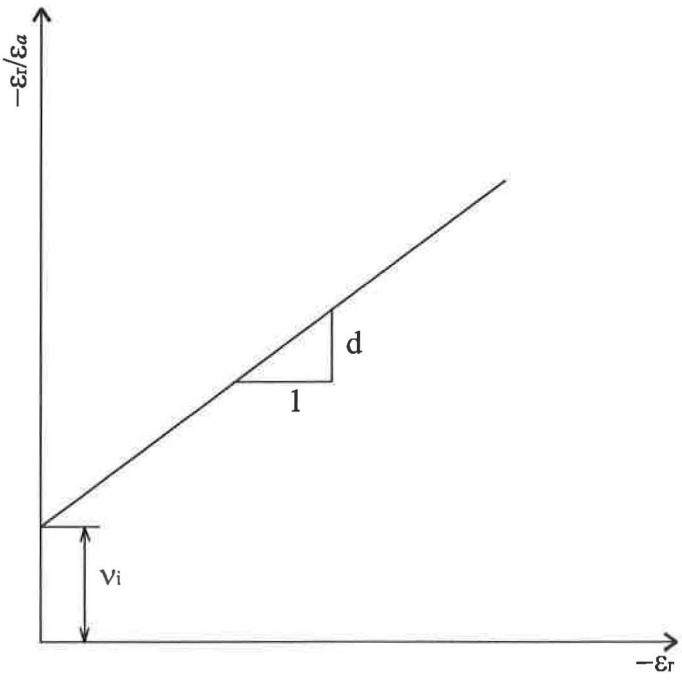

Figure 3.5: Transformed hyperbolic axial strain-radial strain curve

$$\nu_t = \frac{G - F\log\left(\frac{\sigma_3}{P_a}\right)}{\left\{1 - KP_a\left(\frac{\sigma_3}{P_a}\right)^n\left[\frac{d(\sigma_1-\sigma_3)(1-\sin\phi)}{2c\cos\phi + 2\sigma_3\sin\phi}\right]\right\}^2} \tag{3.14}$$

where σ_1, σ_3 = maximum and minimum principal stresses, respectively; K = modulus number; n = modulus exponent; c = cohesion intercept; ϕ = friction angle; G, F, d = Poisson's ratio parameters; and P_a = atmospheric pressure. There are nine parameters involved in the hyperbolic stress-strain and volume change relationships, and the roles of these parameters are summarized in Table 3.1.

The nonlinear volume change can also be accounted for by employing the constant bulk modulus instead of Poisson's ratio parameters. The assumption that the bulk modulus of the soil is independent of stress level $(\sigma_1 - \sigma_3)$ and that it varies with confining pressure provides a reasonable approximation to the shape of the volume change curves. According to the theory of elasticity, the value of the bulk modulus is defined by

$$B = \frac{\Delta\sigma_1 + \Delta\sigma_2 + \Delta\sigma_3}{3\Delta\varepsilon_v} \tag{3.15}$$

where B is the bulk modulus, $\Delta\sigma_1, \Delta\sigma_2$, and $\Delta\sigma_3$ are the changes in the values of the principal stress, and $\Delta\varepsilon_v$ is the corresponding change in volumetric strain. For a conventional triaxial test, in which the deviator stress $(\sigma_1 - \sigma_3)$ increases while the confining pressure is held constant; hence, Equation 3.15 may be expressed as:

$$B = \frac{(\sigma_1 - \sigma_3)}{3\varepsilon_v} \tag{3.16}$$

Table 3.1: Summary of the hyperbolic parameters

Parameter	Name	Function
K, K_{ur}	Modulus number	Relate E_i and E_{ur} to σ_3
N	Modulus exponent	
C	Cohesion intercept	Relate $(\sigma_1-\sigma_3)$ to σ_3
ϕ	Friction angle	
R_f	Failure ratio	Relates $(\sigma_1-\sigma_3)_{ult}$ to $(\sigma_1-\sigma_3)_f$
G	Poisson's ratio parameter	Value of ν_i at $\sigma_3=p_a$
F	Poisson's ratio parameter	Decrease in ν_i for ten-fold increase in σ_3
D	Poisson's ratio parameter	Rate of increase of ν_t with strain

The value of the bulk modulus for a conventional triaxial compression test may be calculated using the value of $(\sigma_1 - \sigma_3)$ corresponding to any point on the stress-strain curve. When values of B are calculated from tests on the same soil specimen at various confining pressures, the bulk modulus will usually be found to increase with increasing confining pressure. The variation of B with confining pressure can be approximated by an equation of the form [46]:

$$B = K_b P_a \left(\frac{\sigma_3}{P_a} \right)^m \tag{3.17}$$

where K_b is the bulk modulus number and m is the bulk modulus exponent, both of which are dimensionless, and P_a is atmospheric pressure. Experimental studies of this soil model, sometimes called the modified Duncan model, for most soils, has resulted in values of m varying between 0.0 and 1.0. If a bulk modulus is known, the tangent Poisson's ratio can be determined from the basic theory of elasticity by the following equation:

$$\nu_t = \frac{1}{2} - \frac{E_t}{6B} \tag{3.18}$$

Although the hyperbolic relationship outlined previously has proven to be quite useful for a wide variety of practical problems, it has some significant limitations. Duncan et al. [46] outlined the following limitations: 1) Being based on the generalized Hooke's law, the relationships are most suitable for analysis of stresses and movements prior to failure. The relationships are capable of accurately predicting nonlinear relationships between loads and movements, and it is possible to continue the analyses up to the stage where there is local failure in some elements. However, once a stage is reached where the behavior of the soil mass is controlled to a large extent by properties assigned to elements which have already failed, the results will no longer be reliable, and they may be unrealistic in terms of the behavior of real soils at and after failure. 2) The

hyperbolic relationships do not include volume changes due to changes in shear stress, or shear dilatancy. They may, therefore, be limited with regard to accuracy with which they can be used to predict deformations in dilatant soils, such as dense sands under low confining pressures. The values of the tangent Poisson's ratio calculated using Equation 3.7 may result in a value exceeding 0.5 for some combinations of parameter values and stress values, so it needs to be specified to be less than 0.5 in the computer program. 3) The parameters are not fundamental soil properties, but only values of empirical coefficients that represent the behavior of the soil under a limited range of conditions. The values of the parameters depend on the density of the soil, its water content, the range of pressures used in testing, and the drain conditions. In order that the parameters will be representative of the real behavior of the soil under field conditions, the laboratory test conditions must correspond to the field conditions with regard to these factors.

3.2.2 Selig Bulk Modulus and Parameters

Both the Duncan et al. [46] and Selig [47] parameters were derived using the same Young's modulus obtained from constant confining pressure triaxial tests. Musser [12], however, recognized that Selig's model incorporated an alternative method for obtaining bulk modulus based on a hydrostatic compression test. In this test, the soil specimen is compressed under an increasing confining pressure applied equally in all directions. According to Equation 3.15, tangent bulk modulus B is the slope of the hydrostatic stress-strain curve. Selig observed that the curve relating σ_m and ε_{vol} was found to be reasonably represented by the hyperbolic equation

$$\sigma_m = \frac{B_i \varepsilon_{vol}}{1-(\varepsilon_{vol}/\varepsilon_u)} \tag{3.19}$$

where B_i = initial tangent bulk modulus, and ε_u =ultimate volumetric strain at large stress. As the tangent bulk modulus B is the slope of the hydrostatic stress-strain curve, σ'_m, it can be determined by differentiating Equation 3.19 with respect to ε_{vol} and substituting the expression for ε_{vol} obtained by rearranging Equation 3.19. The result is Selig's bulk modulus given by Equation 3.20.

$$B = B_i(1 + \sigma_m / (B_i \varepsilon_u))^2 \tag{3.20}$$

To determine the parameters B_i and ε_u, the test results from Figure 3.6 are plotted in the linearized hyperbolic form as shown in Figure 3.7. Once B_i and ε_u are known, the test results can then be represented by Equation 3.20.

Lin [48] showed that the hyperbolic formulation for bulk modulus given by Equation 3.20 better represents soil behavior in a hydrostatic compression test than Duncan's power formulation represented by Equation 3.17, thus favoring the use of Selig's model.

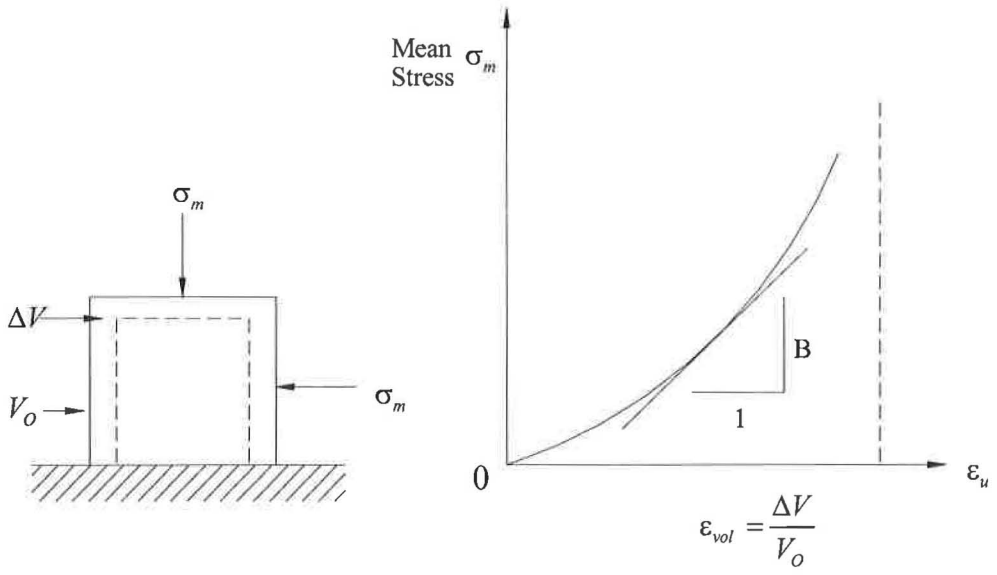

Figure 3.6: Hydrostatic compression test

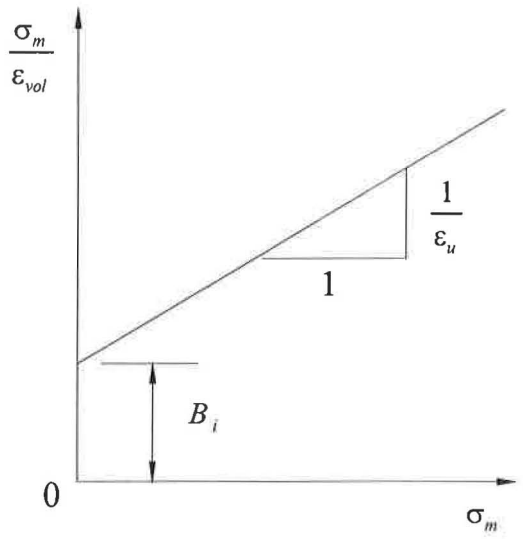

Figure 3.7: Linear transformation of hyperbola for bulk modulus

3.3 Finite Element Modeling

3.3.1 Modeling Techniques

The schematic finite element models for embankment installations and ITI are shown in Figure 3.8. Taking advantage of symmetry, only one-half of the system is included in the model. Experience has shown that lateral boundaries of the model need not be extended further than 3 times the pipe width from the center of the pipe. For deep fill, the current version of SPIDA and CANDE-89 (Level 2 option) has upper boundaries 3 times and 1.5 times, respectively, the pipe width above the crown of the pipe. An equivalent overburden pressure is used to represent the remaining soil weight. It is further noted that CANDE-89 (Level 2 option) limits the number of beam elements for modeling the pipe to ten while SPIDA allows it to be nineteen. CANDE-89 (Level 3 option) eliminates the mesh limitations imposed in Level 2 analysis. However, the lack of an automatic mesh generation scheme that is available in the lower level options in CANDE-89 makes the input data generation a fairly cumbersome task.

The FEA results in this study also showed that lateral and top boundaries need not be extended beyond 3 times the width of the pipe from the center of the pipe and 3 times the width of the pipe from the crown of the pipe, respectively. A rigid layer was located 1.5 times the width of the pipe below the invert (or bottom) of the conduit since soil beyond this depth did not affect the results. Curved beam elements and straight beam elements are used to model the circular pipes. A plane strain linear elastic element was used for soil. The elastic properties of the soil were described by two stiffness parameters, tangent modulus (E_t) and bulk modulus (B) as defined by Equations 3.8 and 3.20, respectively.

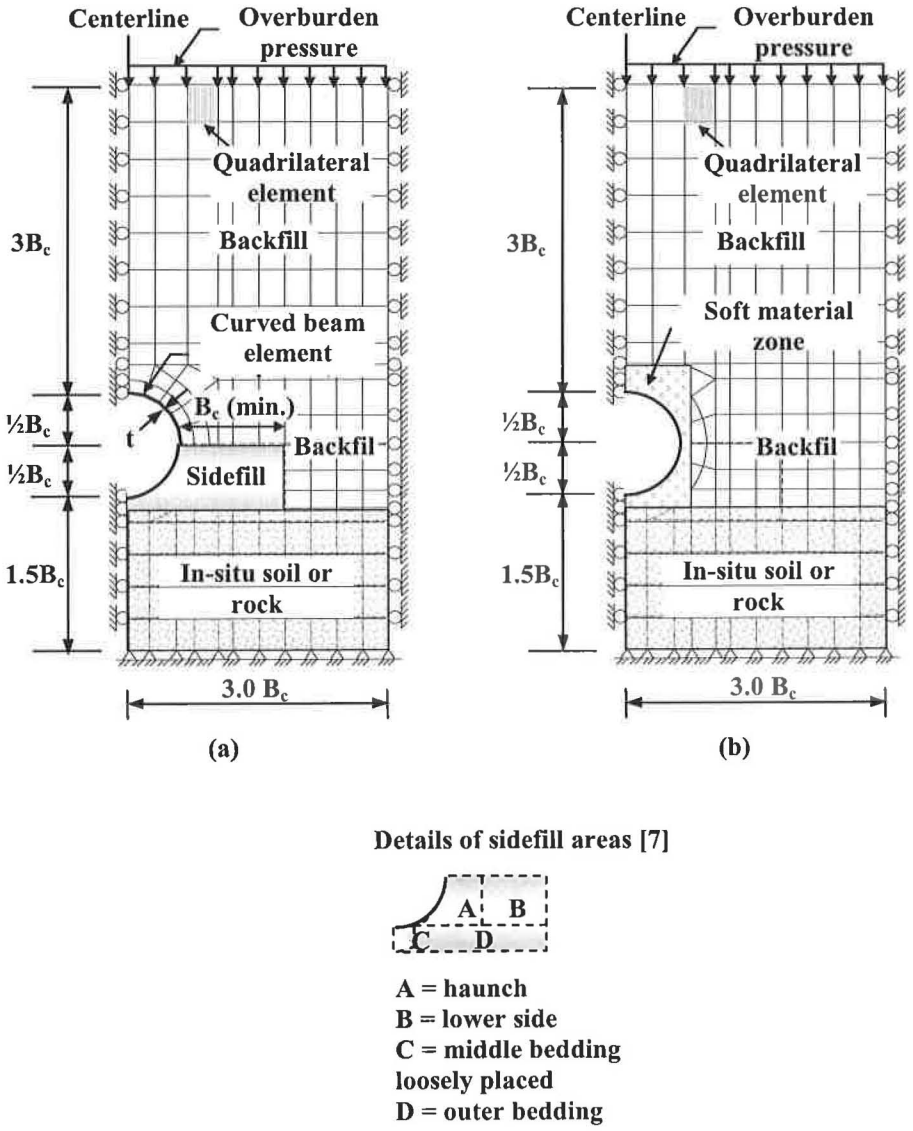

Figure 3.8: Schematic finite element model: (a) embankment installation and (b) imperfect trench installation (B_c = width of the pipe; t = pipe wall thickness)

The unit weight of soil was assumed to be 19 kN/m^3 (120 pcf). Nonlinear soil behavior was approximated by incremental analyses, i.e., by changing soil property values as backfill is placed and compacted. Values of tangent modulus and Poison's ratio were computed for each layer by using Equations 3.21 and 3.22 based on the assumption that soil layers are in principal stress states.

$$\sigma_1^{(i)} = \gamma_i (H_i / 2) + \sum_{j=j+1}^{n} \gamma_j H_j \tag{3.21}$$

$$\sigma_3^{(i)} = K_0 \sigma_1^{(i)} \tag{3.22}$$

where $\sigma_1^{(i)}$ = maximum principal stress in ith layer of soil (numbering commences from the bottom to the top of the backfill); $\sigma_3^{(i)}$ = minimum principal stress in ith layer of soil; H_i = depth of ith soil layer; γ_i = density of ith soil layer; and K_0 = coefficient of lateral earth pressure. These values are substituted for the principal stresses in Equation 3.8 for tangent modulus (E_t) and in Equation 3.20 for bulk modulus (B) for each layer. Poison's ratio (ν) is then computed by Equation 3.18. Soil parameters, such as the internal friction angle and soil cohesion used in Duncan and Selig's formulations, are available for a variety of soil types in the Concrete Pipe Technology Handbook [15] and also in the CANDE-89 User Manual [12]. Although variations of the soil properties for each layer used to simulate the nonlinear behavior of soil in the analysis using ABAQUS and MSC/NASTRAN appears to be haphazard, the numerical results compared with those from SPIDA and CANDE-89 for simple test cases correlate very well. Typical sample comparisons are discussed in detail in the next chapter. Such time consuming and laborious procedures were dictated by the aforementioned limitations with regard to the backfill height and mesh generation schemes imposed in SPIDA and CANDE-89 for deeply buried pipes.

In the past, materials such as baled hay or straw, and sawdust were tried in the soft zone ITI. However, these materials left unanticipated large holes after they decomposed and, consequently, the use of ITI methods were perceived to be unreliable despite their theoretical soundness. Because of the availability of modern non-bio-degradable materials such as expanded polystyrene blocks (geofoam), polystyrene beads (a.k.a. peanuts), legitimate concerns have been largely overcome. McAffee and Valsangkar [49] reported experimentally measured modulii of lightweight materials ranging from 345 kPa (50 psi) for geofoam to 2,756 kPa (400 psi) for bales of hay. Poisson's ratio for geofoam is generally less than 0.1. Based on these two references, values of modulus of elasticity (E_s) of soft zone materials were varied between 345 kPa (50 psi) and 2,756 kPa (400 psi) and Poisson's ratio (ν) was assumed equal to 0.1.

3.3.2 Verification of Modeling Techniques

In order to assess the validity of the soil modeling techniques adopted, the analytical results from ABAQUS and MSC/NASTRAN, general purpose 3-D finite element codes, were compared with those of SPIDA and CANDE-89, special purpose computer codes for pipes.

1) Corrugated PVC pipes

The analytical results from ABAQUS were compared with those from CANDE-89, MSC/NASTRAN, and field tests on corrugated PVC pipe reported by Sargand et al. [50, 51] at the Ohio Research Institute for Transportation and Environment (referred to ORITE hereinafter). The corrugated PVC pipe had an inside diameter of 0.76 m (30 in.). The unit weight of backfill materials was 21.2 kN/m^3 (135 pcf) and the fill height was 12.2 m (40 ft). Figure 3.9 shows the radial pressure distributions from ABAQUS, MSC/NASTRAN, and CANDE-89 under the full-

bonded interface conditions. The maximum radial pressure from ABAQUS shows good agreement with those from CANDE-89 and MSC/NASTRAN with less than 5% differences. For the radial pressure at the pipe crown, data from ABAQUS under the full-bonded interface conditions showed good agreement with that from the field test with less than 10% differences as shown in Figure3.9.

2) Corrugated Steel Pipes

The example CSP for model verification has a diameter of 2 m (78 in.). The unit weight of backfill materials used in this comparison is 18.9 kN/m^3 (120 pcf) and the backfill height (H) is 24.4 m (80 ft). Figure 3.10(a) shows the radial pressure distributions from ABAQUS, MSC/NASTRAN, and CANDE-89. The maximum radial pressure from ABAQUS agrees well with those from MSC/NASTRAN and CANDE-89 with less than 7% difference.

The results from ABAQUS were also compared with those from field tests and numerical investigation by the Ohio Research Institute for Transportation and the Environment (ORITE) [52]. Figure 3.11 shows the construction of the multi-plate corrugated steel pipe. The diameter of pipe was 6.4 m (252 in.). The steel plates were 0.95 cm (0.375 in.) thick and had a 15.24 cm (6 in.) by 5.08 cm (2 in.) corrugation profile. As the diameter of the test pipe was very large, they incorporated the slotted joint [53]. In order to simulate the numerical model as close to the test condition as possible, a joint travel length (JTL) of 1.27 cm (0.5 in.) of the slotted joint was incorporated in the CANDE runs. Fig. 3-13 shows that the vertical earth pressures on the crown computed with ABAQUS were relatively close to those from CANDE-89 investigation by Sargand and Moreland [52].

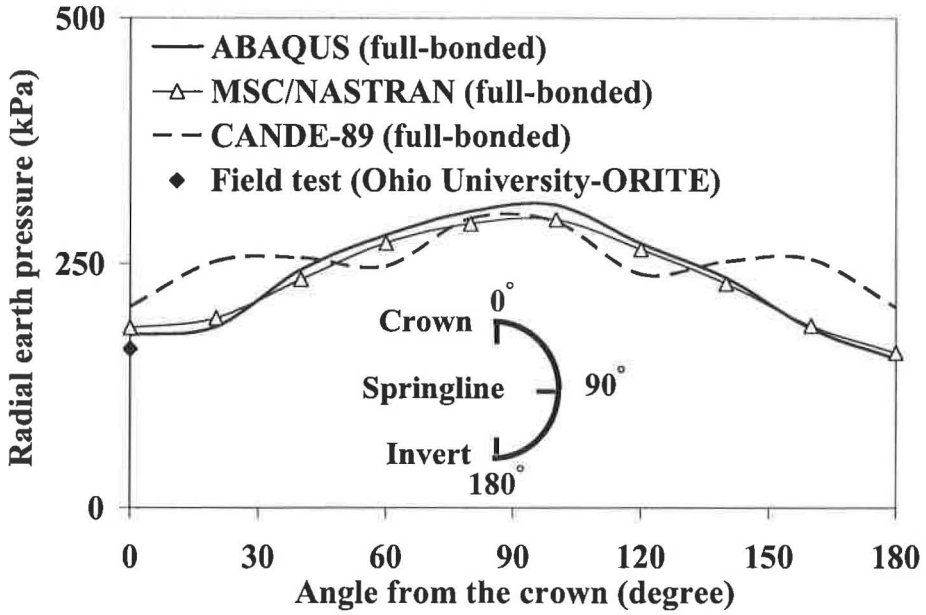

(a)

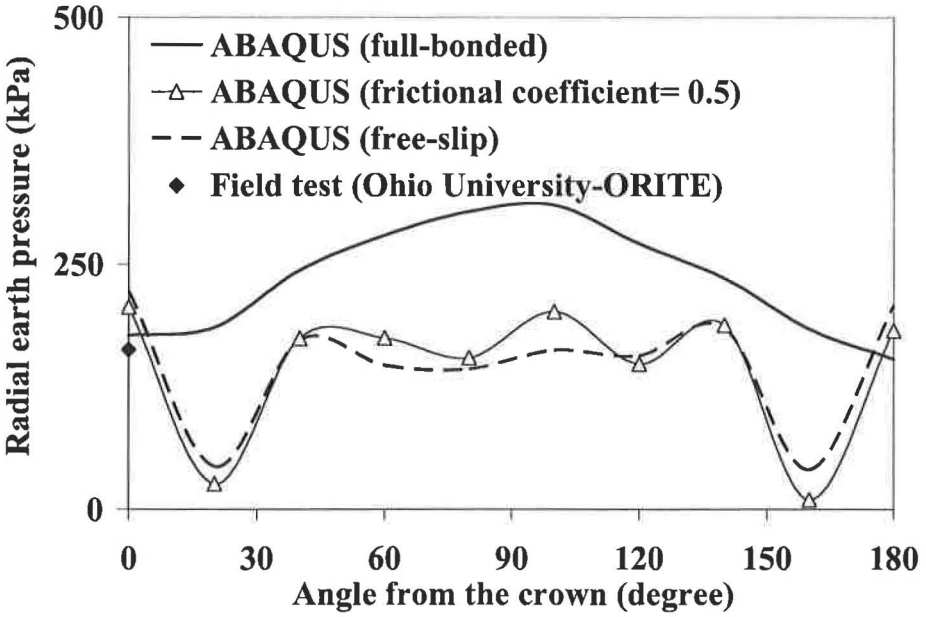

(b)

Figure 3.9: Finite element modeling versus field test by the Ohio Research Institute for Transportation and Environment (ORITE): (a) verification of modeling techniques and (b) effects of interface conditions (parameters: pipe diameter = 0.8 m; fill height = 12 m)

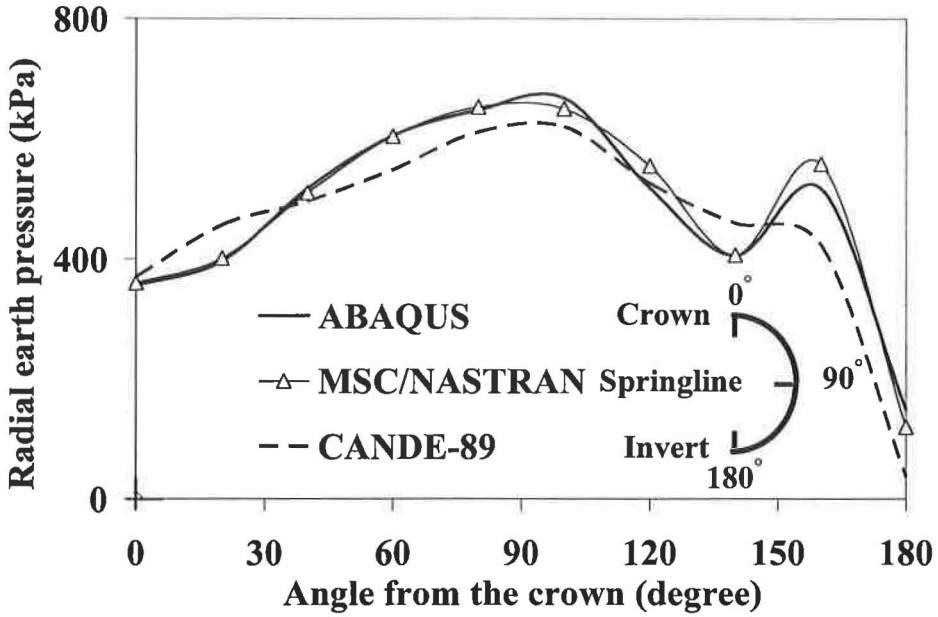

Figure 3.10: Comparison of radial earth pressures by ABAQUS, MSC/NASTRAN, and CANDE-89 (parameters: pipe diameter = 2 m; fill height = 24.4 m; interface condition= full-bonded)

Figure 3.11: Multi-plate corrugated steel pipe during construction [52]

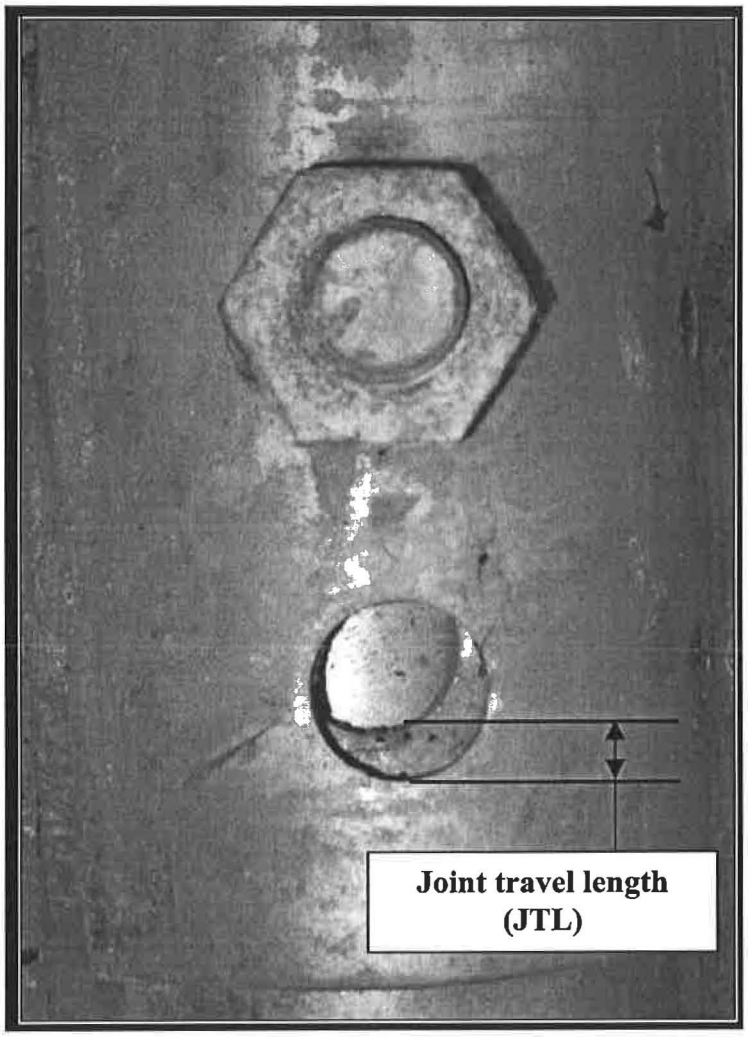

Figure 3.12: Slotted joint [52]

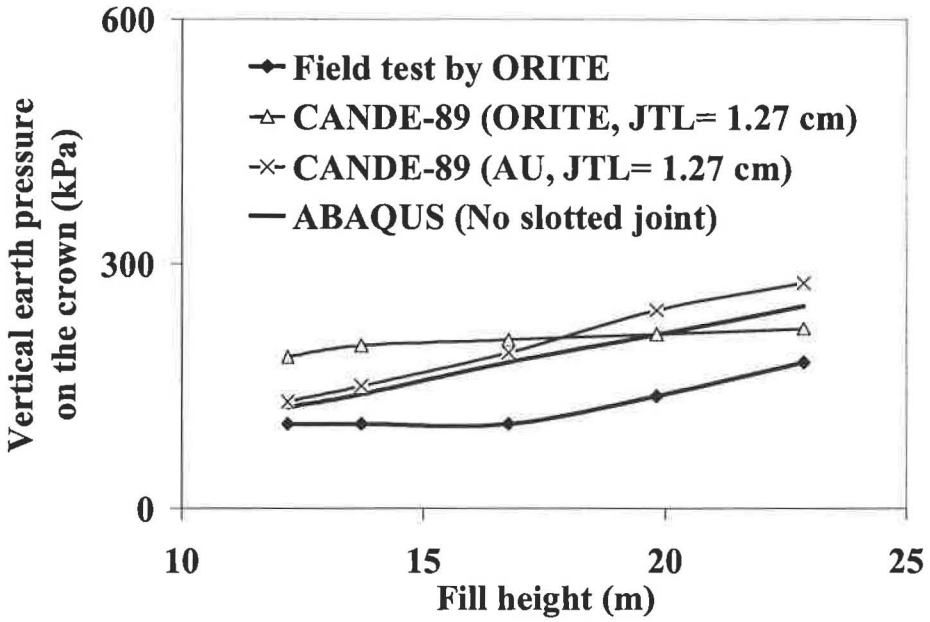

Figure 3.13: FEM vs. field tests by the Ohio Research Institute for Transportation and the Environment (ORITE) (D= 6.4m, JTL= joint travel length, AU= Auburn University)

3.4 Optimum Geometry of Imperfect Trench Installations

The single most important original contribution of this study is the optimization of the geometry of the soft material zone in ITI. Although the notion of placing soft lightweight materials above a deeply buried pipe in order to lessen the earth loads on the pipes has been available nearly the past one hundred years, none has ever successfully come up with an optimum geometry of the soft material zone. Further, no information on the quantitative assessment of the effectiveness of the ITI has been available.

Kim and Yoo [35] presented an improved geometry for the soft material zone. They, however, overlooked the development of unexpectedly large shearing stresses. It was found during this study that these unexpected shearing stresses can effectively be eliminated by extending the soft material zone down to the bottom of a pipe as illustrated schematically in Figure 4.3. The effectiveness of the reduction of the earth pressure on the deeply buried pipes installed under the optimum geometry of the ITI is truly outstanding. The highest reduction rate observed during the analysis of well over 600 hypothetical models is 85% of the anticipated earth pressure for the pipe in ordinary embankment installations. The detailed dimensions of the extended soft material zone geometry are slightly different reflecting the particular characteristic of PVC pipes and CSP. The detailed dimensions and the effectiveness of reducing the unexpected shearing stresses for each of these two major conduits will be entailed in the subsequent chapters.

CHAPTER 4

ANALYSES FOR CORRUGATED PVC PIPES

4.1 Soil-Structure Interaction

4.1.1 Finite Element Modeling

PVC has stress-strain relationships that are nonlinear and time dependent. The initial modulus of elasticity (E_{ini}, short-term), minimum 50-year modulus of elasticity (E_{50}, long-term), Poisson's ratio (ν), and unit weight (γ) of PVC materials were taken to be 2.75 GPa (400 ksi), 0.96 GPa (140 ksi), 0.30, and 9.3 kN/m^3 (59 pcf), respectively, from AASHTO LRFD [7]. Kim and Yoo [35, 54] and McVay [37] reported that the effect of interface behavior was insignificant for soil-structure interaction of rigid conduits. Sargand et al. [55] installed and monitored the response of 18 deeply buried thermoplastic pipes. The field study by Sargand et al. [55] showed that the loads on corrugated PVC pipes were predicted more closely by the full-bond interface model. As will be shown later, however, the vertical arching factors, VAF, of flexible conduits appear to be significantly affected by the assumed interface conditions. In order to clarify the effects of the interface conditions for the corrugated PVC pipes, this study examined three interface conditions: full-bonded (with a coefficient of friction equal to infinity), frictional slip (with a coefficient of friction equal to 0.5), and free-slip (with a coefficient of friction equal to zero).

4.1.2 Effects of Sidefill Material Properties

It is reported and this study confirms that the surrounding sidefill (haunch area and lower side) for a flexible pipe provides considerable support. If the sidefill is uncompacted, the support

becomes weak. Figure 4.1 shows that the sidefill of gravelly sand (SW90 or SW95) (gravelly sand compacted to 90% or 95% of maximum density per AASHTO [56]) is more efficient than that of silty sand (ML90 or ML95) or silty clay (CL90 or CL95) in reducing the earth load on the pipe. This is due to the higher value of modulus of soil reaction of gravelly sand than that of silty sand and/or silty clay. AASHTO LRFD [39] specifies gravelly sand compacted to 90% standard proctor as a minimum requirement for backfill of corrugated PVC pipes.

The numerical analyses in this study were executed using several different compaction values including the SW90. However, in the comparative study with AASHTO LRFD [7], the SW90 conditions was used.

4.1.3 Effects of Interface Conditions and Time-Dependent Properties

Values determined from FEA were compared (Figure 4.2) with those obtained from equations by Burns and Richard [16] and AASHTO LRFD [7]. Figure 4.2 shows that the arching factors were affected by *H/D*, interface conditions, and the time-dependent material properties of corrugated PVC pipes. Deflections, however, were hardly affected by interface conditions and time-dependent material properties. Figure 4.2 indicates the following trends:

- In the case of *VAF* for short-term properties, FEA showed that the *VAF* by ABAQUS for the full-bonded interface conditions are in good agreement with those by the AASHTO LRFD equations where the interface conditions are not considered. The *VAF* computed with ABAQUS and AASHTO LRFD are close to those computed for full-bonded and free-slip interface conditions according to procedures suggested by Burns and Richard.

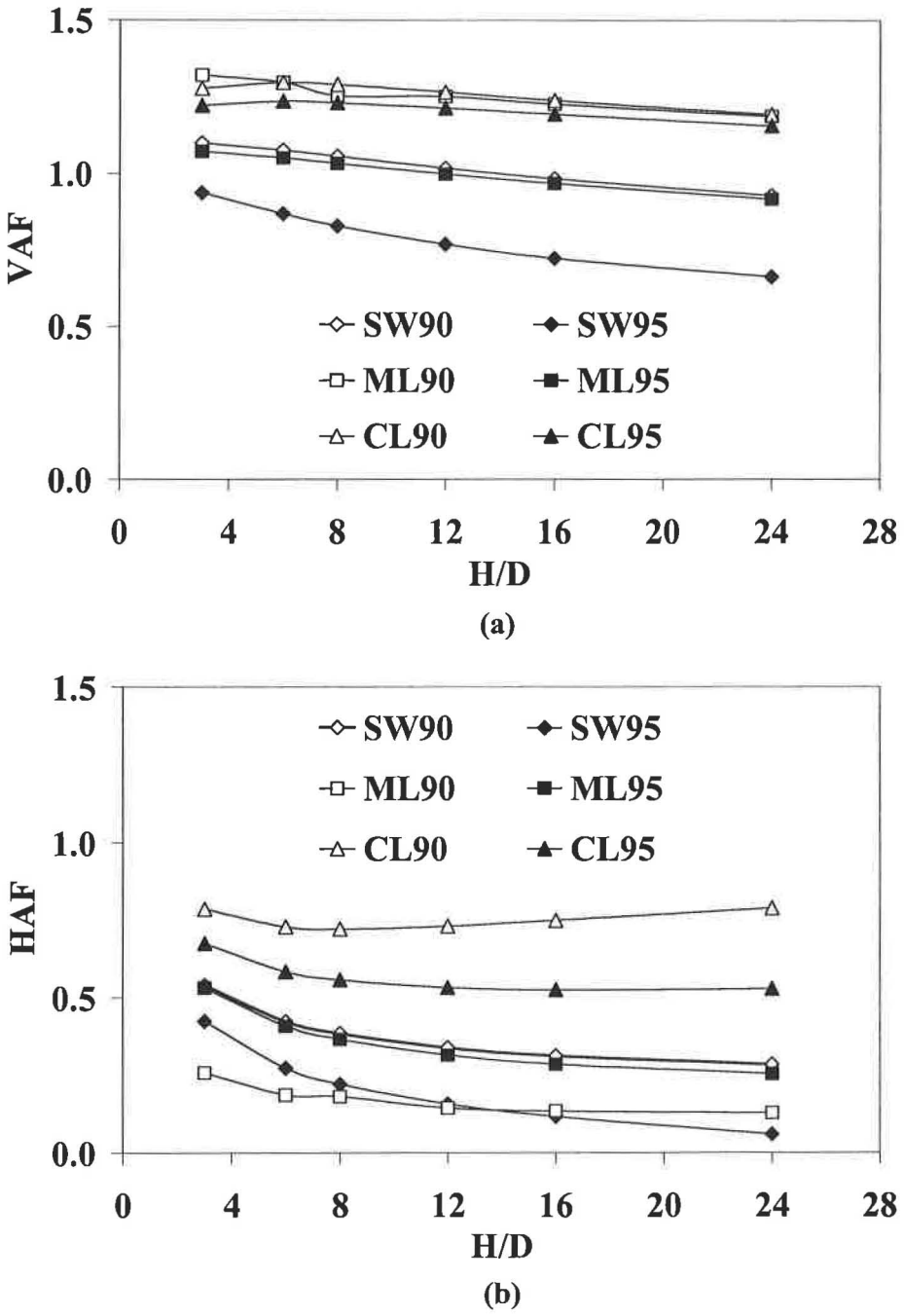

Figure 4.1: Effects of the properties of backfill material: (*a*) *VAF* versus *H/D* and (*b*) *HAF* versus *H/D*

- In the case of *VAF* evaluated with long-term properties of PVC, values determined with ABAQUS under full-bonded interface condition are fairly close to those evaluated from Burns and Richard equations under the free-slip interface condition.
- *VAFs* evaluated with ABAQUS decrease slightly as the ratio of the fill height to the pipe diameter (*H/D*) increases.
- *VAFs* determined with ABAQUS under frictional slip and free-slip interface conditions are 25% and 45% less, respectively, than those under the full-bonded interface condition. *VAFs* computed from Burns and Richard equations under the free-slip interface condition are 26% less than *VAFs* under the full-bonded interface condition.
- Although the interface effect on *VAF* in flexible conduits is fairly significant, the degree of the interface effect cannot be determined by analysis alone. A well designed field testing program is needed to assess this question. A conservative approach of full bond is an intermediate option.
- The deflections from ABAQUS were much less than those computed with Spangler equation [2] while they were relatively close to those from the Burns and Richard [16] deflection equations, as shown in Figures 4.2(c). The results from the ABAQUS and Burns and Richard deflection equations, also, showed that the interface conditions have insignificant effects on the deflections of corrugated PVC pipes. This observation is attributable to the fact that the deflection is primarily controlled by the earth pressure at the crown which is not sensitively affected by the interface conditions while *VAFs* in flexible conduits are measured as the sum of the axial stress and the bending stress at the springline where the interface conditions play an important role.

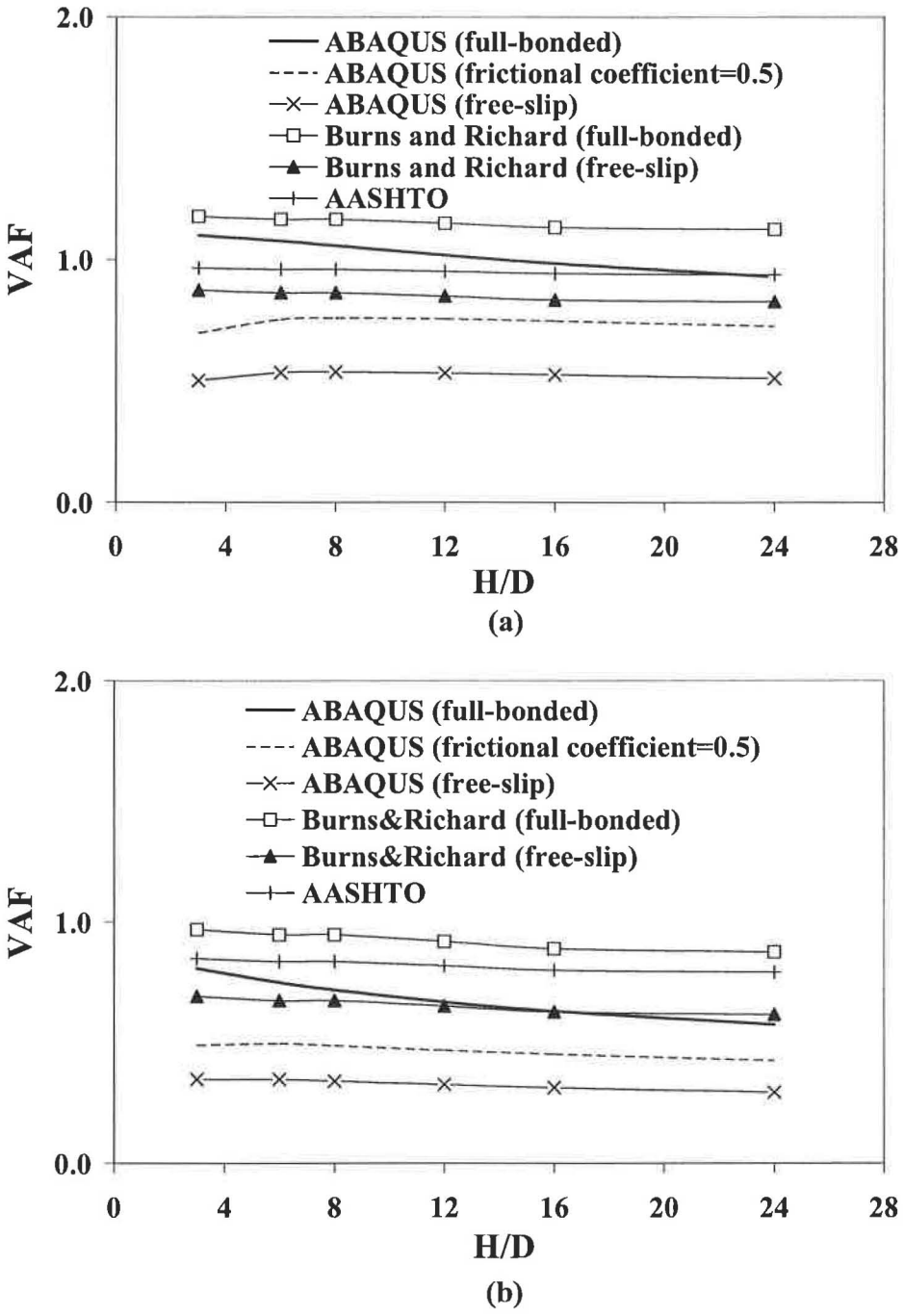

Figure 4.2: Finite element analyses versus current design equations: (*a*) *VAF* versus *H/D* (short-term) and (*b*) *VAF* versus *H/D* (long-term) (parameters: pipe diameter = 0.6 m) (continued)

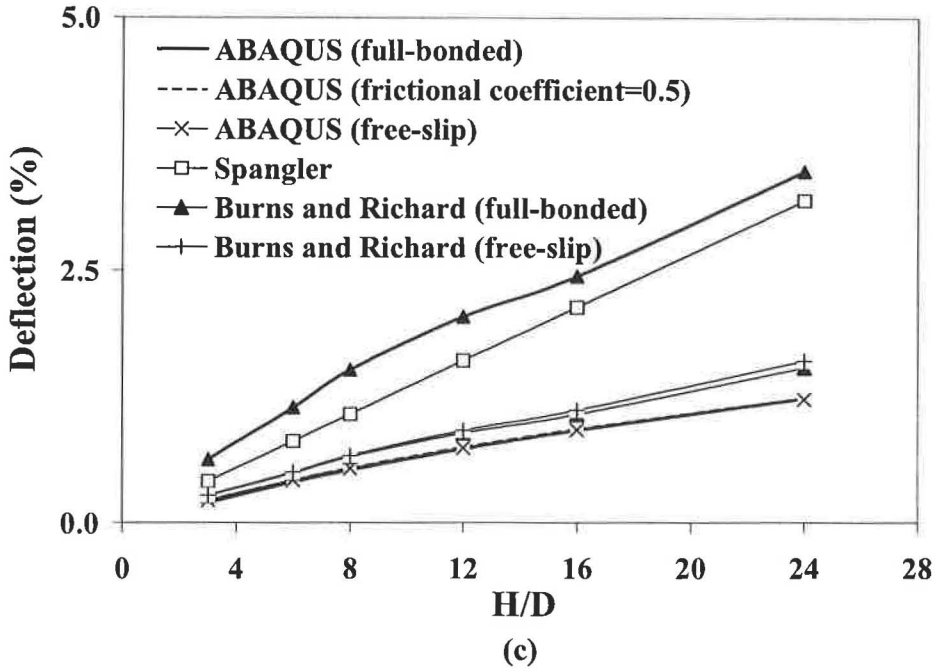

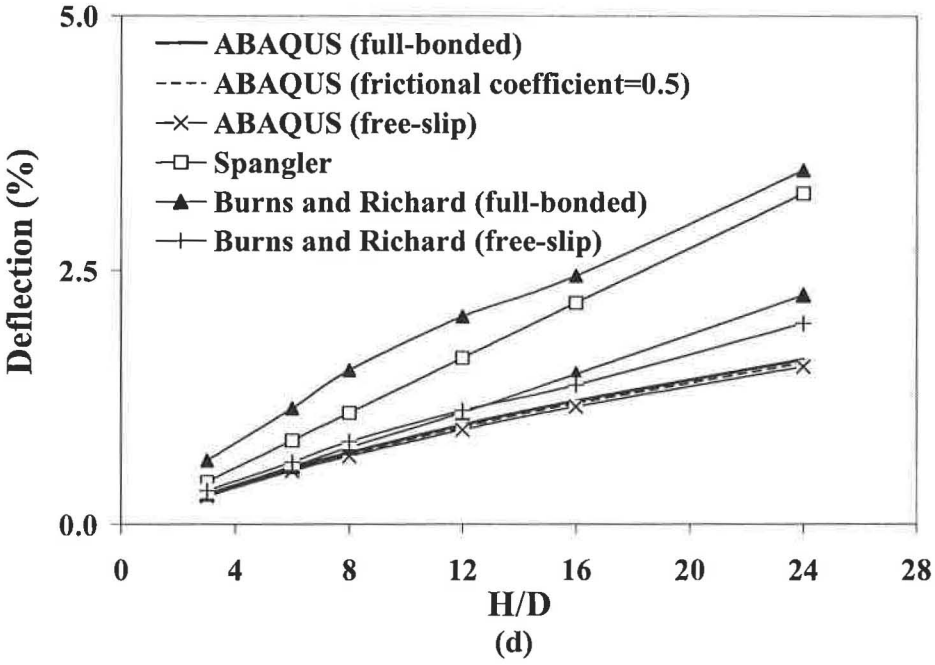

Figure 4.2: Finite element analyses versus current design equations: (*c*) deflection versus *H/D* (short-term) and (*d*) deflection versus *H/D* (long-term) (parameters: pipe diameter = 0.6 m; deflection lag factor (D_L) = 1; bedding factor (K_b) = 0.1)

4.2 Imperfect Trench Installation

4.2.1 Optimization of Soft Zone Geometry

The soft zone geometry is traditionally defined by three parameters; width, W; height, H_s; and the distance from the top of the pipe to the bottom of the soft zone, H' (Figure 4.3(a)). Figure 4.3(a) shows a schematic for an ITI as suggested by Spangler [23] and Vaslestad et al. [30]. Vaslestad et al. [30] also studied a geometry shown in Figure 4.3(c). As discussed elsewhere in this report, the ITI geometry shown in Figure 4.3(c) produces unexpectedly large shearing stresses along the side of the pipe. Based on a large number of parametric studies (over 300 cases), the soft zone geometry, as shown in Figure 4.3(b), was found to be the most effective in reducing the earth pressure. The soft zone in Figure 4.3(c) was also found to be more effective than that shown in Figure 4.3(a).

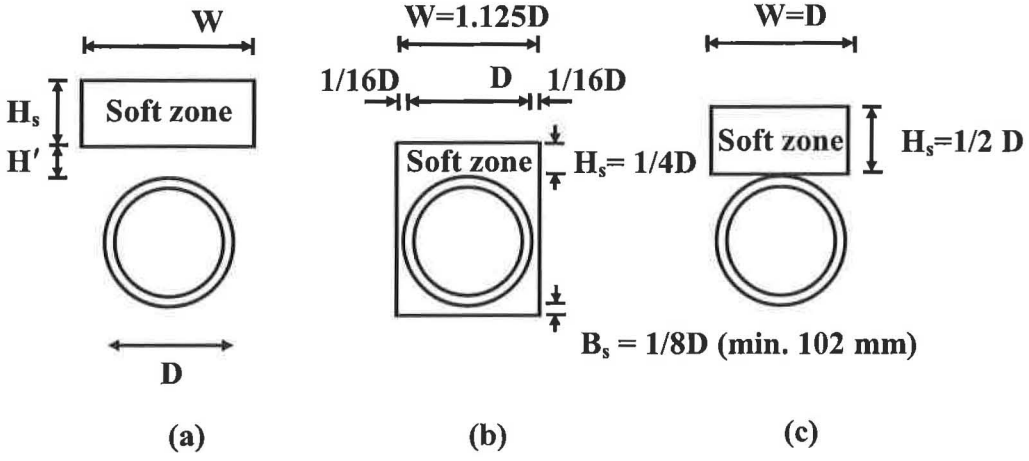

Figure 4.3: Notation for imperfect trench installations and geometries of soft zone: (*a*) notation, (*b*) soft zone geometry (proposed), and (*c*) soft zone geometry (tried by Spangler [23] and Vaslestad et al. [30])

The basis for concluding that the geometry given in Figure 4.3(b) is most efficient is illustrated in Figure 4.4. The reduction rate, R_{ms}, (to be incorporated in maximum wall stress) remains virtually unchanged once the height of the soft zone divided by the outside diameter of the pipe reaches 0.25 as shown in Figure 4.4(a). Figure 4.4(b) gives the reduction rate as a function of the width of the soft zone. As can be seen from Figure 4.4(b), the maximum reduction rate of the pipe wall stress occurs when the width of the soft material zone is slightly wider than the pipe diameter. This occurrence is due to the loss of lateral support by the sidefill that increases the bending moment at the springline. This is a significant difference between the behavior of rigid pipe and flexible pipes. In the case of rigid pipes, the reduction rate continues to increase as the width of the soft zone increases. As can be seen from Figure 4.5(b), there must be a soft material zone around the springline in order to avoid the development of high shear. At the same time the width of the soft material zone needs to be slightly larger than the diameter as shown in Figure 4.3(b). An optimum compromise for these seemingly reverse trends is to make the width of the soft material zone is equal to be the pipe diameter plus 1/8 times the pipe diameter, D. Bedding thickness of 1/8 D at the invert is recommended as the curve in Figure 4.3(c) shows only slightly larger reduction rates (R_{ms}) for the ratio of bedding thickness to pipe diameter (B_s / D) greater than 1/8 D. Figure 4.5 shows that the optimum soft zone geometry is highly effective in reducing the loading of corrugated PVC pipes. Geofoam (E_s = 345 kPa and $\nu = 0.1$) was used in all model analyses shown in Figures 4.4 and 4.5.

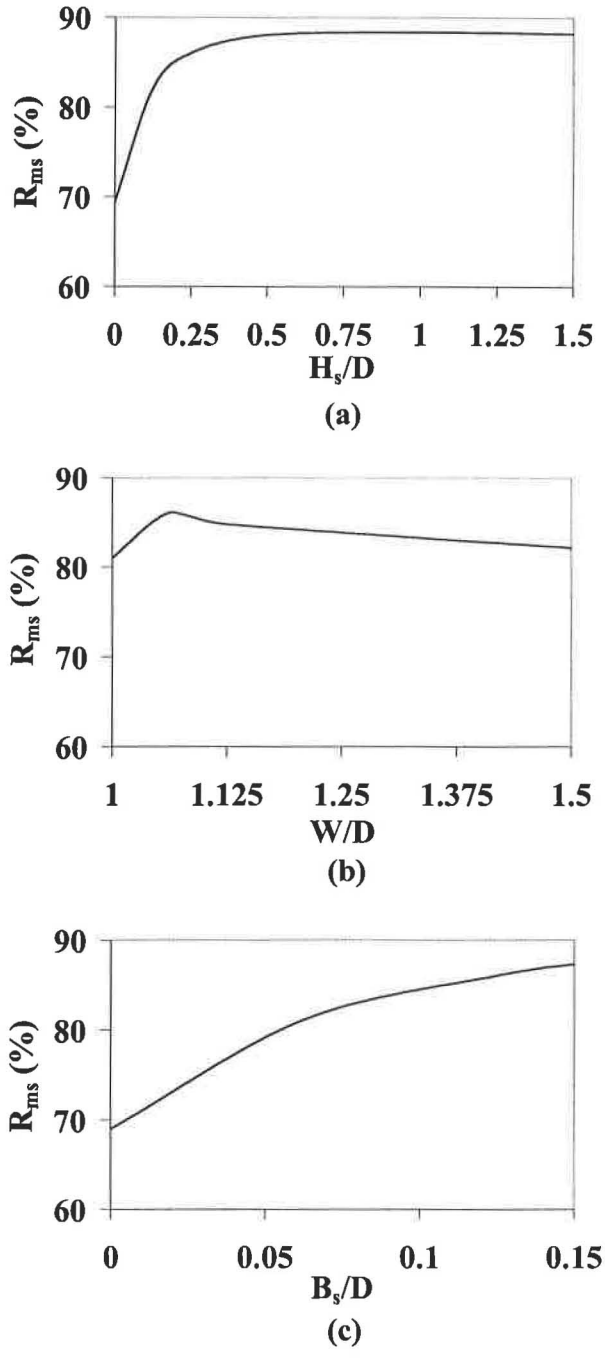

Figure 4.4: Optimization process of soft zone geometry: (a) height of soft zone (H_s) with $W/D = 1.125$ and $B_s/D = 0.125$, (b) width of soft zone (W) with $H_s/D = 0.25$ and $B_s/D = 0.125$, and (c) bedding thickness of soft zone (B_s) with $H_s/D = 0.25$ and $W/D = 1.125$ (R_{ms} = reduction rate of maximum wall stress)

4.2.2 Imperfect Trench Installation versus Embankment Installation

Figure 4.5(b) shows that, when soft zones are included, significantly different patterns of shear stresses develop on the pipe sidewall due to an alteration of the soil movement relative to the pipe. In the case of an embankment installation, positive shearing stresses (in the clockwise tangential direction) develop above the springline while negative shearing stresses (in the counter-clockwise tangential direction) develop below the springline. The shear forces resulting from these shear stresses act in opposite directions and are nearly equal in magnitude. This means there is no significant axial force increase at the springline of the pipe.

For the soft zone geometry as shown in Figure 4.3(c), the radial pressure at about 25 degrees from the invert was significantly larger than that at the crown, as shown in Figure 4.5(a). One effective measure found to remedy this was to extend the soft zone to the bedding as shown in Figure 4.3(b). This significantly decreases the radial pressure on the pipe as shown in Figure 4.5(a). The superb reduction in loading on the pipe for the proposed soft zone geometry is evident in Figure 4.5.

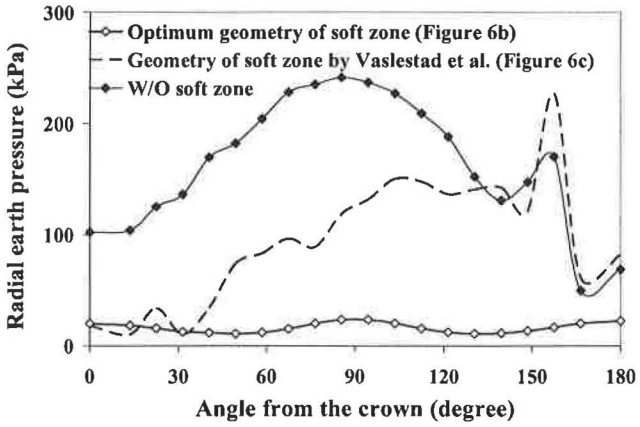

(a)

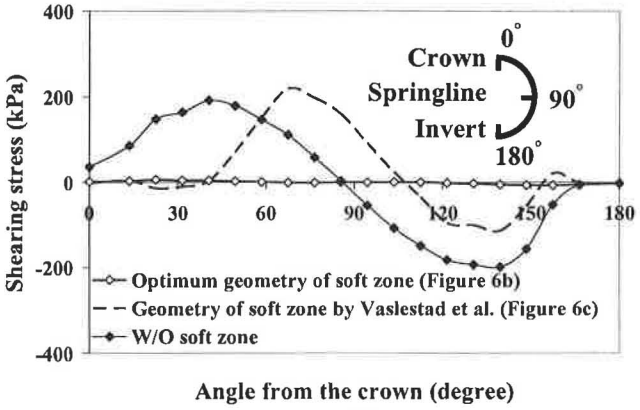

(b)

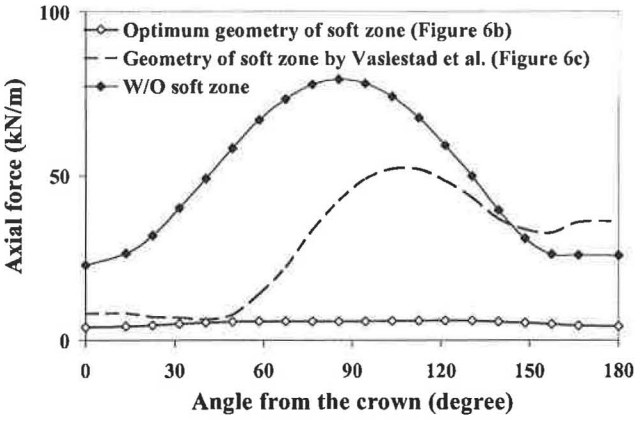

(c)

Figure 4.5: Imperfect trench installations versus embankment installation: (*a*) radial earth pressure, (*b*) shearing stress, and (*c*) axial force (parameters: pipe diameter = 0.6 m; short-term material properties; fill height = 15 m; modulus of elasticity of the lightweight material = 345 kPa) (continued)

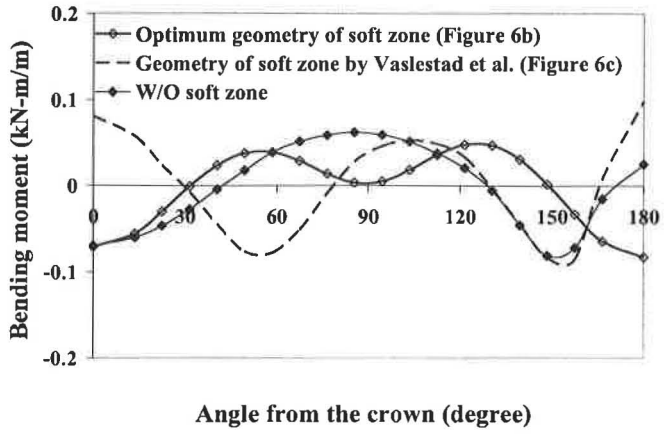

(d)

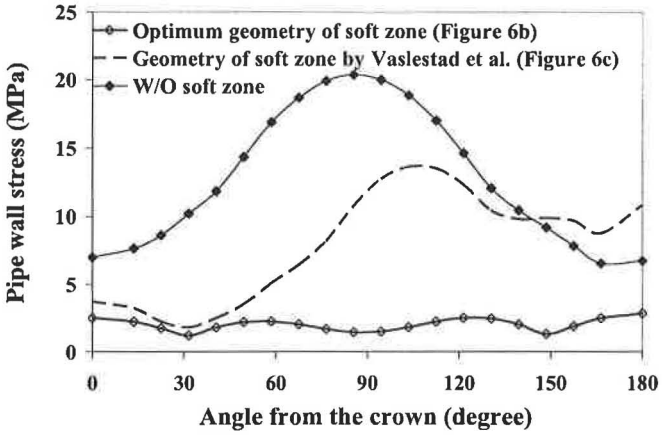

(e)

Figure 4.5: Imperfect trench installations versus embankment installation: (*d*) bending moment and (*e*) pipe wall stress (parameters: pipe diameter = 0.6 m; short-term material properties; fill height = 15 m; modulus of elasticity of the lightweight material = 345 kPa)

4.3 Predictor Equations

4.3.1 Arching Factor, Deflection, and Maximum Wall Stress

More than 300 hypothetical models were run to formulate linear regression equations for predicting arching factors, deflections, and maximum wall stresses based on embankment installations. The models assumed full-bond between pipes and soil. Figure 4.6 shows that the arching factors, deflections, and maximum wall stresses are affected by the ratio of the pipe diameter to radius of gyration (*D/r*) and time-dependent PVC modulus as well as *H/D*. Therefore, *H/D*, *D/r*, and time-dependent PVC modulus were variables in predictor equations, Equations 4.1 through 4.3. Based on recommendations in, AASHTO LRFD [7], values of *D/r* were varied between 60 and 100. The *D/r*, however, has insignificant effects on the maximum wall stresses and *D/r* is excluded from the predictor equation for maximum wall stresses, Equation 4.4.

$$VAF = \left[-0.008\frac{H}{D} + 1.124\right] / \left(\frac{D}{77r}\right)^{0.538} \quad \text{for short-term material properties} \qquad (4.1a)$$

$$VAF = \left[-0.011\frac{H}{D} + 0.816\right] / \left(\frac{D}{77r}\right)^{0.961} \quad \text{for long-term material properties} \qquad (4.1b)$$

$$HAF = 0.744\left(\frac{H}{D}\right)^{-0.310} / \left(\frac{D}{77r}\right)^{0.961} \quad \text{for short-term material properties} \qquad (4.2a)$$

$$HAF = 0.578\left(\frac{H}{D}\right)^{-0.489} / \left(\frac{D}{77r}\right)^{1.782} \quad \text{for long-term material properties} \qquad (4.2b)$$

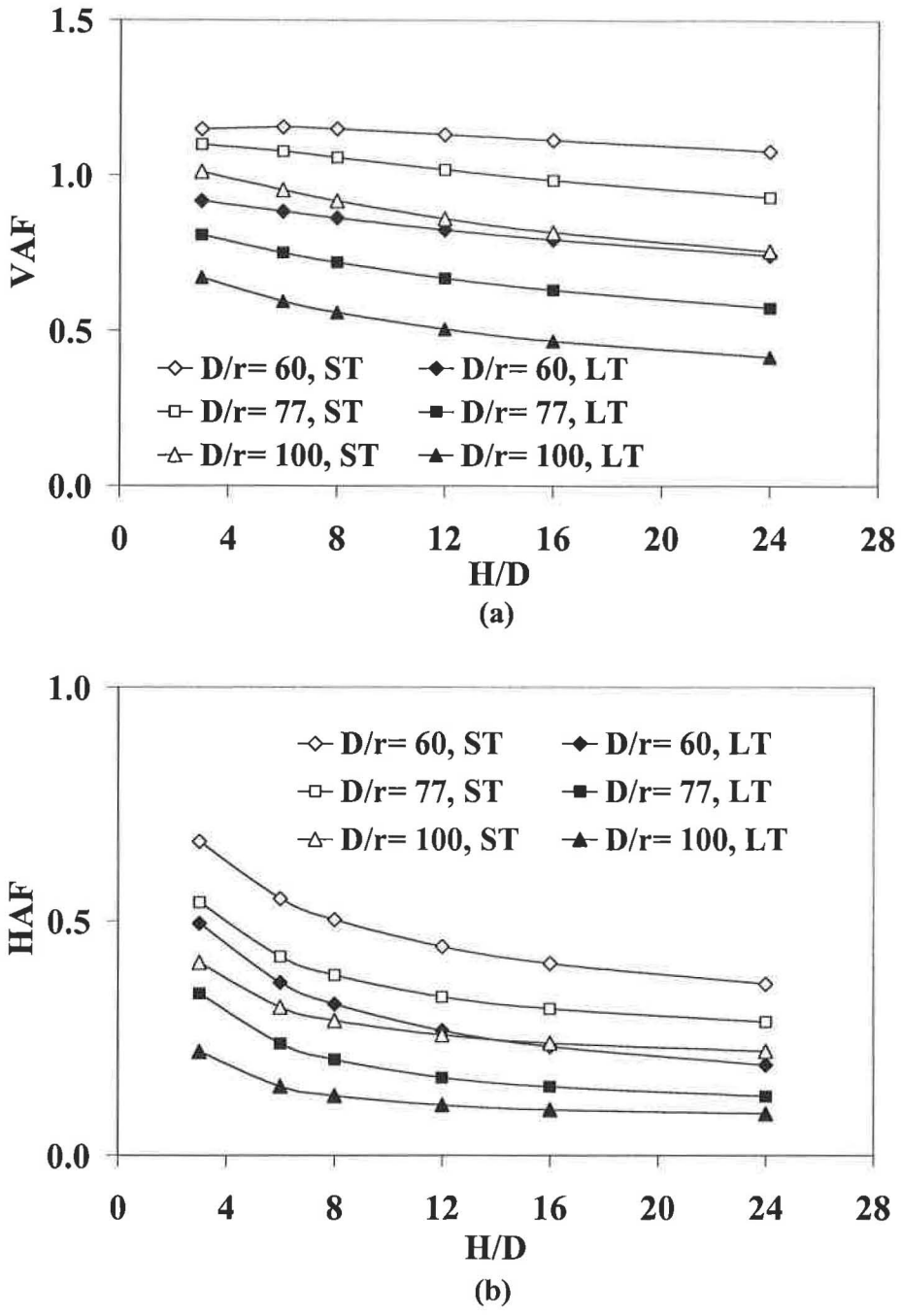

Figure 4.6: Predictor equations of arching factors, deflection, and soil-structure interaction multiplier (F_{ms}) for maximum wall stress: (*a*) *VAF* and (*b*) *HAF* (*D* = pipe diameter; *r* = radius of gyration of corrugation; *ST* = short-term material properties; *LT* = long-term material properties; modulus of elasticity of the lightweight material = 345 kPa) (continued)

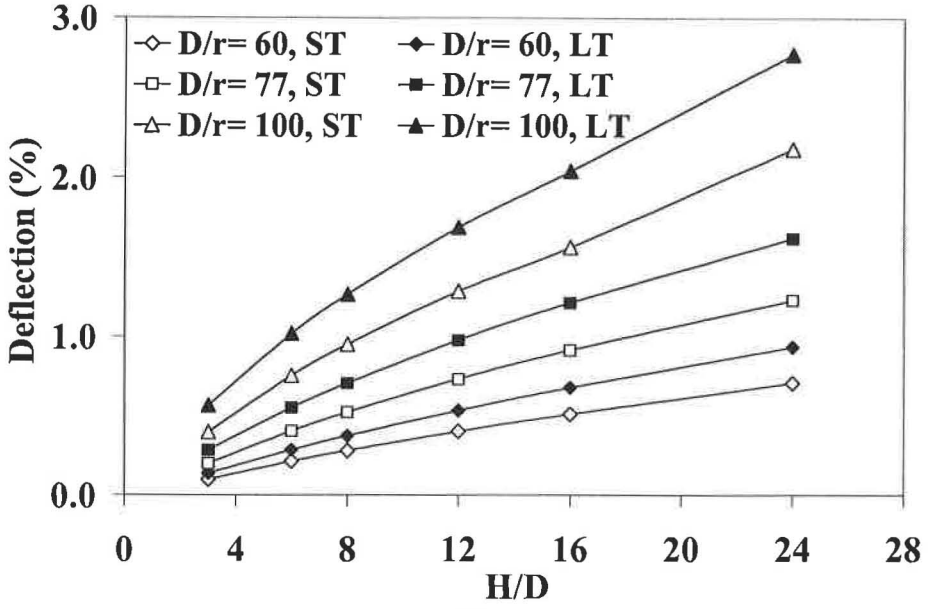

(c)

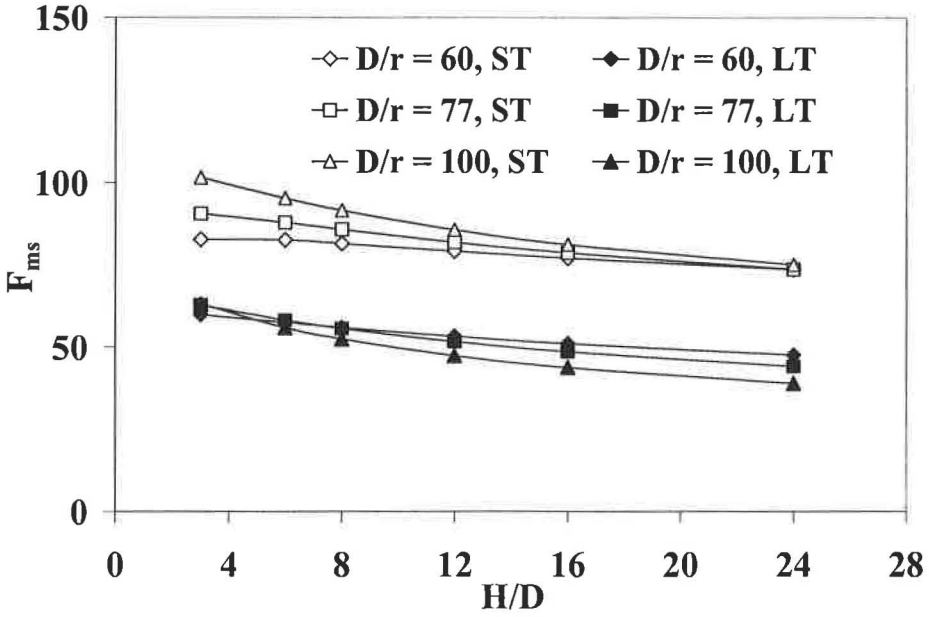

(d)

Figure 4.6: Predictor equations of arching factors, deflection, and soil-structure interaction multiplier (F_{ms}) for maximum wall stress: (*c*) deflection and (*d*) F_{ms} (D = pipe diameter; r = radius of gyration of corrugation; *ST* = short-term material properties; *LT* = long-term material properties; modulus of elasticity of the lightweight material = 345 kPa)

$$\frac{\Delta_y}{D}(\%) = \left[0.049\frac{H}{D} + 0.110\right]\left(\frac{D}{77r}\right)^K \quad \text{for short-term material properties} \quad (4.3a)$$

$$\frac{\Delta_y}{D}(\%) = \left[0.063\frac{H}{D} + 0.110\right]\left(\frac{D}{77r}\right)^K \quad \text{for long-term material properties} \quad (4.3b)$$

$$K = \left(\frac{H}{D}\right)^{0.33} \quad (4.3c)$$

$$F_{ms} = \left[-0.82\frac{H}{D} + 92.51\right] \quad \text{for short-term material properties} \quad (4.4a)$$

$$F_{ms} = \left[-0.87\frac{H}{D} + 63.51\right] \quad \text{for long-term material properties} \quad (4.4b)$$

where F_{ms} is the soil-structure interaction multiplier for maximum pipe wall stresses. Maximum pipe wall stresses, therefore, can be calculated by

$$\sigma_{\max} = F_{ms}\left(\frac{PL}{D}\right) \quad (4.5)$$

4.3.2 Reduction Rates

Figures 4.5(c) and 4.5(e) show that the axial force and maximum wall stresses are reduced by, respectively, 92% and 85% for ITI. This reflects that the reduction rate related to bending moment is only 18%, as shown in Figure 4.5(d). The geometry of the soft zone, *D/r*, *H/D*, time-dependent PVC modulus, and the modulus of elasticity and Poisson's ratio of the lightweight materials are variables affecting the reduction rates of the arching factors, deflections, and maximum wall stresses. After the three dominant geometric parameters of the soft zone were identified as shown in Figure 4.4, the remaining variables were varied in approximately 300 hypothetical models. An examination of the analysis results revealed that

D/r, *H/D*, and Poisson's ratio of the soft zone materials hardly affect the reduction rate of arching factors, deflections, and maximum wall stresses. Therefore, these three variables were not considered further in the development of predictor equations. The analyses indicated the reduction rates for the arching factors, deflections, and maximum wall stresses were sensitive to the modulus of elasticity of the soft zone material. Time-dependent PVC modulus had insignificant effects on the reduction rates of VAF, deflections, and maximum wall stress but did significantly affect HAF. Figure 4.7 shows that the reduction rates decreased as the modulus of elasticity of the soft zone material increases. This demonstrates that the soft zone material should have the lowest modulus of elasticity as practically possible. This is contrary to Tyler [31] who erroneously discounted the importance of the stiffness of the soft zone materials.

Predictor equations for the reduction rates resulting from the proposed soft zone geometry were derived with the linear regression method. The modulus of elasticity of the soft zone material is the only variable in Equations 4.6a through 4.6e, but Equations 4.6(b) and 4.6(c) are for, respectively, short and long term PVC modulus.

$$R_v = \left[-0.015E_s + 91.74\right] \tag{4.6a}$$

$$R_{hs} = \left[7\times10^{-6}E_s^{\,2} - 0.047E_s + 96.34\right] \tag{4.6b}$$

$$R_{hl} = \left[1\times10^{-5}E_s^{\,2} - 0.077E_s + 87.35\right] \tag{4.6c}$$

$$R_d = \left[9\times10^{-6}E_s^{\,2} - 0.048E_s + 49.67\right] \tag{4.6d}$$

$$R_{ms} = \left[-0.015E_s + 85.08\right] \tag{4.6e}$$

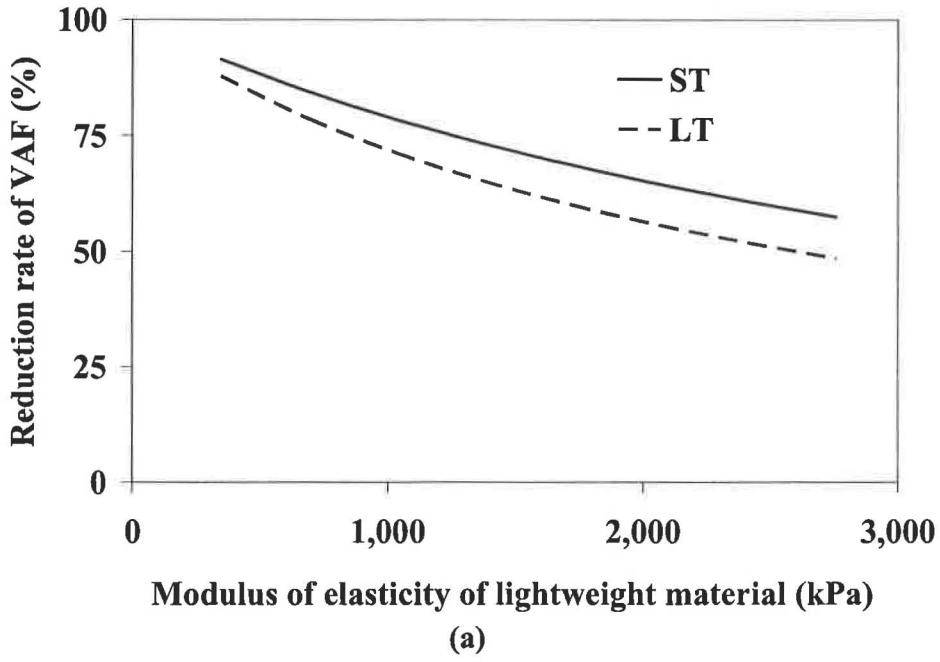

(a)

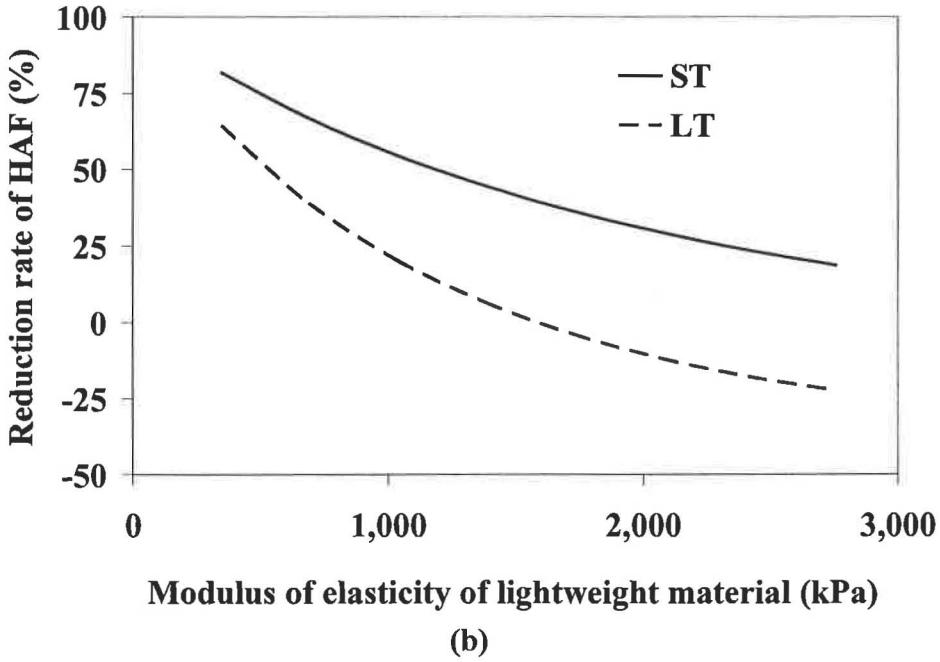

(b)

Figure 4.7: Predictor equations of reduction rates: (*a*) *VAF* and (*b*) *HAF* (*ST* = short-term material properties; *LT* = long-term material properties; σ_{ms} = maximum wall stress) (continued)

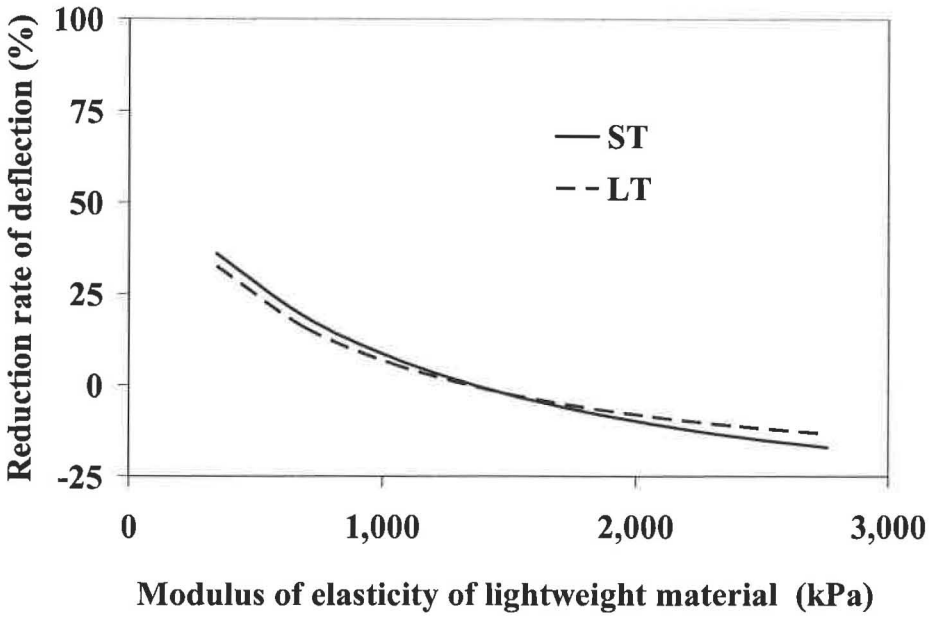

(c)

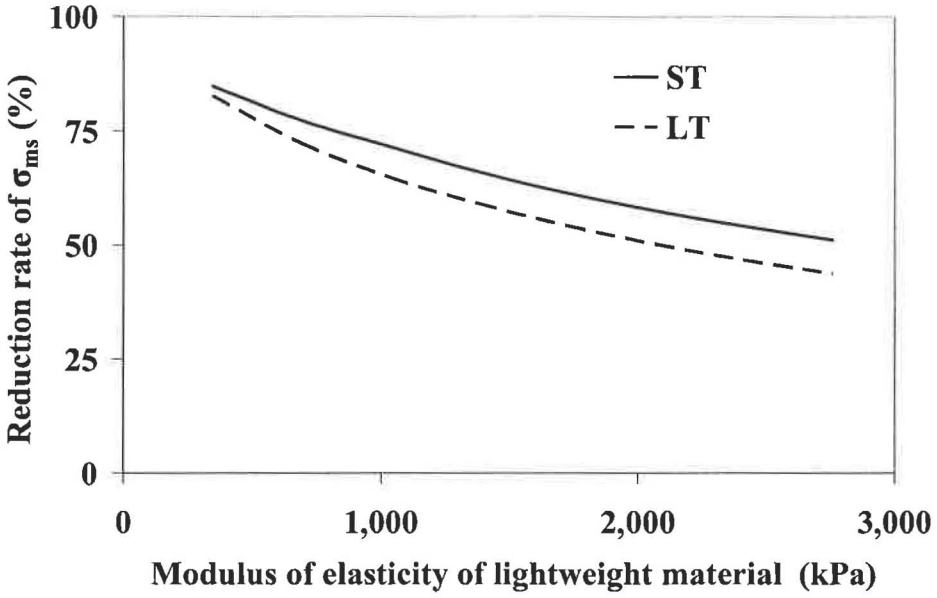

(d)

Figure 4.7: Predictor equations of reduction rates: (*c*) deflection and (*d*) maximum wall stress (*ST* = short-term material properties; *LT* = long-term material properties; σ_{ms} = maximum wall stress)

where R_v = vertical arching factor reduction rate (%); E_s = modulus of elasticity of lightweight materials (kPa); R_{hs} = horizontal arching factor reduction rate (%) for short-term material properties; R_{hl} = horizontal arching factor reduction rate (%) for long-term material properties; R_d = deflection reduction rate (%); and R_{ms} = maximum wall stress reduction rate (%).

CHAPTER 5

ANALYSES FOR CORRUGATED STEEL PIPES

5.1 Soil-Structure Interaction

5.1.1 Finite Element Modeling

The modulus of elasticity (E_p), Poisson's ratio (ν), and unit weight (γ) of steel were taken to be 200 GPa (29,000 ksi), 0.30, and 77 kN/m^3 (490 pcf), respectively, from AASHTO LRFD [7]. In order to clarify the effects of the interface conditions for CSP, this study examined three interface conditions: full-bonded (m= ¥), frictional slip (m= 0.5), and free-slip (m= 0).

5.1.2 Effects of Sidefill Material Properties

The surrounding sidefill for CSP provides considerable support. Therefore, sidefill compaction is critical for CSP performance. Figure 5.1 shows that the cohesionless backfill compacted to 90 or 95% of AASHTO T-99 maximum density (SW90 or SW95) is more efficient than similarly compacted silty (ML90 or ML95) or clayey backfill (CL90 or CL95) in reducing earth loads on the pipe. The cohesionless sidefill has higher modulus of soil reaction and provides higher lateral support. The effects of higher stiffness sidefill for CSP shown in Figure 5.1 are, however, not as significant as those shown in Figure 4.1 for PVC pipe. AASHTO LRFD [39] specifies the SW90 as a minimum requirement for CSP sidefill. The analyses were performed with several different soil types and compaction rates, including the SW90. However, only the AASHTO LRFD SW90 was used in the analyses that are compared with AASHTO LRFD [7] results shown in Figure 5.2.

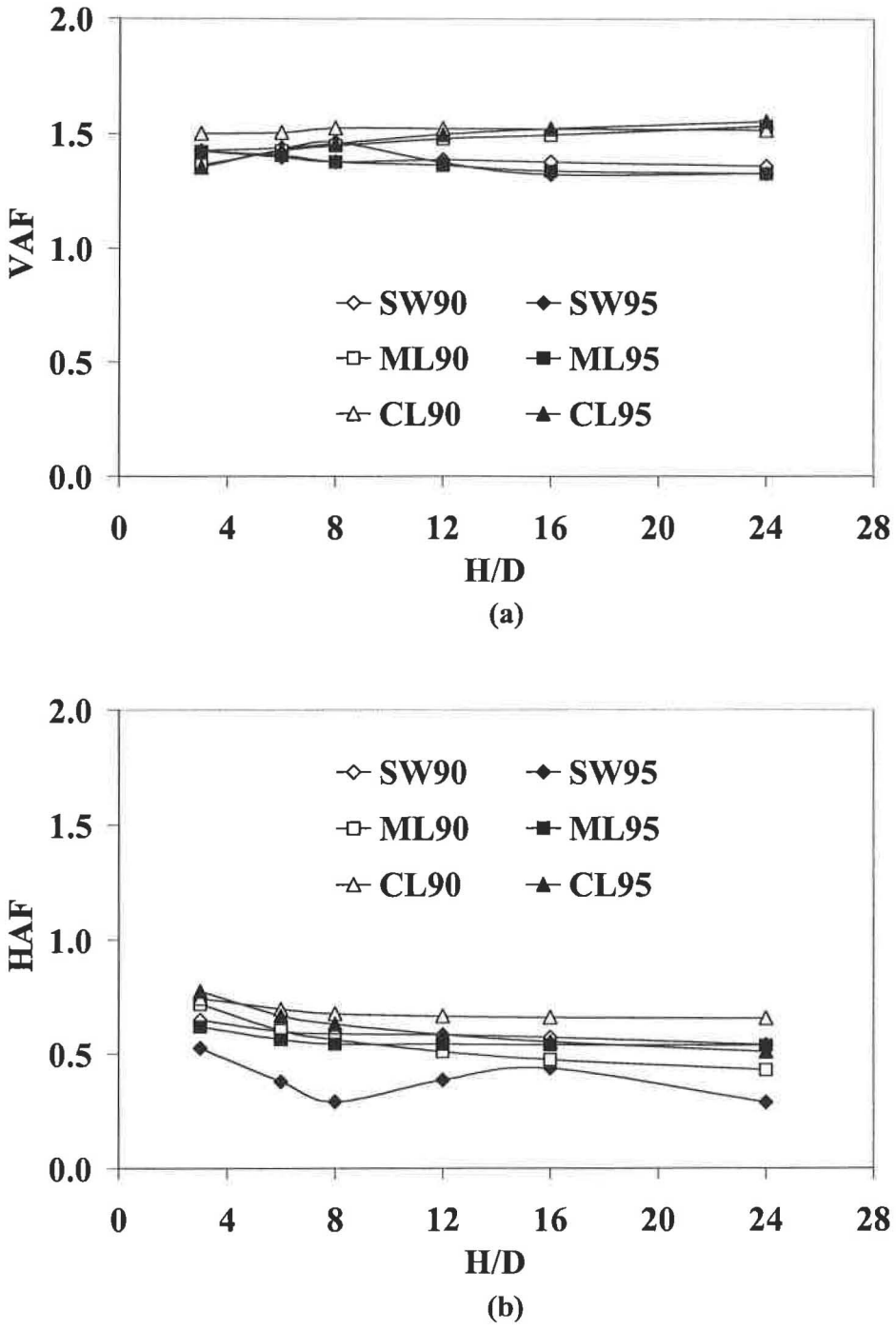

Figure 5.1: Effects of the properties of backfill material: (a) *VAF* versus *H/D* And (b) *HAF* versus *H/D* (parameter: interface condition= full-bonded)

5.1.3 Effects of Interface Conditions

Vertical arching factors determined from FEA were compared with those computed from available equations including those from AASHTO LRFD [7], Burns and Richard [16], and AISI [6]. Figure 5.2 shows that vertical arching factors were sensitively affected by interface conditions. With the full-bonded interface condition, *VAFs* by ABAQUS are in good agreement with those by Burns and Richard [16]. Also, *VAFs* by AASHTO LRFD [7] and Burns and Richard with the free-slip condition lie between the values computed by ABAQUS for frictional slip and free-slip interface conditions, respectively. *VAFs* by AASHTO are close to those computed by Burns and Richard equations under the free-slip interface condition. *VAFs* determined by ABAQUS for frictional slip and free-slip interface conditions are 18% and 39% smaller, respectively, than those for the full-bonded interface condition. *VAFs* computed from Burns and Richard equation for the free-slip interface condition are 22% smaller than those with the full-bonded interface condition.

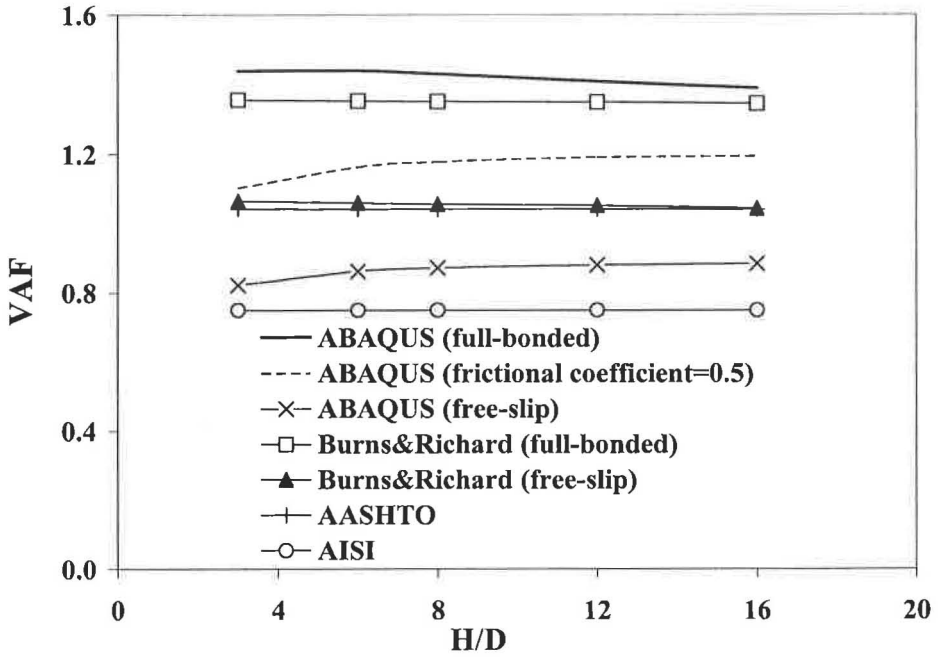

Figure 5.2: Variations of vertical arching factor (*VAF*)

Figure 5.3 illustrates the effects of interface conditions on the total vertical load, W_e, which is transformed into *VAFs* defined by Equation 2.1. As expected, Figure 5.3 correctly shows that the vertical load resulting from the radial pressure is not very sensitively affected by the interface condition while the vertical load exerted on the CSP due to shearing stress is quite sensitively affected by the interface condition. It is noted that the dead weight of the CSP is negligibly small fraction of the total vertical load. Although the effects of interface conditions on *VAFs* for CSP are significant (up to 34% of the total vertical load), they cannot be determined rationally by analysis alone. A well designed field testing program is needed to assess this question. As an intermediate option, it is recommended that *VAF* be computed with full-bonded interface condition.

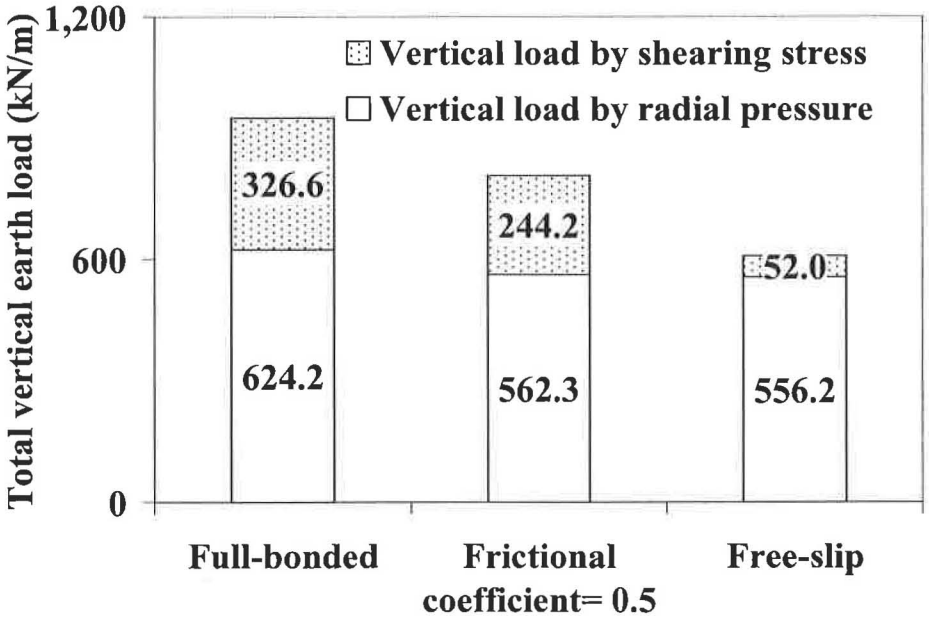

Figure 5.3: Effects of interface conditions for total vertical earth load (W_e) (parameters: pipe diameter = 2.4 m; fill height = 29 m)

Figure 5.4 shows that deflections are not affected very much by interface conditions. This observation may be attributable to the fact that the vertical load affecting the vertical deflection at the crown is the total earth load above the crown as opposed to the total vertical load at the springline shown in Figure 5.3. Hence, the total vertical load above the crown is not affected by the interface condition. Deflections from ABAQUS were much less than those computed from equations proposed by Spangler [2], Equation 2.7 and McGrath [17], Equation 2.9. Deflections from Burns and Richard equations, Equation 2.8a and Equation 2.8b, are close to those from ABAQUS. Although the deflection of the CSP rarely controls the design, it may control performance criteria (Article 12.12.3.5.4b, AASHTO LRFD 2004 [7]) such as strain limits and reversal of curvature of the pipe. Hence, overestimated deflections from the Spangler and McGrath equations may lead to overly conservative designs.

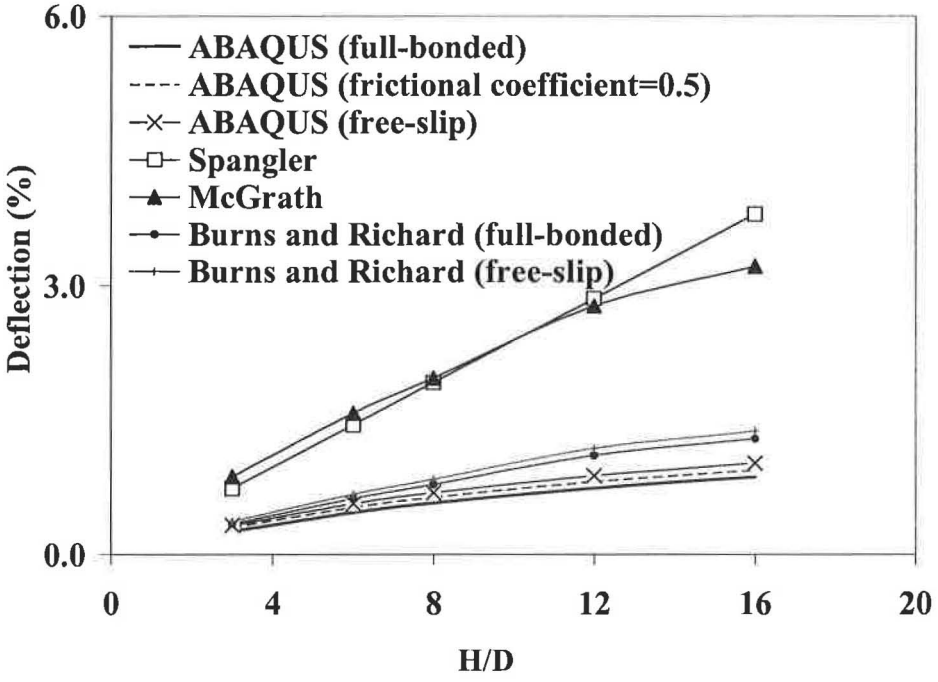

Figure 5.4: Vertical deflection (parameters: deflection lag factor (D_L) = 1; bedding factor (K_B) = 0.1)

5.2 Buckling Analyses

The pipe-spring model shown in Figure 5.5 was developed by placing linear springs below the springline of the CSP to investigate its buckling strength. The spring constants used in the above pipe-spring model were determined by a trial and error process from a series of soil-structure analyses. Equilibrium was checked at each loading. Each trial loading consists of variable shearing forces on the entire surface of the pipe such that they maintain symmetry with respect to the vertical axis. Each trial loading also includes vertical load representing the burial depth at each node above the springline. Additional lateral springs were needed above the springline to correctly model the soil-structure interaction. These additional lateral springs were needed to match the bending moment in the region between the crown and the springline to the bending moment developed in the soil-pipe system.

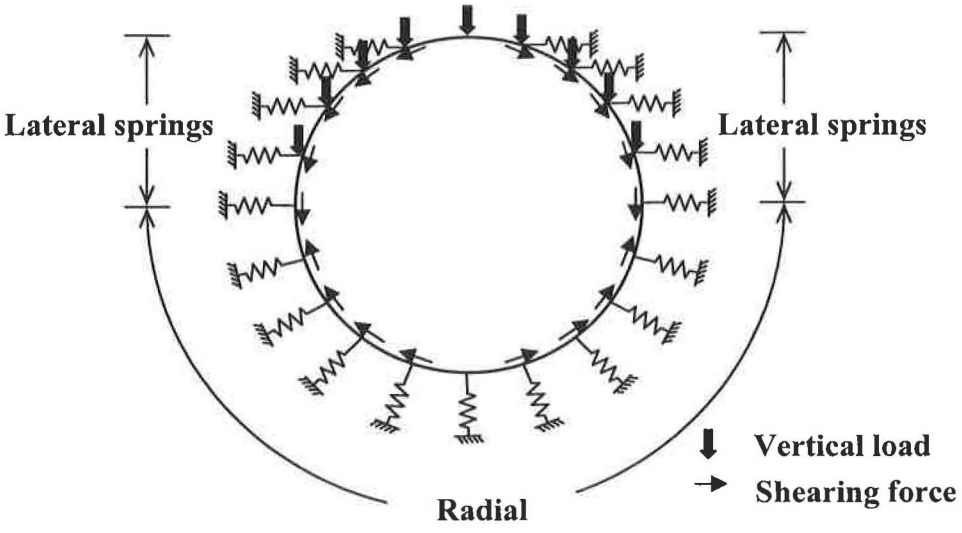

Figure 5.5: Pipe-spring model

The bending moment in the region between the invert and the springline is properly accounted for by the presence of the radial springs shown in Figure 5.5.

Based on a series of some 100 hypothetical models, Equations 5.1 and 5.2 were extracted by multiple linear regression processes. Figure 5.6 shows, comparatively, the critical buckling stresses determined from AASHTO LRFD [7], AISI [6], and the pipe-spring model developed herein. The critical buckling stresses determined from the pipe-spring model are in reasonably good agreement with those from AISI. AASHTO LRFD [7] yields values considerably greater than the pipe-spring model. Figure 5.6 clearly shows that the buckling strength determined from AASHTO LRFD [7] is considerably greater than those from the pipe-spring model. Although the buckling strength determined from the pipe-spring model is fairly close to those obtained from AISI [6], the buckling strength from the pipe-spring model is 7.3% smaller than that from AISI at the upper limit of the industry imposed slenderness ratio, thereby indicating the unconservative nature of the buckling strength by existing procedures. It is believed that this successful innovative analytical method to determine the critical buckling load for deeply CSP duly reflecting the soil-structure interaction is first of its kind. Despite the unconservative nature of the existing buckling strength formula, there has been little expressed concern. This is perhaps due to the fact that the industry self-imposed limit [8] for the pipe slenderness ratio of 294 is smaller than the threshold value for yielding from the AISI formula [6].

$$f_{cr} = f_y = 227{,}370\,\text{kPa}\ (33{,}000\,\text{psi}) \qquad \text{when } \frac{D}{r} \le 343 \qquad (5.1a)$$

$$f_{cr} = \alpha \frac{E_p}{(D/r)^2} \qquad \text{when } \frac{D}{r} > 343 \qquad (5.1b)$$

$$\alpha = 0.27(D/r) + 14.94 \qquad \text{for SW85} \qquad (5.2a)$$

$$\alpha = 0.30(D/r) + 34.23 \qquad \text{for SW90} \qquad (5.2b)$$

$$\alpha = 0.20(D/r) + 114.08 \qquad \text{for SW95} \qquad (5.2c)$$

where α = dimensionless coefficient.

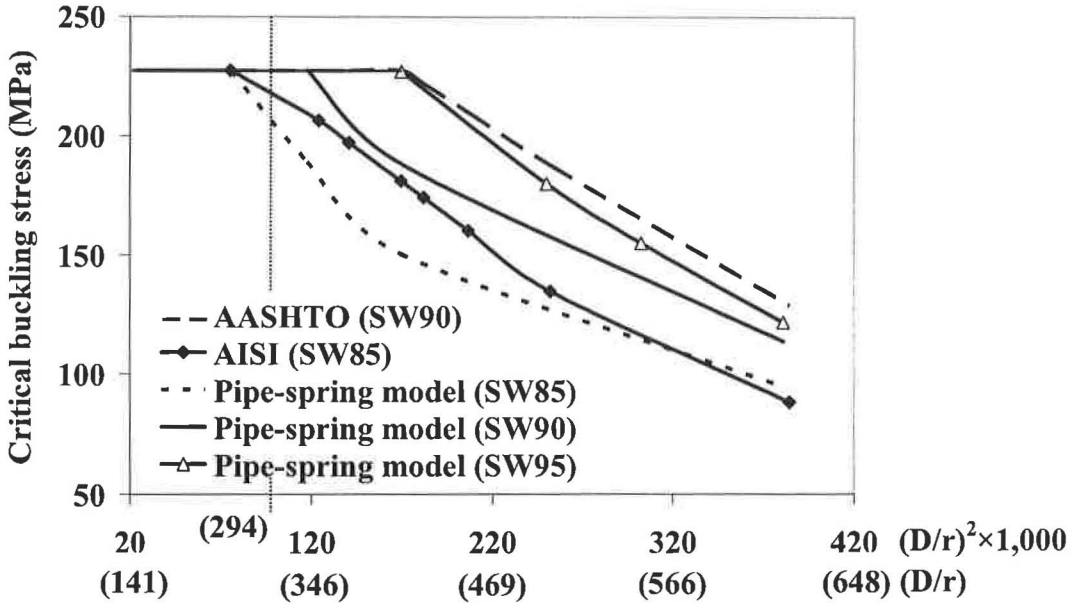

Figure 5.6: Comparison of critical buckling stresses between AASHTO, AISI, and pipe-spring model (D = pipe diameter; r = radius of gyration of corrugation)

5.3 Imperfect Trench Installation

5.3.1 Optimization of Soft Zone Geometry

As mentioned earlier, the soft zone geometry is traditionally defined by three parameters; width, W; height, H_s; and the distance from the top of the pipe to the bottom of the soft zone, H', as shown in Figure 5.7(a). Figure 5.7(c) shows the soft zone geometry suggested by Spangler [23] and Vaslestad et al. [30] where H'=0. Based on a large number of parametric studies (over 300 cases), the proposed soft zone geometry shown in Figure 5.7(b), is shown to be

most effective in reducing earth pressure. The soft zone at the sidewall is different than that shown in Figure 4.3(b) for PVC pipe. The sidewall thickness for CSP is fixed at 76 mm (3 inches).

Unlike the case of corrugated PVC pipes where the slenderness ratio, D/r, varies in a narrow range, 60 - 100, the slenderness ratio of CSP varies in a wide range, 154-411. Therefore, it was necessary to include the slenderness ratio as a variable in the process for optimizing soft zone geometry. As shown in Figure 5.8(a), the reduction rate (R_{ms}) remains virtually unchanged once the height of the soft zone (H_s) divided by the pipe diameter (D) of the pipe reaches 0.25.

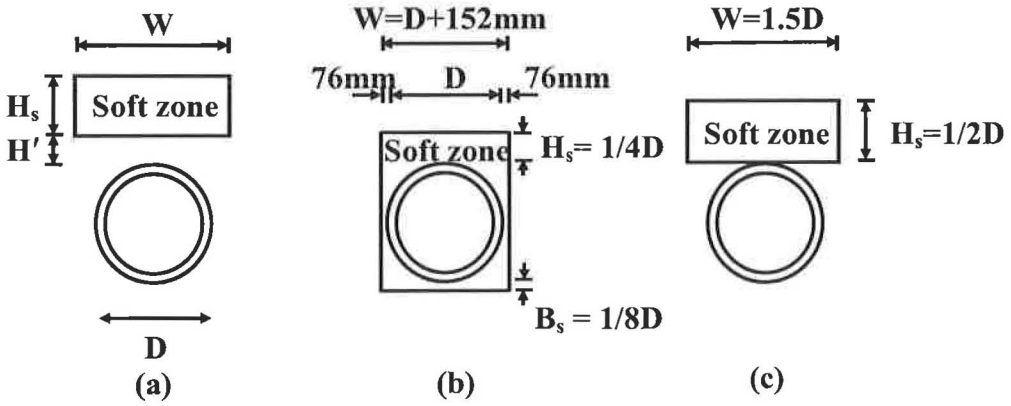

Figure 5.7: Notation for imperfect trench installations and geometries of soft zone: (a) notation, (b) soft zone geometry (proposed), and (c) soft zone geometry (conventional)

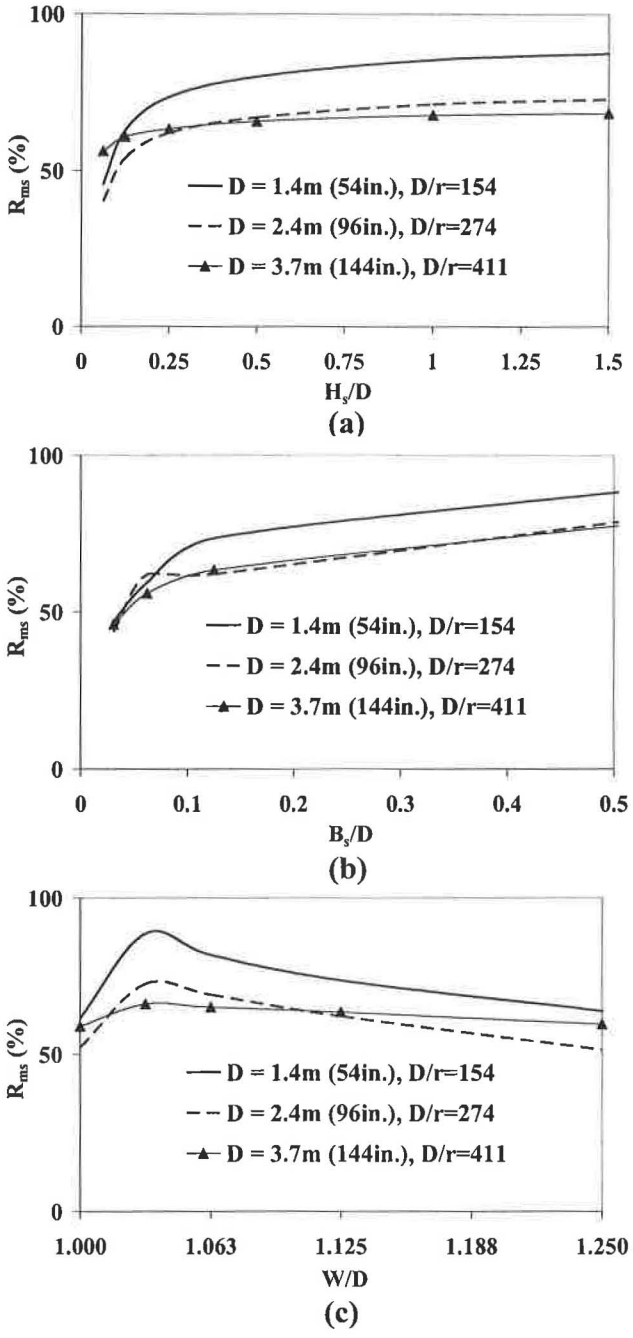

Figure 5.8: Optimization process of soft zone geometry: (a) Height of soft zone (H_s) with W= D +152mm and B_s/D= 0.125, (b) Thickness of soft zone below invert (B_s) with H_s/D= 0.25 and W= D +152mm, and (c) Width of soft zone (W) with H_s/D= 0.25 and B_s/D= 0.125 (R_{ms} = reduction rate of maximum wall stress; modulus of elasticity of the lightweight material = 345 kPa)

A bedding thickness for the soft material zone below invert, B_s, of 1/8 times the pipe diameter was selected. The reduction rates (R_{ms}), shown in Figure 5.8(b), do not improve much for thickness greater than this value. Figure 5.8(c) gives the variation of the reduction rate as a function of the width of the soft zone, W. As shown in Figure 5.8(c), the maximum reduction rate occurs when the width of the soft zone is about the pipe diameter plus 1/32 times the pipe diameter. The reduction rate actually decreases as the width of the soft material zone is increased beyond this optimum width. This is caused by the loss of lateral support due to the presence of wider soft sidefill that increases the bending moment at the springline (induced as a result of wider lateral deformation of the pipe). In order to facilitate the installation (constructibility) of the soft zone (preferably 76 mm on each side as a minimum), a width of the pipe diameter plus 152 mm (6 in.) is recommended.

5.3.2 Imperfect Trench Installation versus Embankment Installation

As shown in Figure 5.7(c), higher-than-expected lateral pressure develops when the soft zone is placed only at the top of the pipe. This is due to a redistribution of the load from the crown to the sides of the pipe and the development of undesirable shear stresses . This is confirmed in Figure 5.9(a) which shows radially pressure increasing as the angle from the crown increases. Figure 5.9(b) shows that a soft zone results in significantly different patterns of shear stresses, compared to the embankment installation.

In the case of embankment installations, a positive shearing force (in the clockwise tangential direction) develops above the springline while a negative shearing force (in the counter- clockwise tangential direction) develops below the springline. As these two shearing

forces of opposite direction are nearly equal in magnitude, there is no significant axial force increase at the springline and the bottom of the pipe, as shown in Figure 5.9(b).

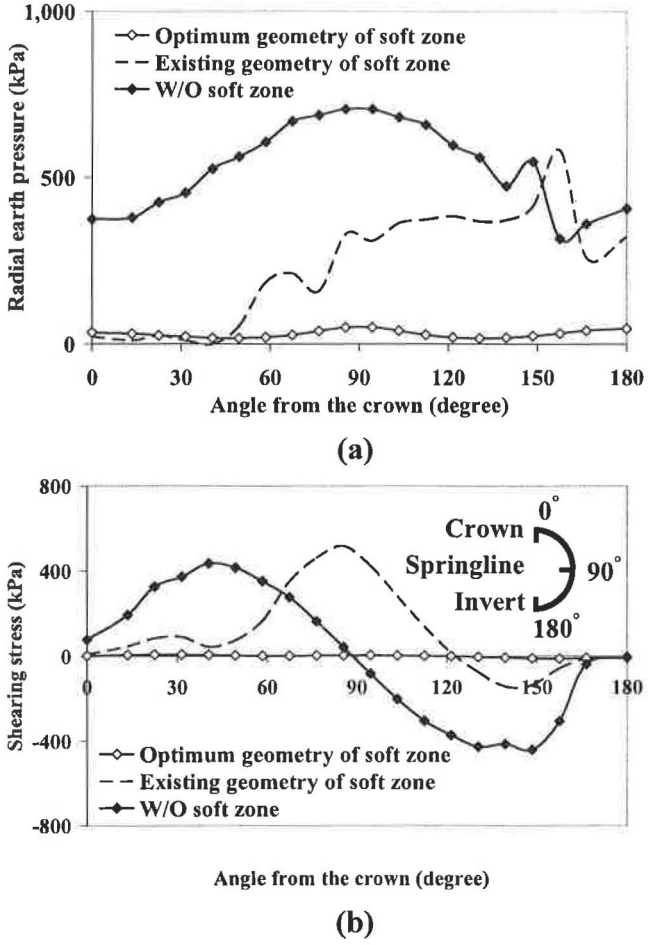

Figure 5.9: Imperfect trench installations versus embankment installation: (a) radial earth pressure, and (b) shearing stress (parameters: pipe diameter = 2.4 m; fill height = 29 m; modulus of elasticity of the lightweight material = 345 kPa)

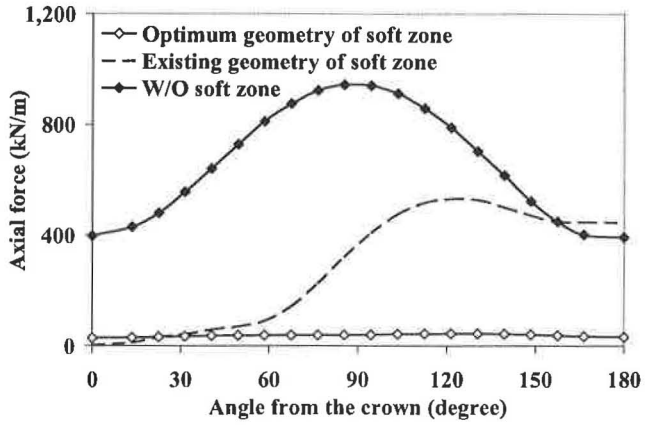

(c)

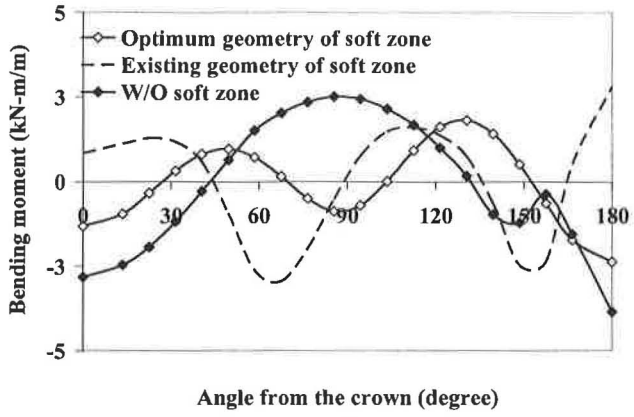

(d)

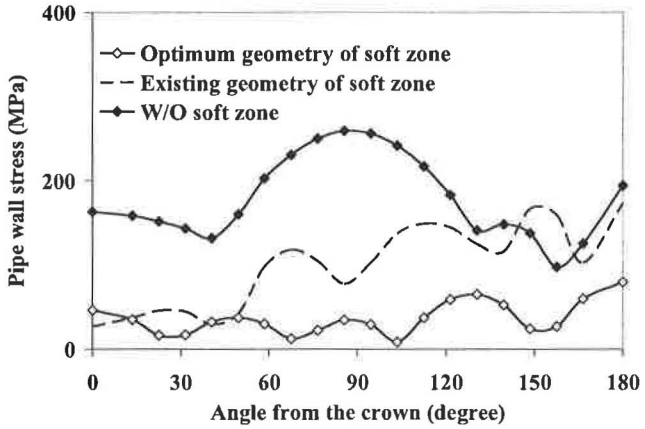

(e)

Figure 5.9: Imperfect trench installations versus embankment installation: (c) axial force , (d) bending moment, and (e) pipe wall stress (parameters: pipe diameter = 2.4 m; fill height = 29 m; modulus of elasticity of the lightweight material = 345 kPa)

For the soft zone geometry as shown in Figure 5.7(c), the radial pressure at about 155 degrees from the crown becomes significantly larger than that at the crown, as shown in Figure 5.9(a). It is noted herein that the development of shearing forces affect the radial forces in the pipe indirectly due to the relationship of the pressure versus hoop tension. This undesirable shearing stress distribution was practically eliminated by extending the soft zone to the bedding as shown in Figure 5.7(b). The resulting shearing stresses are dramatically decreased as shown in Figure 5.9(b). This, in turn, significantly decreases the radial earth pressure on the pipe as shown in Figure 5.9(a). With this effective elimination of the undesirable development of the shearing forces comparatively shown in Figure 5.3 and Figure 5.10, the pipe wall stress that is used as the main design criterion is reduced significantly as shown in Figure 5.9(e).

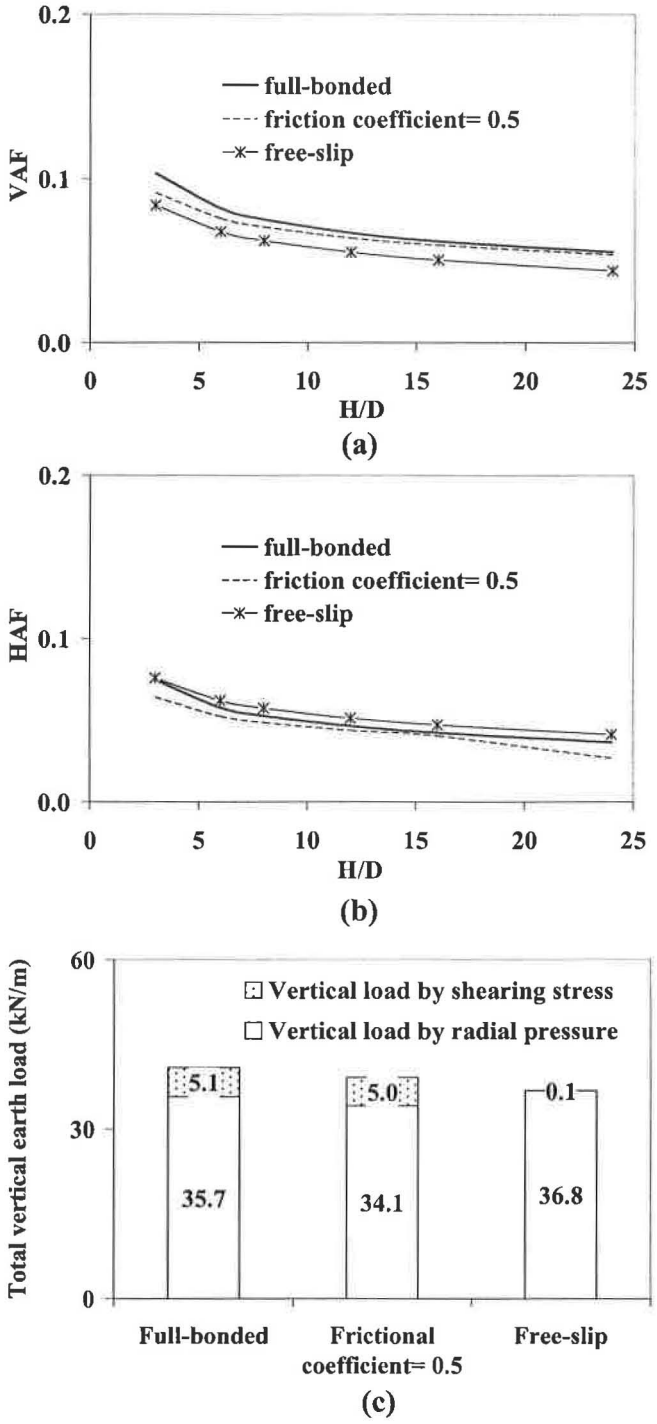

Figure 5.10: Effects of interface properties in ITI: (a) *VAF* versus *H/D*, (b) *HAF* versus *H/D*, and (c) total vertical earth load (W_e) versus interface properties for pipe diameter = 2.4 m and fill height = 29 m (parameters: modulus of elasticity of the lightweight material = 345 kPa; proposed soft zone geometry as shown in Figure 5.7(b))

5.4 Predictor Equations

5.4.1 Arching Factor, Deflection, and Maximum Wall Stress

More than 300 hypothetical models were run in order to generate data to develop equations for arching factors, deflections, and maximum wall stresses. The full-bonded interface condition was assumed conservatively and linear regression techniques were used to develop equations. Values of *D/r* were varied between 154 and 411. Figure 5.11 show that arching factors for CSP are hardly affected by *H/D* or *D/r*. Therefore, *VAF* and *HAF* of 1.4 and 0.6, respectively, are recommended for SW90 backfill. These are significantly higher than values determined from AASHTO LRFD [7] and AISI [6] procedures.

Pipe deflections, as shown in Figure 5.11(c), are affected by *H/D* and *D/r* and the equation

$$\frac{\Delta_y}{D}(\%) = \left(0.087\frac{H}{D} + 0.167\right)\left(\frac{D}{274r}\right) \tag{5.3}$$

was developed for computing the ratio of vertical deflection to pipe diameter. Figure 5.11(d) introduces a parameter, F_{ms}, to be incorporated into a procedure to determine the wall stress as the main design criterion. As can be seen from Figure 5.11(d), the parameter is not affected very much by *H/D* and *D/r*. A value of 575 for F_{ms} appears to be reasonably

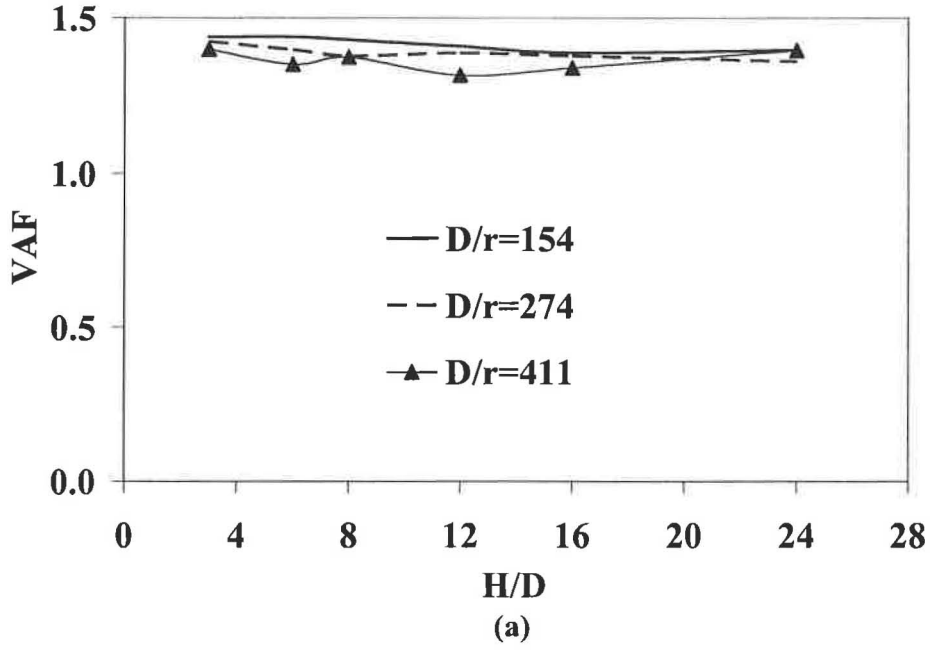

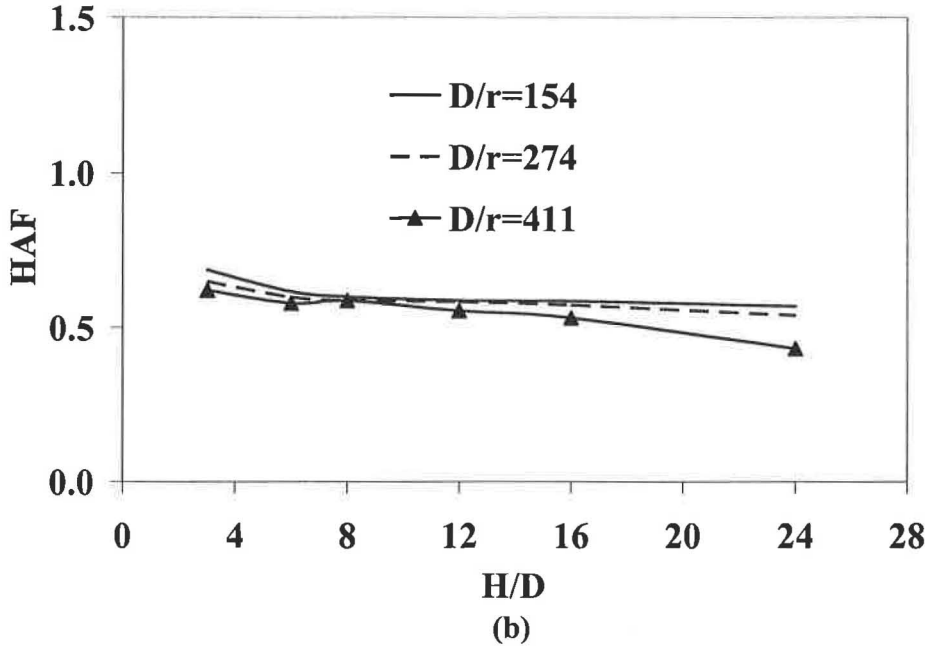

Figure 5.11: Arching factor, deflection, and soil-structure interaction multiplier (F_{ms}) for maximum wall stress versus *H/D*: (a) *VAF* and (b) *HAF* (*D* = pipe diameter; *r* = radius of gyration of corrugation; interface condition= full-bonded) (continued)

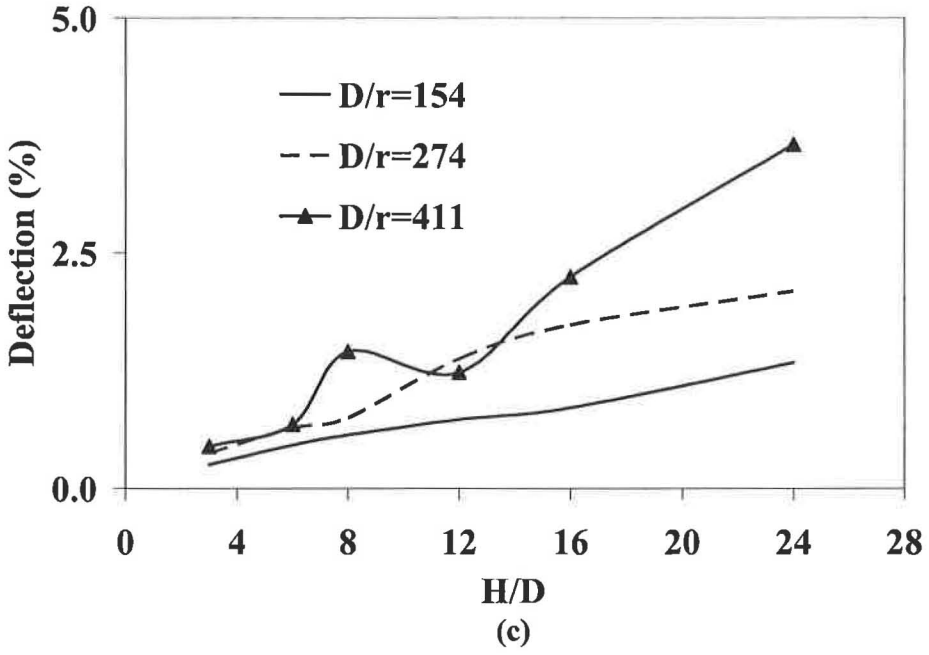

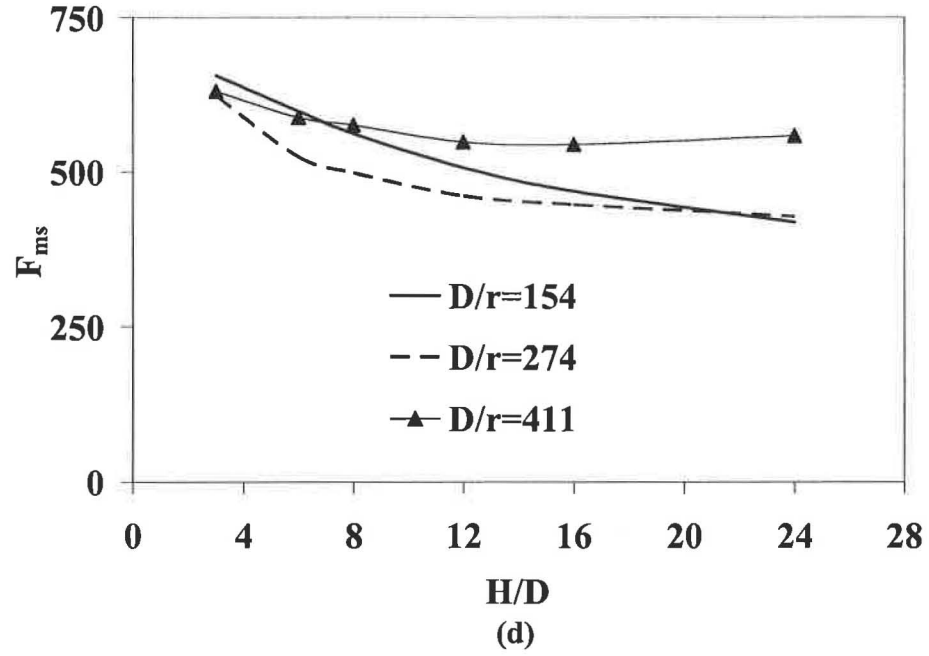

Figure 5.11: Arching factor, deflection, and soil-structure interaction multiplier (F_{ms}) for maximum wall stress versus *H/D*: (c) deflection and (d) soil-structure interaction multiplier (F_{ms}) (D = pipe diameter; r = radius of gyration of corrugation; interface condition= full-bonded)

conservative value for a range of *H/D* and *D/r*. Maximum wall stresses (σ_{max}), therefore, can be calculated as follows:

$$\sigma_{max} = F_{ms}\left(\frac{PL}{D}\right) = 575\left(\frac{PL}{D}\right) \tag{5.4}$$

5.4.2 Reduction Rates

The geometry of the soft zone, H/D, D/r, and the modulus of elasticity and Poisson's ratio of the soft zone material are variables affecting the reduction rates for the arching factors, deflection, and maximum wall stress in ITI. After the three dominant geometric parameters of the soft zone (height, bedding thickness, width) were identified as shown in Figure 5.8, the remaining variables were varied in the production run of nearly 300 hypothetical models. An examination of the analysis results revealed that H/D and Poisson's ratio of the soft zone material do not affect very much the reduction rates. Therefore, these two variables were not considered further in the development of predictor equations. As shown in Figure 5.12, D/r has some effect on the reduction rates for horizontal arching factor, deflections and maximum wall stress. Figure 5.12 shows that reduction rates are affected by the modulus of elasticity of soft zone material and that the reduction rates decrease as the modulus of elasticity of the lightweight material increases. As mentioned in Chapter 4, this demonstrates that the soft zone material should be as soft (low modulus of elasticity) as practically possible.

Reduction rates for CSP in ITI are computed with

$$R_v = \left(-0.010E_s + 97.08\right) \tag{5.5}$$

$$R_h = \left(-0.015E_s + 95.34\right) \qquad \text{for } D/r \text{ £ } 274 \tag{5.6}$$

$$R_h = (-0.015E_s + 95.34) + \left(\frac{D/r}{274}\right)^{\beta_1} \quad \text{for } D/r > 274 \tag{5.7}$$

$$\beta_1 = E_s^{0.26} \tag{5.8}$$

$$R_d = \left(7\times10^{-6}E_s^{\,2} - 0.047E_s + 81.79\right) \quad \text{for } D/r \leq 274 \tag{5.9}$$

$$R_d = \left(7\times10^{-6}E_s^{\,2} - 0.047E_s + 81.79\right) - \left(\frac{D/r}{274}\right)^{\beta_2} \quad \text{for } D/r > 274 \tag{5.10}$$

$$\beta_2 = E_s^{0.30} \tag{5.11}$$

$$R_{ms} = \left(7\times10^{-6}E_s^{\,2} - 0.045E_s + 86.48\right)\left(\frac{274}{D/r}\right)^{0.3} \tag{5.12}$$

where b_1, b_2 = nondimensional parameters. It is noted that conversion factor must be incorporated in the above equations when the unit of E_s is different from kPa.

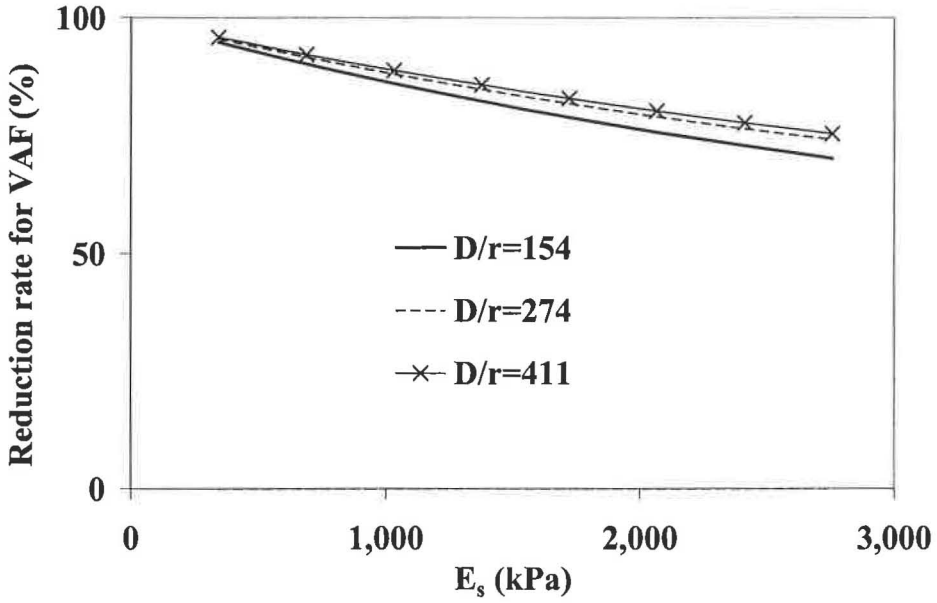

(a)

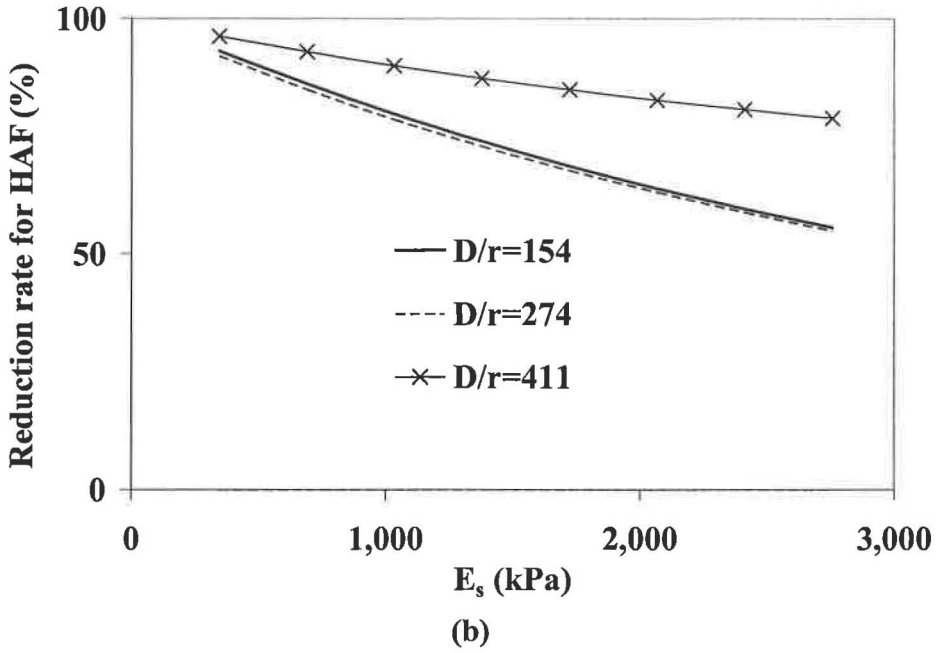

(b)

Figure 5.12: Reduction rates versus modulus of elasticity of lightweight material (E_s): (a) *VAF* and (b) *HAF* (parameter: proposed soft zone geometry as shown in Figure 5.7(b)) (continued)

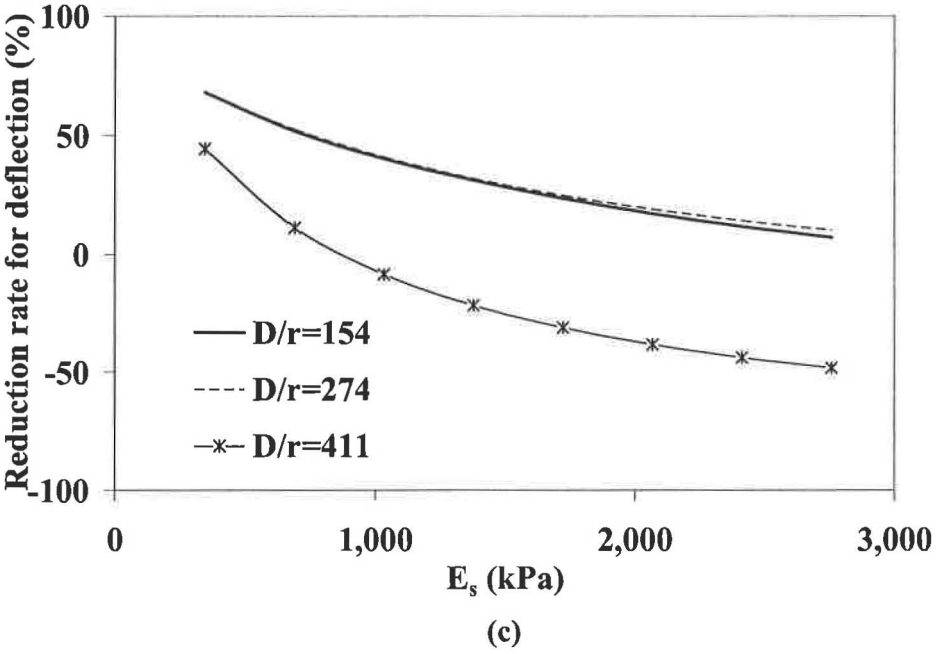

(c)

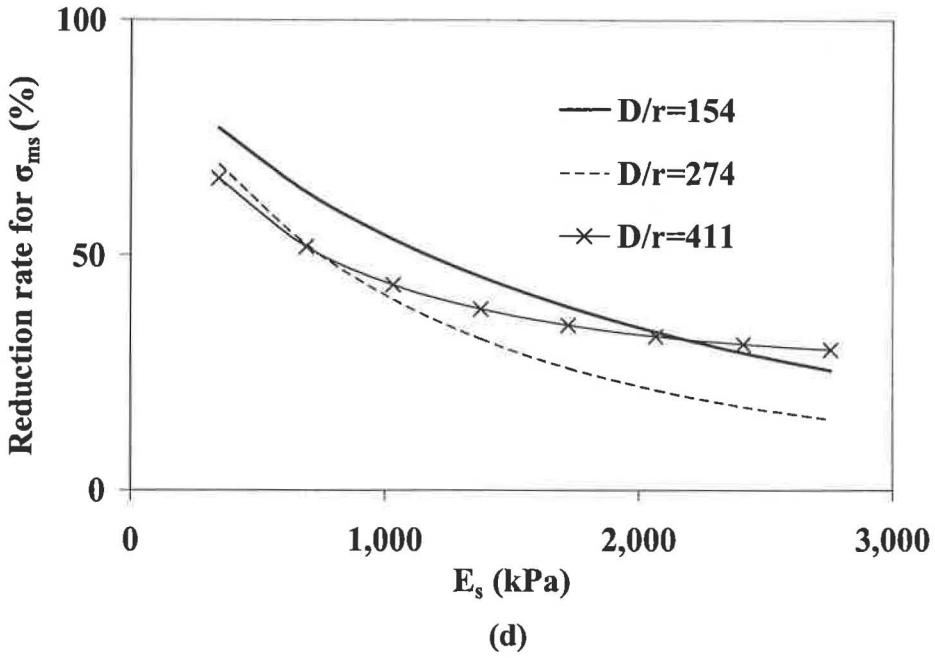

Figure 5.12: Reduction rates versus modulus of elasticity of lightweight material (E_s): (c) Deflection and (d) Maximum wall stress (σ_{ms}) (parameter: proposed soft zone geometry as shown in Figure 5.7(b))

CHAPTER 6

SUMMARY AND CONCLUSIONS

6.1 Summary and Conclusions

The single most important accomplishment of the study is the optimization soft zone geometry for ITI of flexible pipes. Although Brown [57] first introduced the possibility of numerically assessing the effectiveness of ITI and Kim and Yoo [54] extended this concept considerably, no one considered the fairly high intensity shearing forces on the sides of flexible pipes in ITI. These undesirable shearing forces can be reduced by extending the soft zone material all the way to the bottom of the pipe. As a consequence, earth load can be reduced by up t0 85%. Corrugated PVC and steel pipes were studied but the optimum soft zone geometry can be applied to any deeply buried conduits with minor adjustments related to the thickness of the soft zone at the sidewall.

Corrugated PVC Pipes

1) The interface effect on *VAF* in flexible pipe is not negligible as it is for rigid pipe. However, the degree of the interface effect cannot be determined by analysis alone although the analysis procedure used in this study demonstrates that any interface effect including in-between condition can be reflected. A well designed field testing program is needed to assess this question. However, the conservative approach of full bond interface is an intermediate option and was the approach taken in this study.

2) The deflections from ABAQUS were much less than those computed from Spangler equation [2] while they were relatively close to those from the Burns and Richard [16] deflection equations. The results from the ABAQUS and Burns and Richard deflection equations, also, showed that the interface conditions have insignificant effects on the deflections of corrugated PVC pipes. This observation appears valid as the primary parameter affecting the deflection of flexible PVC pipes is the earth load at the crown which does not vary much depending upon the interface conditions.
3) The reduction rate of the arching factors related to axial force alone reaches up to 92% while the reduction rate of maximum wall stresses related to the combined action of bending moment and axial force is 85% as the reduction rate related to bending moment is only 18%. This is due to the fact that the maximum bending moment at the springline is not reduced significantly because of the horizontal movement of the flexible pipe aided by the presence of soft zone that was needed to minimize the shearing forces.

Corrugated Steel Pipes

1) The arching factors for buried CSP are not affected very much by the pipe slenderness ratio, *D/r*, and the ratio of fill height-to-diameter, *H/D*. Therefore, the current practice of specifying constant values of for *VAF* and *HAF* by AASHTO LRFD and AISI is justified. However, their *VAFs* (AASHTO LRFD=1.1, AISI=0.75) appear to be quite unconservative. Further, they do not specify *HAFs* at all. It has been found that *VAFs* and *HAFs* need to be 1.4 and 0.6, respectively, for SW90.
2) The constant arching factors and the simplified predictor equations for the deflections at the crown and the maximum wall stresses given by Equations 5.3 and 5.4 do not require the

value of the constrained soil modulus (M_S) as in other existing predictor equations by Burns and Richard [16] and/or AASHTO LRFD [7].

3) The interface effect on *VAF* of CSP in embankment installation is not negligible as in the case for rigid pipe.
4) The elastic buckling strengths of the buried CSP were carried out on the pipe-spring model. The elastic buckling strengths from the pipe-spring model are in good agreement with those computed from the AISI procedure. AASHTO LRFD [7] gave critical stresses greater than those by the pipe-spring model.

An innovative understanding of the soil-structure interaction for deeply buried conduits and other findings presented in this study ought to be able to find their way into improved specifications in the near future. As the economic impact appears to be huge, an immediate implementation of these findings by designers and contractors will render a high dividend for conduits buried under several hundred feet of fill.

6.2 Recommendation for Future Study

Field experimental studies of deeply buried conduits would be desirable in order to calibrate the results of FEA and verify the validity and reasonableness of the assumptions in the physical behavior of the soil-structure interaction and material properties and characterization adopted in this study. In light of the importance of the interface condition between the exterior wall of the conduits and the backfill soil on the behavior of the soil-structure interaction, particularly in ITI, a detailed experimental study on this topic is urgently needed. Information on the properties and behavior of the soft materials, particularly the long-term effect and potential environmental degradation, envisioned for ITI would be a welcome addition.

This page intentionally left blank

REFERENCES

[1] Civil Connection. (2006). FHWA Broadens Allowable Pipe Choices. On-line version at http//www.news.cenews.com, December 26, 2006.

[2] Spangler, M. G. (1941). The Structural Design of Flexible Culverts. Iowa State College Bulletin 30, Vol. XI.

[3] Watkins, R. K. (1990). Plastic Pipes Under High Landfills. Buried Plastic Pipe Technology, ASTM STP 1093, pp. 379-392.

[4] Watkins, R. K., and Anderson, L. R. (2000). Structural Mechanics of Buried Pipes, CRC Press LLC, Boca Raton, FL.

[5] Moore I. D. (2000). Buried pipes and culverts. Geotechnical and Geoenvironmental Engineering Handbook, 18: 541-567.

[6] AISI (1994). Handbook of Steel Drainage & Highway Construction Products, 5th. American Iron and Steel Institute, Washington, DC.

[7] AASHTO (2004a). AASHTO LRFD bridge design specifications, 3rd ed., American Association of State Highway and Transportation Officials, Washington, DC.

[8] Brockenbrough, R.L. (2006). A personal correspondence (e-mail, June 29, 2006) to Yoo, C.H., Department of Civil Engineering, Auburn University, Auburn, AL.

[9] McAffee, R. P., and A. J. Valsangkar. (2005). Performance of an Induced Trench Installation. In Transportation Research Record: Journal of the Transportation Research Board, No. 1936, TRB, National Research Council, Washington, DC, pp. 230-237.

[10] ABAQUS User's manual. (2003). Habbitt, Karlsson and Sorensen, Inc., Pawtucket, RI.

[11] MSC/NASTRAN 2005 Release Guide. (2005). The MacNeal-Schwendler Corp., Los

Angeles, CA.

[12] Musser, S.C. (1989). "CANDE-89 User Manual." FHWA-RD-89-169. Federal Highway Administration, U.S. Department of Transportation.

[13] Katona MG, Smith JM, Odello RS, Allgood JR. (1976). CANDE-a modern approach for the structural design and analysis of buried culverts. Report FHWA-RD-77-5, FHWA, U.S. Department of Transportation.

[14] Heger, F.J., Liepins, A.A., and Selig, E.T. (1985). "SPIDA: An Analysis and Design System for Buried Concrete Pipe." Advances in Underground Pipeline Engineering – Proceeding of the International Conference, ASCE, 143-154.

[15] ACPA (1994). ACPA Concrete Pipe Technology Handbook. Second Printing, American Concrete Pipe Association, Vienna, VA.

[16] Burns, J. Q., and R. M. Richard. (1964). Attenuation of Stresses for Buried Cylinders. In Proc., Symposium on Soil-Structure Interaction, University of Arizona Engineering Research Laboratory, Tucson.

[17] McGrath, T. J. (1998). Design Method for Flexible Pipe. A Report to the AASHTO Flexible Culvert Liaison Committee, Simpson Gumpertz & Heger Inc.

[18] McGrath, T. J. (1999). Calculating Loads on Buried Culverts Based on Pipe Hoop Stiffness. In Transportation Research Record: Journal of the Transportation Research Board, No. 1656, TRB, National Research Council, Washington, DC, pp. 73-79.

[19] Sargand, S. M., and T. Masada. (2003). Soil Arching over Deeply Buried Thermoplastic Pipe. In Transportation Research Record: Journal of the Transportation Research Board,No. 1849, TRB, National Research Council, Washington, DC, pp. 109-123.

[20] Watkins, R. K., and M. G. Spangler. (1958). Some Characteristics of the Modulus of

Passive Resistance of Soil: A Study in Similitude. Presented at the 37th Annual Meeting of Highway Research Board, Washington DC.

[21] Watkins RK, Moser RP. (1969). The structural performance of buried corrugated steel pipes. Utah State University, Logan, Utah and American Iron and Steel Institute, Washington, DC.

[22] ACPA (1988). Concrete Pipe Handbook, Third Printing, American Concrete Pipe Association, Irving, TX.

[23] Spangler, M.G. (1950a). "A Theory of Loads on Negative Projecting Conduits." Proceedings of the Highway Research Board, 30, Transportation Research Board, Washington, DC, 153-161.

[24] Marston, A., and Anderson, A. O. (1913). "The theory of loads on pipes in ditches and tests of cement and clay drain tile and sewer pipes." Bulletin 31, Iowa Engineering Experiment Station, Ames, IA.

[25] Marston, A. (1922). "Second Progress Report to the Joint Concrete Culvert Pipe Committee." Iowa Engineering Experimental Station, Ames, IA.

[26] Marston A. (1930). The theory of external loads on closed conduits in the light of the latest experiments. Bulletin 96. Iowa Engineering Experiment Station, Ames, Iowa.

[27] Spangler, M. G., and Handy, R.L. (1982). Soil Engineering, 4th Ed., Harper and Row, NY.

[28] Sladen J.A. and Oswell J.M. (1988). "The Induced Trench Method – A Critical Review and Case History." Can. Geotech. J., 25, 541-549.

[29] Sven, N., and Liedberg, D. (1997). "Load Reduction on A Rigid Pipe Pilot Study of A Soft Cushion." Transportation Research Record, 1594, 217-223.

[30] Vaslestad, J., Johansen, T.H., and Holm, W. (1993). "Load reduction on rigid culverts beneath high fills: long term behavior." Transportation Research Record, 1415, Transportation Research Board, Washington, DC, 58-68.

[31] Tyler, M. (2003). "Earth Pressures on Induced Trench Conduits." M.S Thesis, Dept of Civil Engineering, University of New Brunswick, Canada.

[32] Janbu, N. (1957). Earth pressure and bearing capacity calculations by generalized procedure of slices, Proc.4.Int.Conf.SMFE, London, Vol. 2, 207-212.

[33] Spangler, M.G. (1933). "The supporting Strength of Rigid Pipe Culverts." Bulletin 112, Iowa State College, IA.

[34] Yoo, C.H., Parker, F., and Kang, J. (2005). "Bedding and Fill Heights for Concrete Roadway Pipe and Box Culverts." Final Report, ALDOT Project No. 930-592, Highway Research Center, Auburn University, AL.

[35] Kim, K., and Yoo, C.H. (2005). "Design Loading for Deeply Buried Box Culverts." J. Geotech. Geoenviron. Eng., ASCE, 131(1), 20-27.

[36] McVay, M.C., and Selig, E.T. (1981). Soil Model and Finite Element Boundary Studies, Report No. ACP81-283I, Dept. of Civil Engineering, University of Massachusetts, Amherst, Mass.

[37] McVay, M. C. (1982). Evaluation of Numerical Modeling of Buried Conduits, Ph.D. Dissertation, Dept of Civil Engineering, University of Massachusetts, Amherst, Massachusetts.

[38] ACPA (1989). SPIDA users instructions micro computer version 3c. American Concrete Pipe Association, Vienna, VA.

[39] AASHTO (2004b). LRFD Bridge Construction Specifications, 2nd ed. American

Association of State Highway and Transportation Officials, Washington, DC.

[40] McGrath, T.J., Selig, E.T. (1999). "Pipe Interaction with the Backfill Envelope." Report FHWA-RD-98-191, Federal Highway Administration, U.S. Department of Transportation.

[41] Kondner, R.L. (1963). "Hyperbolic Stress-Strain Response: Cohesive Soils." J. Soil Mech. Found. Div., ASCE, 98(1), 115-143.

[42] Christian, J.T. (1982). "The Application of Generalized Stress-Strain Relations." Proceeding of the Symposium on Limit Equilibrium, Plasticity and Generalized Stress-Strain Applications in Geotech. Eng., ASCE Annual Convention and Exposition Hollywood, FL.

[43] Janbu, N. (1963). Soil Compressibility as Determined by Oedometer and Triaxial Tests, European Conference on Soil Mechanics & Foundations Engineering, Wiesbaden, Germany Vol. 1, pp. 19-25.

[44] Duncan, J.M., and Chang, C.Y. (1970). "Nonlinear Analysis of Stress and Strain on Soils." J. Soil Mech. and Found. Div., ASCE, 96(5), 1629-1653.

[45] Wong, K.S., and Duncan, J.M. (1974). Hyperbolic Stress-Strain Parameters for Nonlinear Finite Element Analysis of Stresses and Movements in Soil Masses, Report No. TE-74-3, University of California, Berkeley, CA.

[46] Duncan, J.M., Byne, P., Wong, K.S., and Mabry, P. (1980). "Strength, Stress-Strain and Bulk Modulus Parameters for Finite Element Analyses of Stresses and Movement in Soil Masses." UCB/Gt/80-01, Univ. of California, Berkeley, CA.

[47] Selig, E.T. (1988). "Soil Parameters for Design of Buried Pipelines." In Pipeline Infrastructure: Proc., Pipeline Infrastructure Conference, ASCE, NY.

[48] Lin, R-S.D. (1987). "Direct Determination of Bulk Modulus of Partially Saturated Soils", Project Report ACP87-341P, M.S. Degree, University of Massachusetts, Amherst, MA.

[49] McAffee, R.P., and Valsangkar, A.J. (2004). "Geotechnical Properties of Compressible Materials Used for Induced Trench Construction." J. Testing and Evaluation, 32(2), 143-152.

[50] Sargand, S. M., T. Masada, and D. J. Schehl. (2001a). Soil Pressure Measured at Various Fill Heights Above Deeply Buried Thermoplastic Pipe. In Transportation Research Record: Journal of the Transportation Research Board, No. 1770, TRB, National Research Council, Washington, DC, pp. 227-235.

[51] Sargand, S. M., G. A. Hazen, K. White, and A. Moran. (2001b). Time-Dependent Deflection of Thermoplastic Pipes Under Deep Burial. In Transportation Research Record:Journal of the Transportation Research Board, No. 1770, TRB, National Research Council, Washington, DC, pp. 236-242.

[52] Sargand, S.M., and Moreland, A. Experimental and Numerical Investigation of A Deeply Buried Corrugated Steel Multi-Plate Pipe. Final Technical Report. Ohio Department of Transportation; FHWA, U.S. Department of Transportation; 2004.

[53] Katona, M.G., Akl, A.Y. (1987). Design of buried culverts with stress-relieving joints. Transportation Research Record; 1129: 39-54.

[54] Kim, K., and Yoo, C.H. (2002). Design Loading for Deeply Buried Box Culverts, Highway Research Center, Auburn University, AL.

[55] Sargand SM, Hazen GA, Masada T. (2002). Field Verification of Structural Performance of Thermoplastic pipe Under Deep Backfill Conditions. Draft Final

Report Ohio Department of Transportation; FHWA, U.S. Department of Transportation.

[56] AASHTO (2002). AASHTO standard specifications for transportation materials and methods of sampling and testing, 22nd. American Association of State Highway and Transportation Officials, Washington, DC.

[57] Brown, C.B. (1967). "Forces on rigid culverts under high fills." J. Struct. Div., ASCE, 93(5), 195-215.

[58] ACPA (1996). Standard Installations and Bedding Factors for the Indirect Design Method. Design Data 40, American Concrete Pipe Association, Vienna, VA.

[59] Spangler, M. G. (1950b). Field Measurements of the Settlement Ratios of Various Highway Culverts, Bulletin 171, Iowa Engineering Experiment Station, Ames, IA.

This page intentionally left blank

APPENDIX

APPENDIX 1

MARSTON AND SPANGLER' S THEORY

The Marston theory of loads on buried conduits was developed near the beginning of the twentieth century. M.G. Spangler presented three bedding configurations and used the concept of a bedding factor to relate the supporting strength of buried pipe to the strength obtained in a three-edge bearing test [58]. Spangler's theory proposed that the bedding factor for a particular pipeline and, consequently, the supporting strength of the buried pipe, is dependent on two installation characteristics: the width and quality of the contact between the pipe and bedding and the magnitude of the lateral pressure and the portion of the vertical height of the pipe over which it acts.

The soil around the conduit was initially divided into prisms by imaginary vertical lines that extend from either side of the conduit to the top of the embankment. The load equations were derived based on an analysis of the forces acting on a thin slice of soil located within the interior prism.

Earth loads on the buried conduits were predicted by applying a factor to the weight of soil overlaying the pipe. The load factor was calculated based on frictional forces that were assumed to develop along these vertical planes. The frictional forces were considered to be generated by differential settlements between the prism of soil directly above the pipe and those on either side. The direction of these shear forces could increase or decrease the load on the pipe depending upon the direction of the differential settlement between the two prisms, as shown in Figure 1.1. Greater settlement above the conduit resulted in earth pressures that were less than

the overburden. Earth pressures greater than the overburden pressure occurred when greater settlements occurred in the exterior prisms.

Marston [26] and Spangler [59] quantified the load on conduits installed by different construction conditions by solving differential equations based on the equilibrium conditions of a simplified free body of prisms, and proposed equations for predicting loads on conduits due to earth fill as follows:

$W = C_d \gamma B_d^2$ for ditch conduits (A1.1)

$W = C_c \gamma B_c^2$ for positive projecting conduits (A1.2)

$W = C_n \gamma B_c^2$ for imperfect ditch conduits (A1.3)

$W = C_n \gamma B_d^2$ for negative projecting conduits (A1.4)

where C_d, C_c, and C_n = load coefficients; B_d = the horizontal width of ditch; and B_c = the out-to-out horizontal span of the conduit. Although graphical diagrams are provided for the computation of coefficients, there exist still many practical difficulties because the load coefficients proposed contain certain parameters that cannot be determined readily, such as the settlement ratio and the height of the plane of equal settlement. Graphical diagrams for C_d, C_c, and C_n are presented in Figures A1.1, A1.2, and A1.3. For load coefficients, C_c, in Figure A1.2, the rays are straight lines that can be represented by equations when the value of H/B_c exceeds the limits of the diagram. These equations are given in Table A1.1. Symbols used in Figures A1.1 through A1.6 are defined as follows:

H = height of fill above top of conduit,

B_d = horizontal width of ditch at top of conduit,

B_c = out-to-out horizontal span of conduit,

K = ratio of active lateral unit pressure to vertical and sides of ditch,

$\mu = \tan\phi$ = coefficient of internal friction of fill material,

$\mu' = \tan\phi'$ = coefficient of friction between fill material and sides of ditch,

p = projection ratio, the vertical distance from the natural ground surface to the top of the structure divided by the structure height, and

p' = projection ratio in negative projection or imperfect ditch installation, the depth of the ditch divided by its width.

As mentioned in Chapter 2, it is difficult to predetermine the actual value of the settlement ratio, r_{sd}, pertinent to a specific case. Spangler and Handy (1982) presented the recommended values of the settlement ratio based on field observations of the performance of actual culverts under embankments, as shown in Table A1.2.

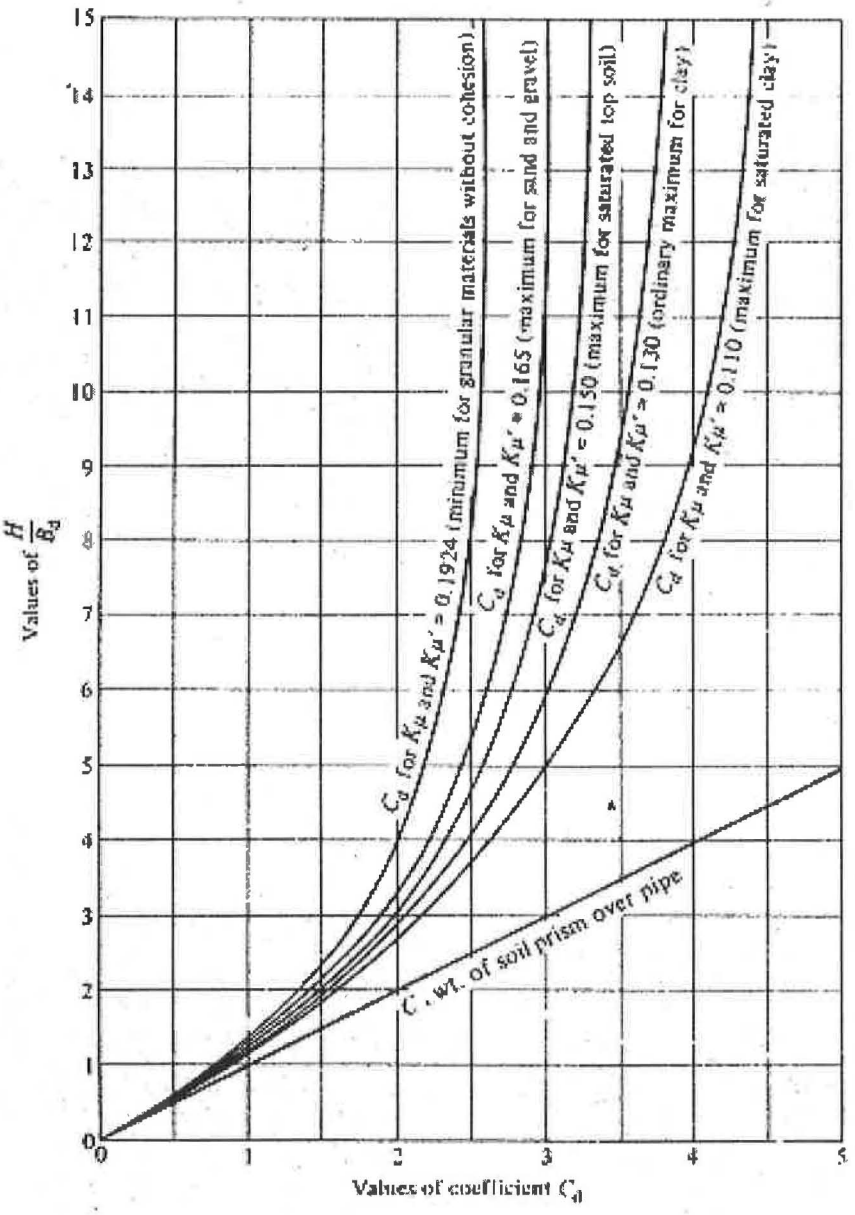

Figure A1.1: Diagrams for coefficient C_d for ditch conduits

Table A1.1: Values of C_c in terms of H/B_c

Incomplete Projection Condition		Incomplete Ditch Condition	
$K\mu = 0.19$		$K\mu = 0.13$	
$r_{sd}p$	Equation	$r_{sd}p$	Equation
+0.1	$C_c = 1.23\ H/B_c - 0.02$	–0.1	$C_c = 0.82\ H/B_c + 0.05$
+0.3	$C_c = 1.39\ H/B_c - 0.05$	–0.3	$C_c = 0.69\ H/B_c + 0.11$
+0.5	$C_c = 1.50\ H/B_c - 0.07$	–0.5	$C_c = 0.61\ H/B_c + 0.20$
+0.7	$C_c = 1.59\ H/B_c - 0.09$	–0.7	$C_c = 0.55\ H/B_c + 0.25$
+1.0	$C_c = 1.69\ H/B_c - 0.12$	–1.0	$C_c = 0.47\ H/B_c + 0.40$
+2.0	$C_c = 1.93\ H/B_c - 0.17$		

Table A1.2: Design values of settlement ratio

Conditions	Settlement Ratio
Rigid culvert on foundation of rock or unyielding soil	+1.0
Rigid culvert on foundation of ordinary soil	+0.5 ~ +0.8
Rigid culvert on foundation of material that yields with respect to adjacent natural ground	~ +0.5
Flexible culvert with poorly compacted side fills	-0.4 ~ 0.0
Flexible culvert with well-compacted side fills	-0.2 ~ +0.2

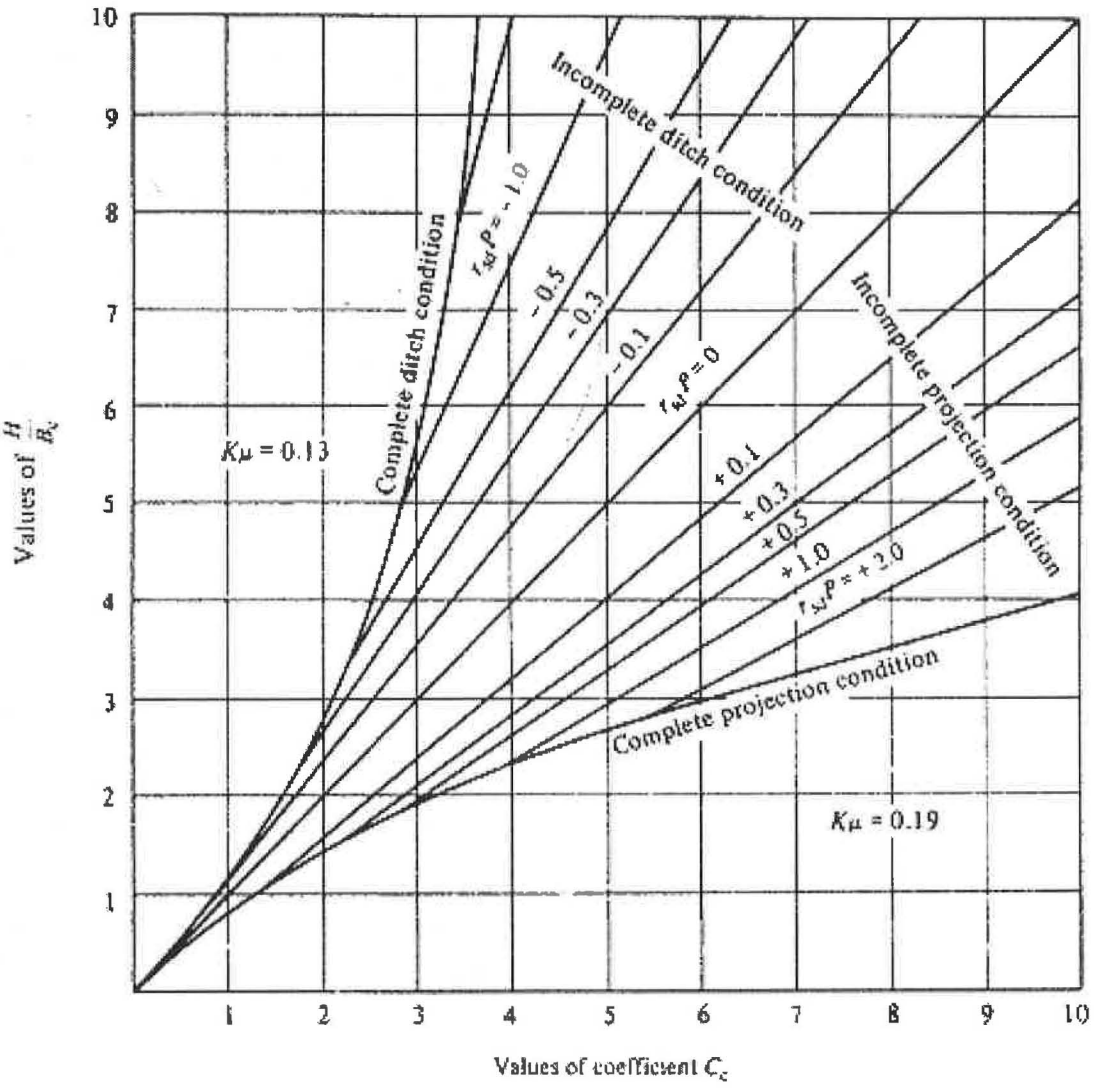

Figure A1.2: Diagrams for coefficient C_c for positive projecting conduits

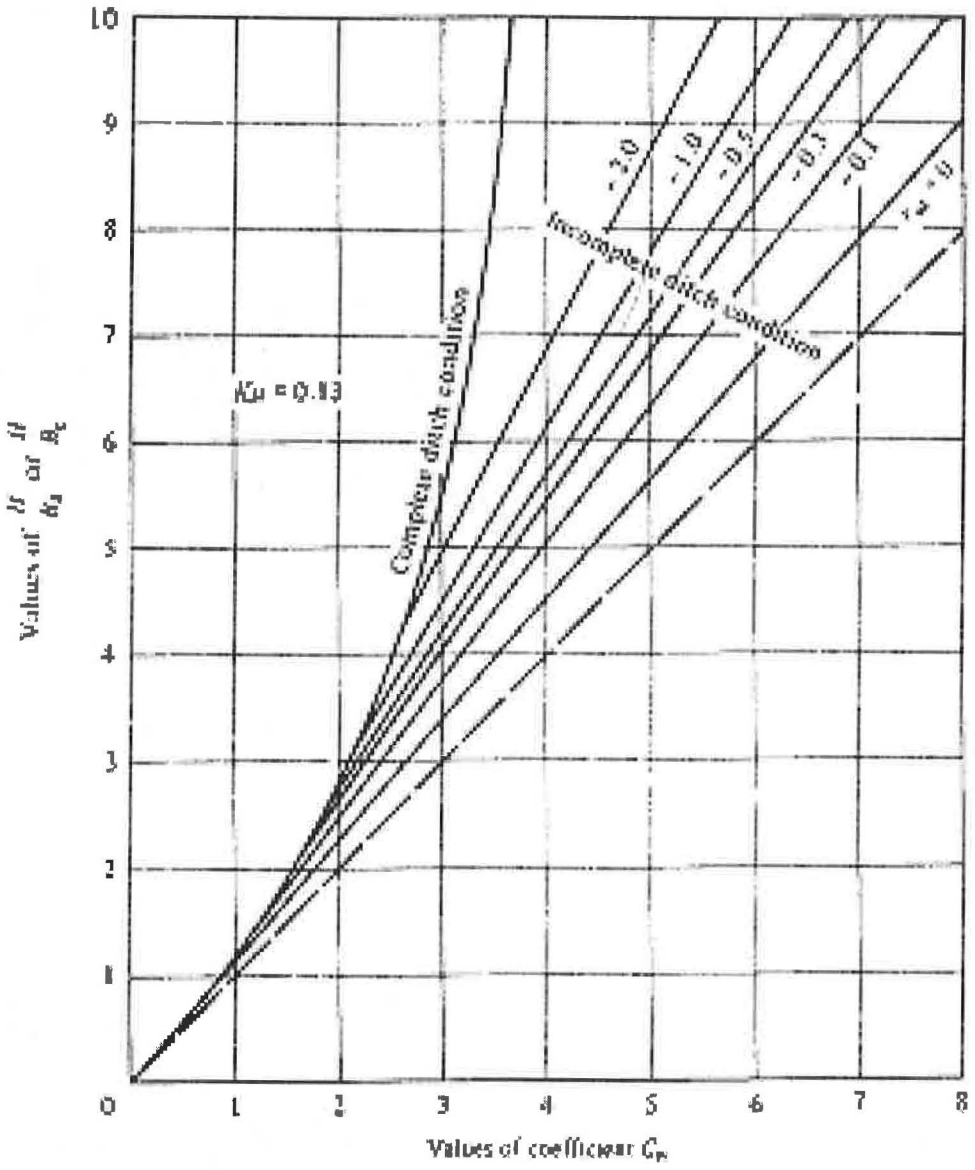

Figure A1.3: Diagrams for coefficient C_n for negative projection conduits and imperfect ditch conditions ($p' = 0.5$)

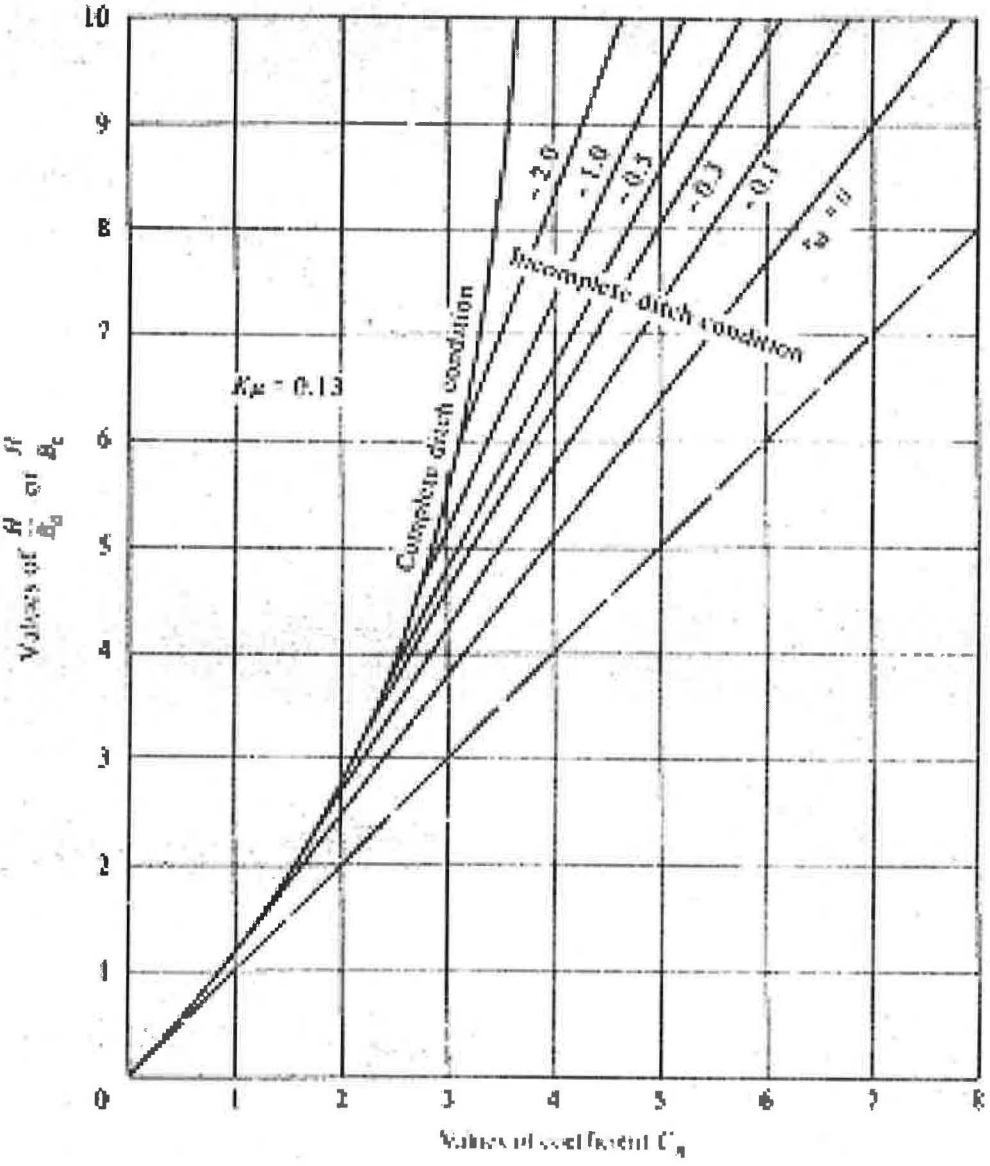

Figure A1.4: Diagrams for coefficient C_n for negative projection conduits and imperfect ditch conditions ($p' = 1.0$)

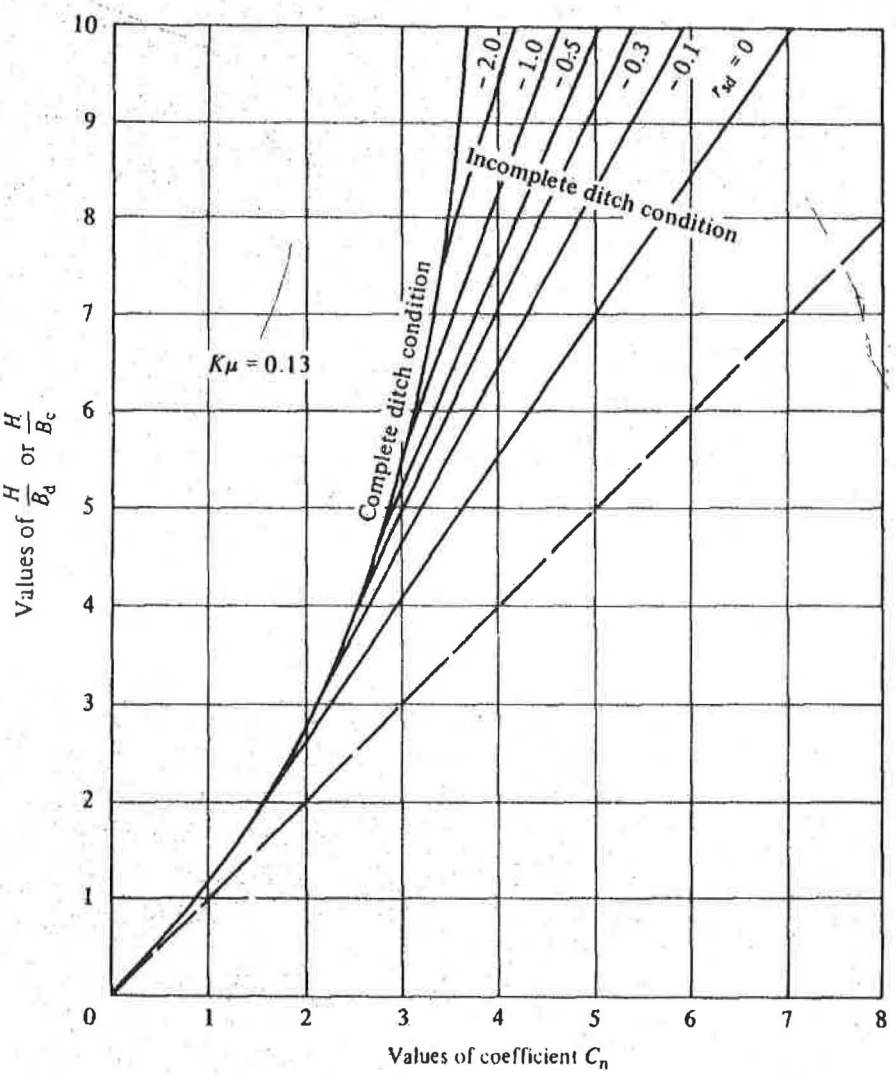

Figure A1.5: Diagrams for coefficient C_n for negative projection conduits and imperfect ditch conditions ($p' = 1.5$)

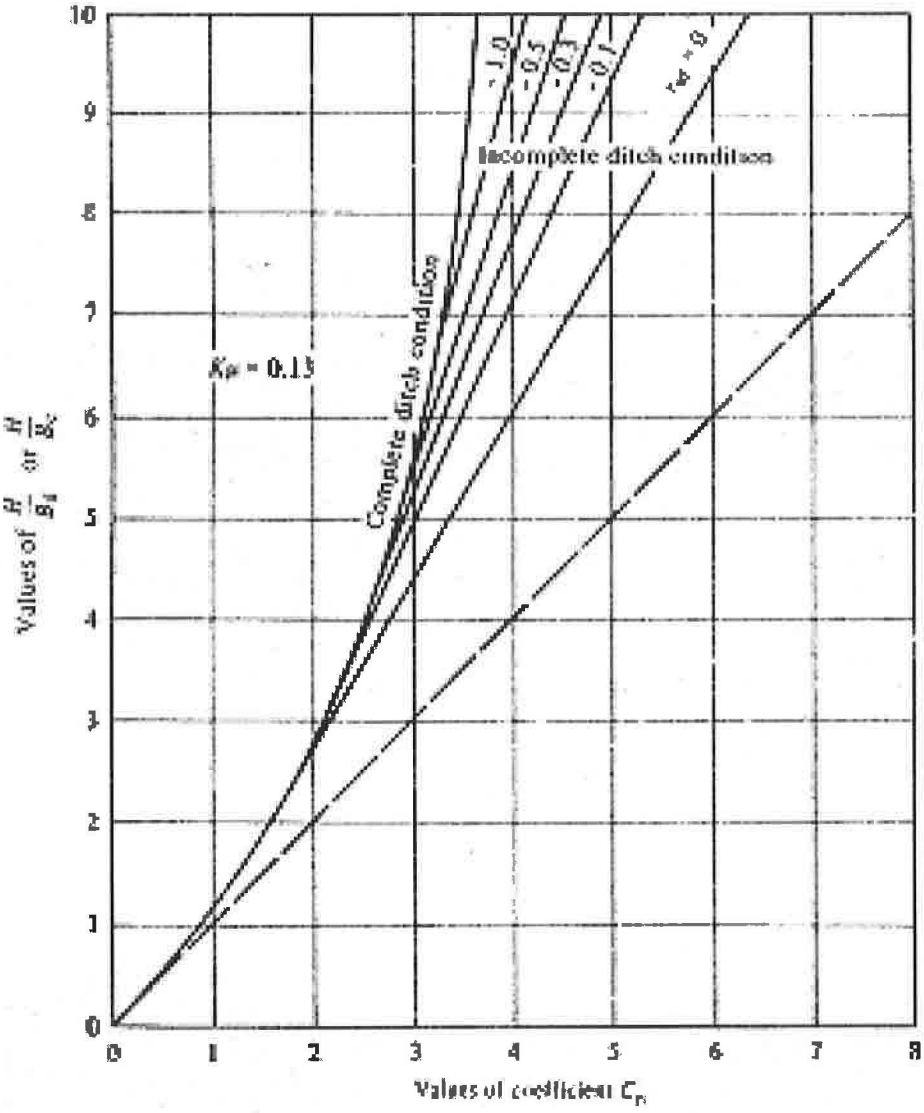

Figure A1.6: Diagrams for coefficient C_n for negative projection conduits and imperfect ditch conditions ($p' = 2.0$)

This page intentionally left blank

APPENDIX 2

SPECIAL HIGHWAY DRAWING OF HIGHWAY RESEARCH CENTER, AUBURN UNIVERSITY

This page intentionally left blank

CORRUGATED PVC PIPES

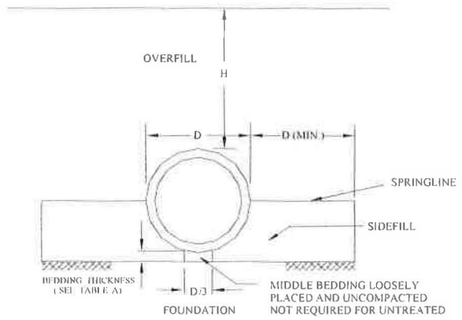

EMBANKMENT INSTALLATION

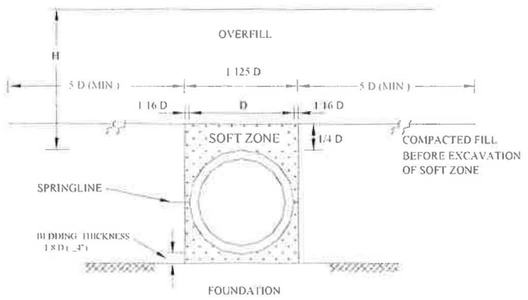

IMPERFECT TRENCH INSTALLATION

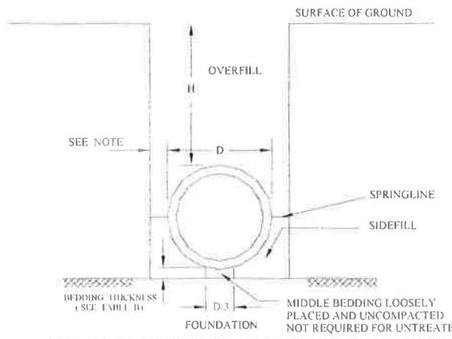

NOTE CLEARANCE BETWEEN PIPE AND TRENCH WALL SHALL BE ADEQUATE TO ENABLE COMPACTION IF CL, BUT NOT LESS THAN 1'-6"

TRENCH INSTALLATION

CORRUGATED STEEL PIPES

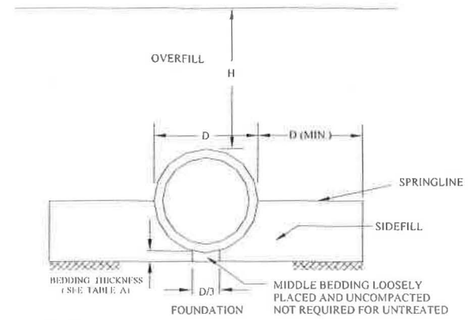

EMBANKMENT INSTALLATION

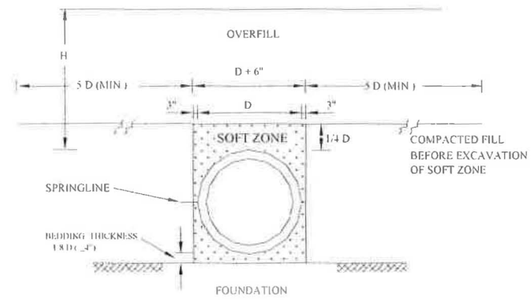

IMPERFECT TRENCH INSTALLATION

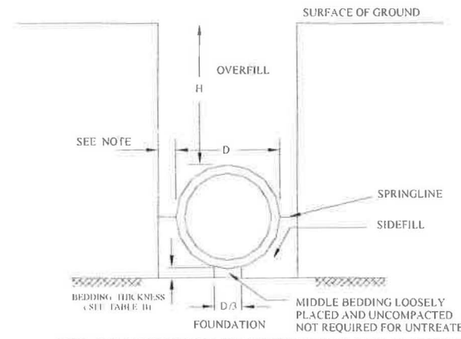

NOTE CLEARANCE BETWEEN PIPE AND TRENCH WALL SHALL BE ADEQUATE TO ENABLE COMPACTION IF CL, BUT NOT LESS THAN 1'-6"

TRENCH INSTALLATION

SOILS AND MINIMUM COMPACTION REQUIREMENTS

A. EMBANKMENT INSTALLATION

TYPE	BEDDING THICKNESS	SIDEFILL COMPACTION
TREATED	D/24" MIN., NOT LESS THAN 3" IF ROCK FOR FOUNDATION USE D/12" MIN., NOT LESS THAN 6"	90% SW
UNTREATED	NO BEDDING REQUIRED EXCEPT IF ROCK FOUNDATIONS USE Bc/12" MIN., NOT LESS THAN 6"	NO COMPACTION REQUIRED EXCEPT IF CL, USE 85%

B. TRENCH INSTALLATION

TYPE	BEDDING THICKNESS	SIDEFILL COMPACTION
NO ADVANTAGE OF TREATED SIDEFILL	D/24" MIN., NOT LESS THAN 3" IF ROCK FOR FOUNDATION USE D/12" MIN., NOT LESS THAN 6"	NO COMPACTION REQUIRED EXCEPT IF CL, USE 85%

HIGHWAY RESEARCH CENTER AT AUBURN UNIVERSITY